Characterization and Control of Electrostatically Assisted Two-Fluid Coaxial Atomization

Rodrigo Osuna Orozco

A dissertation

submitted in partial fulfillment of the

requirements for the degree of

Doctor of Philosophy

University of Washington

2021

Reading Committee:

Alberto Aliseda, Chair

James J. Riley

Nathanael Machicoane

Program Authorized to Offer Degree:

Mechanical Engineering

University of Washington

Abstract

Characterization and Control of Electrostatically Assisted Two-Fluid Coaxial Atomization

Rodrigo Osuna Orozco

Chair of the Supervisory Committee:
Prof. Alberto Aliseda
Mechanical Engineering

Multiphysics control of atomization is a promising new area of research that could result in more robust and versatile atomizers, producing a desired range of droplets under a very broad range of operating conditions. This would enable their use in applications that require the atomization process to operate within tight bounds under the influence of a changing environment and external perturbations. This dissertation studies the physics behind two-fluid coaxial atomization and transport of droplets in a turbulent gas jet, combined with the physics of electrostatic forcing. The effects of electrostatic forcing in the primary atomization, the resulting droplet population and the transport in the turbulent spray are studied over a wide range of gas-to-liquid momentum ratios, gas swirl ratios and electric field strengths. Based on the fundamental understanding of this complex multiphysics problem, a practical implementation of real-time electrostatic feedback control, based on sensing of the spray liquid distribution, is also demonstrated.

First, the role of the electric field geometry in the primary breakup of coaxial atomization is studied. Evidence is presented for strong electric stresses with an axial component opposing the flow direction that increase the growth rate and decrease the wavelength of the interfacial instabilities initiated by the shear at the gas-liquid interface. This also results in reduced liquid core lengths and smaller droplets. In contrast, a predominantly radial electric field was shown to have little effect on the metrics mentioned above.

The electrostatically assisted coaxial atomizer system at the basis of this thesis consists of a canonical coaxial nozzle enclosed between two large metallic plates held at a high electric potential. Atomization of an electrolyte solution revealed a combination of aerodynamic and electrostatic breakup mechanisms. For momentum ratios much lower than the electric Euler number, electrostatic processes were observed to dominate breakup. At high momentum ratios, aerodynamic breakup dominated the large scale features of the spray in the near field, but the electrostatic stresses gave rise to small-scale features, indicative of electrostatic breakup of small ligaments.

Interferometric measurements in the mid field revealed substantial decreases in the droplet sizes due to electrostatic forcing. Substantial radial transport that modified the mean diameter and concentration profiles of the spray was achieved for coaxial atomization at many swirl ratios. We observed preferential radial transport of small droplets, consistent with electric charge densities following a power law of the diameter given by the classical Rayleigh limit for charged drop stability.

Finally, real time feedback control is demonstrated. Proper orthogonal decomposition was used to characterize optical scattering and attenuation signals identifying the liquid distribution in the spray.

TABLE OF CONTENTS

Page

i

LIST OF FIGURES

iv

vi

ACKNOWLEDGMENTS

DEDICATION

a mi abuelo, Pino, quien me enseñó la belleza de la ciencia y la alegría de resolver problemas

Chapter 1

INTRODUCTION

Liquid atomization is ubiquitous in both the natural world and technological applications (e.g. fuel injection, thin film coating, irrigation, manufacturing). Consequently there exist a plethora of atomizer designs motivated by the great variety of applications, operating conditions and working fluids. A simple design that can create a wide range of sprays is the two-fluid coaxial atomizer, whereby, typically, a fast flowing stream of gas atomizes a much slower liquid jet. The possible range of resulting spray structures (and hence the possibility for control) is significantly expanded with the addition of swirl (angular momentum) to the coflowing gas phase.

Perhaps in a very different end of the spectrum, electrostatic atomizers have been typically confined to more specialized applications in mass spectrometry, inkjet printing and manufacturing. Electrostatic atomizers are attractive because of their high energy efficiency, the nearly monodisperse population of very small drops they can produce, and controllability of resulting charged drops. However they are typically limited to very small liquid flow rates and confined geometries, wherein the voltage between two electrodes can be easily controlled. More recently charge injection atomizers have also received much interest for their potential applications in combustion, these atomizers can operate at higher volume flow rates than typical electrostatic atomizers, but the charging they can achieve is limited by the dielectric strength of the liquid.

In spite of its widespread use, the development of real-time feedback control strategies for spray shaping remains a challenge, with many open questions and opportunities for development in this area [4]. In particular, controlling the liquid volume fraction distribution in time and space is still an elusive objective.

Both coaxial [33, 39, 14, 2, 63] and electrostatic [8, 38, 24, 19, 64, 54, 28] atomizers have been the subject of extensive study in the last few decades. More recently, there has been increasing efforts to develop hybrid atomizers that include gas flow forcing as well as an electrostatic component [49, 48, 35, 59, 29, 15, 61, 67]. These studies have revealed a wide range of atomization regimes that can be attainable with a rather simple atomizer geometry. Moreover, there has been an intense effort in developing control strategies for a variety of sprays, most notably, for fuel injection in combustion systems [43, 9, 11, 44, 5, 27, 40].

1.1 Review of Coaxial and Electrostatic Atomization

The operating principles for both coaxial and electrostatic atomizers are reviewed, along with the main hydrodynamic instabilities that dominate breakup in each case. The non-dimensional parameters that control coaxial atomization, aided with electric charge/field are defined, and known scalings are reviewed for the design of the experiment and the analysis of the results. Finally, the development of hybrid atomizers that combine these two forms of atomization is briefly described.

1.1.1 Coaxial Atomization

The basic principle of operation behind coaxial atomizers is that the shear between the gas and liquid phases lead to instabilities that break up the liquid jet into droplets (a simple schematic is shown in figure 1.1). This apparently simple setup can yield a wide range of behaviors (1.2). Although a complete characterization of turbulent coaxial atomization has not been achieved yet, research from the last few decades has yielded many insights into the process. The different atomization regimes achievable by coaxial atomizers have been studied extensively, and the physics of the different regimes, as well as where in non-dimensional parameter space they take place are described in two-decade-old reviews [7, 32]. This multiphase flow can be characterized in term of the following non-dimensional parameters (we list six for completeness, but 5 are sufficient to fully characterize the flow):

$$Re_l = \frac{U_l d_l}{\nu_l}$$

$$Oh = \frac{\mu_l}{\sqrt{\rho_l \sigma d_l}}$$

$$m = \frac{\rho_l U_l A_l}{\rho_g U_g A_g}$$

$$M = \frac{\rho_g U_g^2}{\rho_l U_l^2}$$

$$We = \frac{\rho_g U_g^2 d_l}{\gamma}$$

$$Re_g = \frac{U_g(d_g - D_l)}{\nu_g}$$

These are: The liquid Reynolds and Ohnesorge numbers, the gas-to-liquid mass loading and momentum ratios and Weber number. U_i denotes the mean velocity at the outlet (volume flow rate divided by cross sectional area), ν_i the kinematic viscosity, μ_i the dynamic viscosity, ρ_i the mass density, γ the interfacial surface tension, D_i the outer diameter of the tube where either phase is flowing, d_i the inner diameter, A_i the cross sectional area, and the subscripts l and g denote the gas and liquid phases respectively. The gas Reynolds number is redundant with a combination of other non-dimensional parameters and, in this study, is somewhat analogous to the gas-to-liquid momentum ratio, as the liquid Reynolds number (and velocity) is held constant, and the gas is always turbulent above the critical Reynolds number for mixing transition.

The region near the exit of the nozzle where the primary atomization occurs and the liquid jet emanating from the nozzle is broken down into droplets and ligaments can be referred to as the near field. This is also where instabilities from the interaction of the two phases develop and grow. It has been observed that processes occurring in this region play a large role in the spray formation and its characteristics downstream [23]. Both longitudinal and transverse instabilities arise due to the shear at the interface since there is a difference in velocity between the two phases [39]. The growth and development of instabilities in the
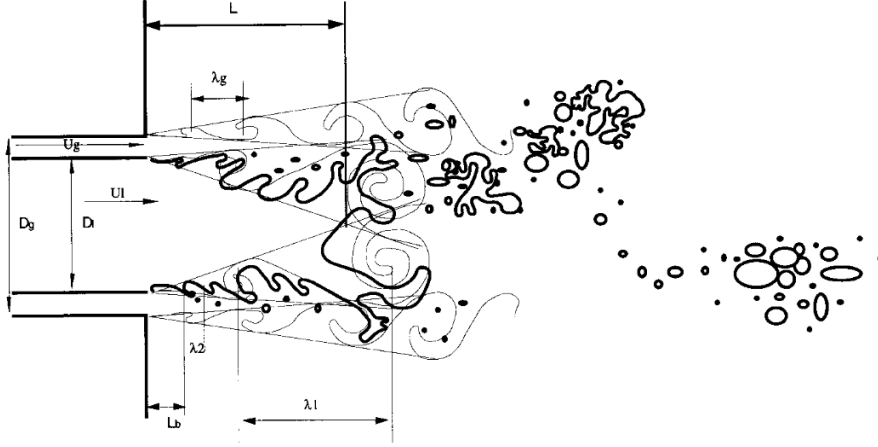
Figure 1.1: Schematic of coaxial atomization (taken from [32]).

near field plays a crucial role in primary atomization and thus in the formation of droplets and their size distributions [2, 33, 63].

The morphology of the liquid jet, and in particular of its surface instabilities, has also been subject of intense study as it may be crucial for some applications. Most atomization processes exhibit complex dynamics and deformations of the liquid jet before breakup (with notable exceptions such as the electric Taylor cone), and it is difficult to provide a complete three dimensional description of the complex interface. Consequently, the research community has focused on the most meaningful metrics that describe the features of the spray in the near region.

Notably, the liquid core length has been described extensively and many scalings, arguments and correlations have been offered to describe its evolution with several non-dimensional parameters [32]. It is important to emphasize that that these descriptions focus solely on the average intact length and discussion of its statistics and temporal dynamics have only been explored recently [30, 37]. Another important metric in the near field is the spray spreading angle. As is the case with the core length, several descriptions for the different regimes have been offered, again focusing almost exclusively on mean values. Closely
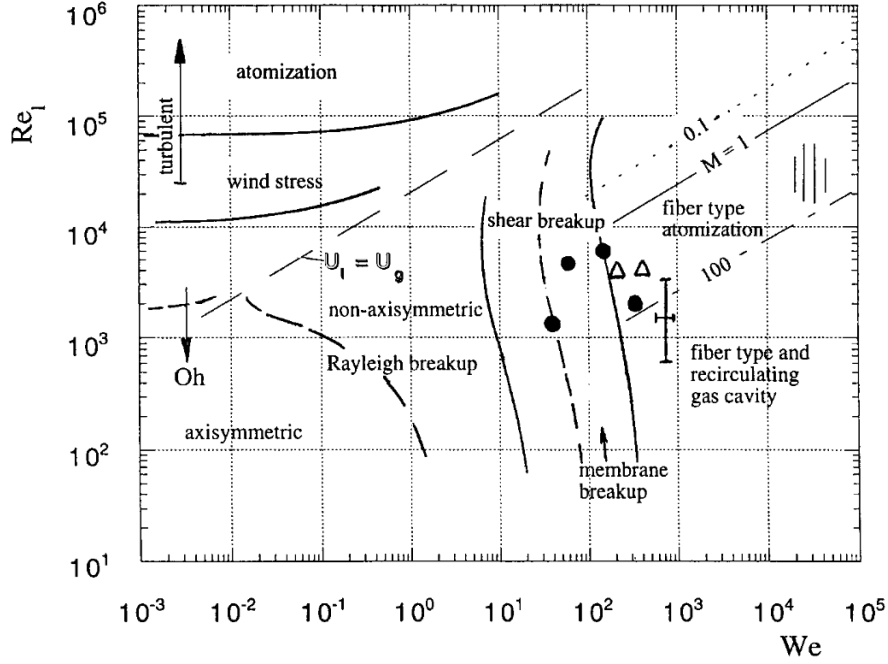
Figure 1.2: Diagram of coaxial atomization regimes in the parameter space of the liquid Reynolds number and the Weber number (taken from [32]).

related to this spray metric is the virtual origin, which is the location where the vertex of the lines defining the spreading angle would meet. These definitions are analogous to those for a single-phase turbulent round jet.

The dynamics of coaxial atomization are notoriously complex and involve multiple spatial and temporal scales. Two of the most prominent dynamic features has been described in terms of two characteristic frequencies: a shedding frequency and a flapping frequency. The shedding frequency can be deduced from the temporal dynamics of the liquid core length [37]. A detailed description of the flapping instability of the liquid core has been given by Delon and Cartellier [12] and has been show to exhibit different regimes depending on the ratio of the wavelength of the shear instability to the liquid jet diameter.

1.1.2 Electrostatic Atomization

Interestingly, the scientific study of electrostatic atomization predates coaxial atomization, with one of the earliest records in the literature by the abbot Jean Antoine Nollet in 1754 [45]. In spite of its long history, the electrospray technique did not receive much attention until much later, especially for its application in mass spectrometry. One of the most attractive features of the electrospray technique is its capacity for generating nano and micro-scale droplets with a nearly monodisperse size distribution. Such a spray is formed under conditions that allow to maintain a steady Taylor cone, i.e. a conical meniscus resulting from the equilibrium of capillary and electrostatic stresses. This mode of atomization is, thus, limited to very low (capillary) flow rates [24, 19].

Recently Li and coworkers performed a linear instability analysis of a viscous coflowing liquid-gas jet and identified key electric parameters of such flows [35].These are the electrical Euler number ($Eu = \epsilon_0 E_0^2 / \rho_l U_l^2$) and the ratio of hydrodynamic time scales to the electrical relaxation time $T = \sigma_l d_l / \epsilon_0 U_l$, where $U_l, \rho_l, d_l, \epsilon_0, E_0$,and σ_l are the average liquid exit velocity, density, nozzle diameter, permittivity of free space, electric field strength, and electrical conductivity. The average velocities are calculated from the volume flow rate and the cross-sectional area of the nozzle exit and the diameters are the liquid nozzle inner diameter and the gas nozzle effective diameter. It is worth noting that typically the control parameter is not the electric field itself but an applied voltage from which the electric field can be computed (typically from the Laplace's equation assuming a charge free region that ignores the charges in the drops). In principle it is very hard to evaluate accurately the electric field given the complex geometry of the breaking liquid core. Approximations typically consider solutions for the electric field in the surface of a cylinder with either a prescribed surface charge density or a voltage drop at a concentric cylinder a known distance away [35, 55, 56, 57, 58, 68].

In addition to the non-dimensional numbers described above there are two numbers of relevance for the droplets in the spray, these are the droplet Weber number ($We_d = \rho_g u_r^2 d/\gamma$),
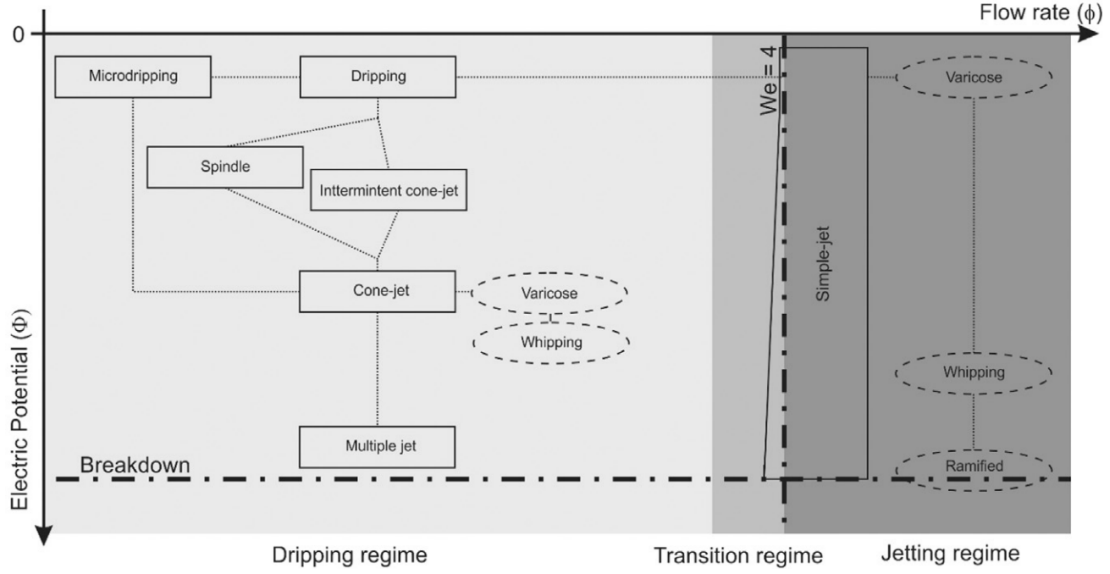
Figure 1.3: Diagram of electrohydrodynamic (EHD) atomization regimes in the parameter space of flow rate and electric potential (taken from [1]).

and the ratio of the electrostatic repulsion of charges in a drop to the surface tension holding a drop together, $(q/\pi(8\epsilon_0\gamma d^3)^{1/2})$, where u_r, d and, q are the droplet's slip velocity (velocity relative to surrounding gas), diameter and electric charge respectively. The second of the non-dimensional groups determines the Rayleigh limit for the size of a charged droplet so that a droplet for which this number exceeds unity is unstable and will break into two or more droplets for which the electrostatic repulsion does not exceed the surface tension forces[51].

The regimes of electrohydrodynamic (EHD) breakup have been described in a recent work by Agostinho and coworkers [1]. As can be seen in the diagram in figure 1.3 the EHD breakup of liquid jets can exhibit a rich morphological variety over the parameter space of electric potential and flow rate. Of these regimes the one most extensively studied by far is the cone-jet mode electrospray [8, 1, 19], due to the virtually monodisperse population of very small droplets it can generate. However, the constrained flow rate at which this can be achieved limits this atomization mode to specialized applications such as mass spectrometry.

In addition to the primary breakup of the liquid jet, electrohydrodynamic forces can significantly contribute to the secondary breakup. One of the earliest studies of breakup of charge drops was the seminal work of Lord Rayleigh almost a century and a half ago [51] where he explored the role of the destabilizing electric forces due to surfaces charges and the stabilizing role of surface tension. Experimental work has demonstrated that drops typically can reach values of around 80% of the Rayleigh limit [22] before undergoing what has been termed Coulomb fission. Such breakup typically involves the deformation of the drop with one or two conical protrusions and tip-streaming of small highly charged drops from the tips of said protrusions [10]. Moreover, not only do the surface charges destabilize the drop, but conducting drops can also be destabilized due to the presence of an electric field that polarized the charges in said drop [62]. More recently the interplay between these two effects as well as with the aerodynamic stresses that arise as the drop accelerates due to the electric force has been investigated [41]. Interestingly, the electric forces tend to deform the drop into prolate shapes whereas the aerodynamic drag tends to deform the drop into oblate shapes, so that there may be competition between the two.

1.1.3 Hybrid Atomizers

During the last few decades, some designs have been proposed seeking to leverage both coaxial and electrostatic atomization. An especially well-studied design is the one used for so-called electro flow-focusing [35, 19, 29]. For these designs, the electrostatic force has been kept as the dominant contribution to atomization, and consequently researcher have limited the experimental space explored to very low values of the gas-to-liquid momentum ratio, typically of order unity. Because of these limitations, and in spite of these recent studies, there seems to remain ample opportunity for the study of electrostatically-assisted coaxial atomizers, especially regarding the exploration of higher momentum ratio, as well as the role of swirl injected in the gas flow at the nozzle.

Most of the work exploring the combination of electrostatic atomization and a coflowing gas has been done from the perspective of the electro flow-focusing (EFF) technique intro-

duced by Gañán-Calvo et al.[20, 18]. This technique has seen very fruitful applications for mass spectrometry [16, 17] and in the context of microfluidics involving two liquid phases [6, 25, 65]. Allaf-Akbari and Ashgriz [3] explored atomization regimes of electrospray in gaseous cross-flow, involving either stable or unstable Taylor cone jets where the main atomization mechanism is electrostatic. Notably, research has focused mostly on situations where the mass flow rate and Reynolds number of the liquid jet are very small (amenable to the aforementioned applications).

1.2 Multiphysics Control of Atomization

The development of control strategies for sprays has been of great interest for the fuel combustion community, as is evident in numerous examples of active control for fuel combustors that have been documented in the last couple of decades [43, 9, 11, 44, 5, 27, 40]. However, as indicated in a recent review [4], ample opportunities remain for the development of new active control strategies for sprays (spray control is referred to here as closed-loop feedback actuation on the atomization and droplet dispersion stages to achieve a particular spray structure, droplet size and/or spatiotemporal distributions).

Multiphysics control of atomization is a promising new area of research that could result in more robust and versatile atomizers that can produce the desired range of droplets under very diverse operating conditions, enabling their use in applications that require the atomization process to operate within tight bounds under the influence of a changing environment and external perturbations (e.g., as it may occur in the combustion chamber of a jet engine onboard an aircraft or in a coating process with heat and mass transfer and phase change). Although a very wide range of atomizers has been designed for various applications, the spray characteristics produced are typically determined by the design itself and offer limited controllability in the presence of perturbations. These could be environment changes, variability of the liquid properties, of the injected flow rate, etc. leading to fluctuations in the produced droplet size and number density that could drift outside acceptable spray properties. The development of robust and versatile closed-loop control strategies for atomization remains

a fundamental challenge, and including multiphysics actuation (e.g. electrostatics, acoustics, swirl, etc.) may offer a possible solution for this fundamental problem or for specific applications [4, 44, 46, 47].

Chapter 2

EFFECT OF ELECTRIC FIELD DIRECTION ON PRIMARY BREAKUP

We present an experimental investigation of the electrostatically-assisted primary atomization in a coaxial gas-liquid jet. Shadowgraphy imaging reveals the primary breakup dynamics and allows for a semi-quantitative assessment of the resulting droplet characteristics. We describe the statistics of the liquid core in terms of the probability distributions of its length, the spray angle and the virtual origin. A strong axial electric field reduces the liquid core length over a wide range of gas-to-liquid momentum ratios, whereas a predominantly radial electric field influences the atomization process weakly. We characterize the primary breakup dynamics in terms of two frequencies associated with the liquid mass: the flapping frequency and the droplet-shedding frequency. Using a combination of proper orthogonal decomposition (POD) and Fourier Transforms in time and space, we derive empirical dispersion relations. Observations of the initial interfacial instabilities' growth reveal shorter wavelengths and higher growth rates in the presence of a strong axial electric field. This enhanced growth of the interfacial instabilities is consistent with a mechanism whereby Maxwell stresses drive liquid ligaments out radially across the high-speed annular gas jet, thus improving the momentum transfer between the two phases, and enhancing the break-up process (producing smaller final droplet sizes). These results illustrate the importance of the electric field configuration to assist two-fluid coaxial atomization and establishes electrostatic forcing as a potential feedback control input.[1].

In this chapter, we present experimental observations of the primary breakup of an electrically-charged laminar liquid jet by a turbulent coaxial gas flow and an external electric

---

[1]This Chapter was adapted from a manuscript submitted to the journal Physical Review Fluids, under the title *Effect of Electrostatic Forcing on Coaxial Two-Fluid Atomization*

field. Section 2.1 describes the experimental setup and experimental methods, section 2.2 summarizes the results and section 2.3 presents the discussion of the results and conclusions.

2.1   Methods

2.1.1   Atomizer

We studied the atomization of an electrically charged laminar liquid jet exposed to a turbulent coaxial gas stream for gas-to-liquid momentum ratios ranging from 1 to 25. We define the momentum ratio, M, as the ratio of the dynamic pressure of the gas to that of the liquid, $M = \rho_g U_g^2 / \rho_l U_l^2$, where ρ is the density and U the mean velocity computed as the volume flow rate divided by the cross-sectional area of the nozzle, and the subscripts indicate the gas and liquid phases. The working liquid was reverse-osmosis purified water with a conductivity of $3\mu S/cm$ and the gas was standard air. The canonical coaxial atomizer (see figure 2.1) used for this study is available in open-source[2]. The design, fabrication and operational aspects have been described in detail in previous work [36]. Figure 2.1 shows a schematic for the atomization setup.

2.1.2   Electric Field Geometry

A negative electric field was applied by connecting the liquid nozzle and two external plates to a high voltage generator. Thus, the liquid droplets issuing from the atomizer were negatively charged. A strong electric field approaching the dielectric strength of air is applied by connecting the metal liquid nozzle to a high voltage power supply and grounding a copper ring at the perimeter of the gas nozzle. To shape the geometry of the electric field in the atomization region, a pair of metallic plates running along the length of the spray axis were either grounded or set to a potential of -5 kV (equal to that of the liquid nozzle). With the plates at -5 kV, the electric field is strongly radial from the liquid towards the copper ring,

---

[2]The atomizer design is made available to the community at http://depts.washington.edu/fluidlab/nozzle.shtml
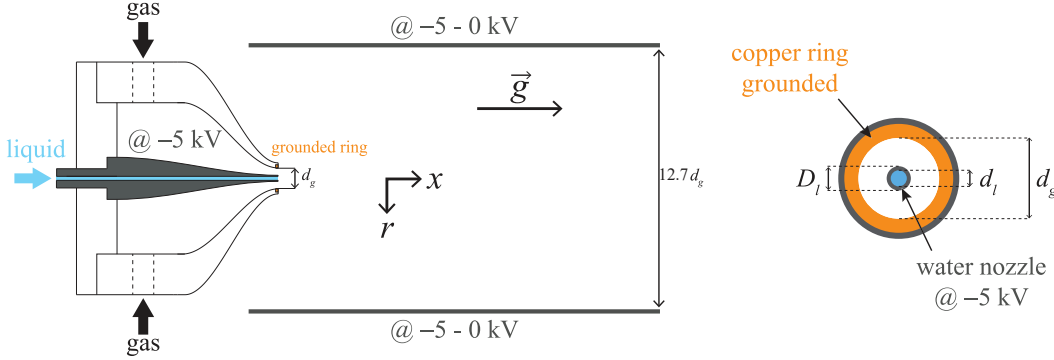
Figure 2.1: Side cut and front view of atomizer showing relevant dimensions; d_l is the liquid nozzle inner diameter, D_l is the liquid nozzle outer diameter and d_g is the gas nozzle inner diameter. The metallic plates are 8"x8" and 5 inches apart.

whereas when the plates are grounded, the electric field has a larger axial component. Figure 2.2 illustrates the geometry of the electric field in the configurations explored, as obtained from finite element simulations. For these simulations we assumed a straight liquid jet of a length that's relevant to the range of M studied. The non-dimensional group describing the ratio of electrostatic to inertial forces, the electrical Euler number [35], was estimated as $Eu = \epsilon_g E_0^2 / \rho_l U_l^2 \approx 10^{-2}$, where ϵ_g is the permittivity of air and the electric field strength E_0 is given by the voltage drop and the distance between the nozzle and the grounded ring.

2.1.3 High-Speed Imaging

High-speed shadowgraphy imaging with a temporal resolution of 100 μs (10,000 frames per second) was used to identify the liquid core and the resulting droplets. The spatial resolution of the imaging was 91.3 or 27.3 microns per pixel, where the lower resolution was utilized for the lower momentum ratio conditions. Image postprocessing identified the presence of liquid along the line of sight of the camera following methods described previously [37]. Figure 2.3 illustrates the liquid core as delineated digitally from the images, with the intact length L_b defined as the farthest distance downstream from the nozzle where there is liquid
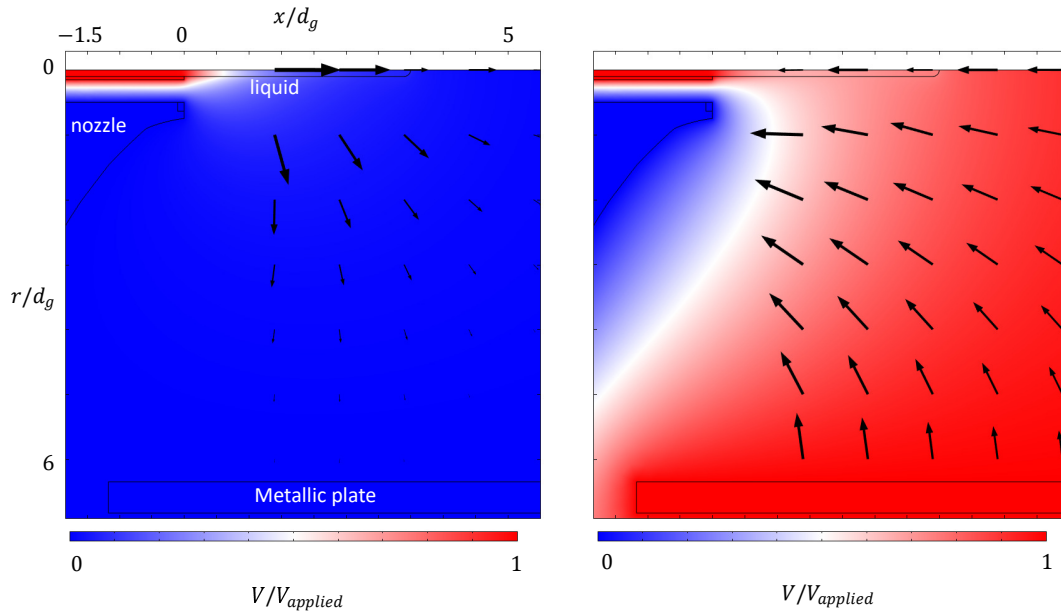
Figure 2.2: Finite Element Method (FEM) simulation illustrating the voltage and electric field lines for the two cases considered: grounded plates (left) and charged plates (right).

continuously connected to the issuing liquid jet. Similarly, the resulting droplet population was characterized based on identification of approximately circular objects in the image. Only detected objects whose perimeter was less than 2π times their equivalent diameter (where the equivalent diameter is computed from the objects' projected area on the image) are used in the analysis as valid droplets.

The spray angle and virtual origin (the point where linear projections of the points defining the width of the jet converge, see figure 2.3) were obtained following the method proposed by the authors in previous work [37]. The liquid core length was obtained from the mean image intensity map using a threshold to identify the region always occupied by liquid.

We measured two key aspects (and their corresponding frequencies) of the liquid motion that are critical to understanding the break-up dynamics: the flapping frequency and the shedding frequency. The flapping frequency can be detected by the transversal variations of
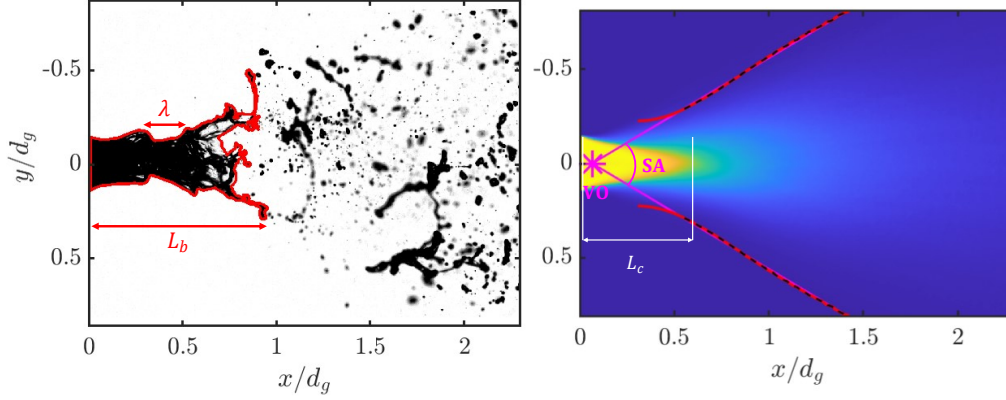
Figure 2.3: Metrics used to characterize the spray morphology. Wavelength, λ, of interfacial instabilities and instantaneous liquid intact length shown for a single snapshot(left). Metrics derived from the mean intensity field (right) included the virtual origin (VO), spreading angle (SA), and the liquid cone length.

the light intensity in the liquid core region, whereas the shedding frequency can be identified from the time series of the intact length [37]. From the time series of the intact length the shedding frequency was computed using Welch's method of averaging over overlapped segments to estimate the power spectral density (PSD). For the flapping frequencies we obtain a time series for every axial location by summing the binarized image intensity over all locations above and below the centerline and substracting these two sums (thus it is the difference of the number of locations with liquid present above and below the centerline). Then we estimate the PSD for every location (figure 2.4, left) and average the PSD for locations less than 1.5 liquid intact lengths from the nozzle (figure 2.4, right).

The entrainment speed, u_e, and wavelength, λ, of the initial interfacial instabilities were computed by tracking of local maxima of the gas-liquid interface radial position. The growth rate of the instabilities, $\dot{\xi}/\xi$ (where ξ is the radial position of the interface relative to the unperturbed state), was approximated based on the relation $u_e \approx \lambda \dot{\xi}/\xi$ proposed by Villermaux [66]. The velocities were estimated using tracks of local maxima (similar as done in previous
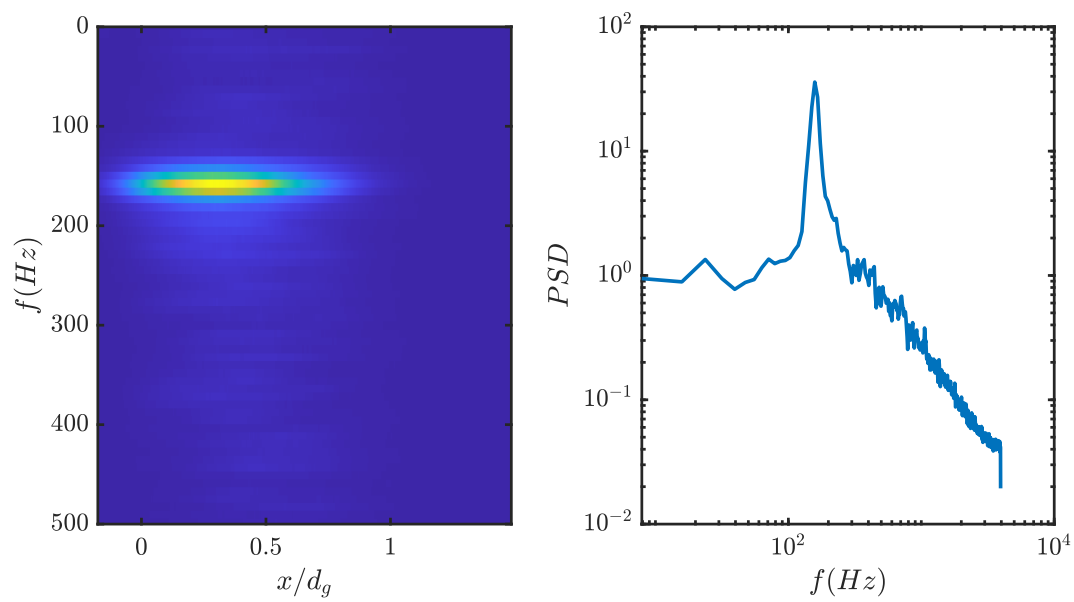
Figure 2.4: Power spectral density of the flapping signal computed for each axial location, notice the bright band near characterizing the flapping motion of the liquid jet (left). Average of the PSD over axial locations less than 1.5 liquid intact lengths from the nozzle, the clearly dominant frequency is the estimate of the flapping frequency (right).

work [53]) that were at least four frames long and that could be fitted with a quadratic expression (assuming nearly constant acceleration) with $R^2 > 0.99$.

Proper orthogonal decomposition (POD) from the images was performed by an implementation of the singular value decomposition analysis. For the purpose of identifying the dynamics of the liquid core, POD was applied to the images after applying a mask that removed drops and ligaments. To derive the empirical dispersion relation, a 2D Fourier transform on all POD modes, and a 1D Fourier transform on their corresponding time vectors, was performed. For robustness, a PSD-weighted mean of the temporal frequency and spatial wavelength was computed. Thus, we obtained unique frequency-wavelength pairs for each POD mode (figure 2.5).
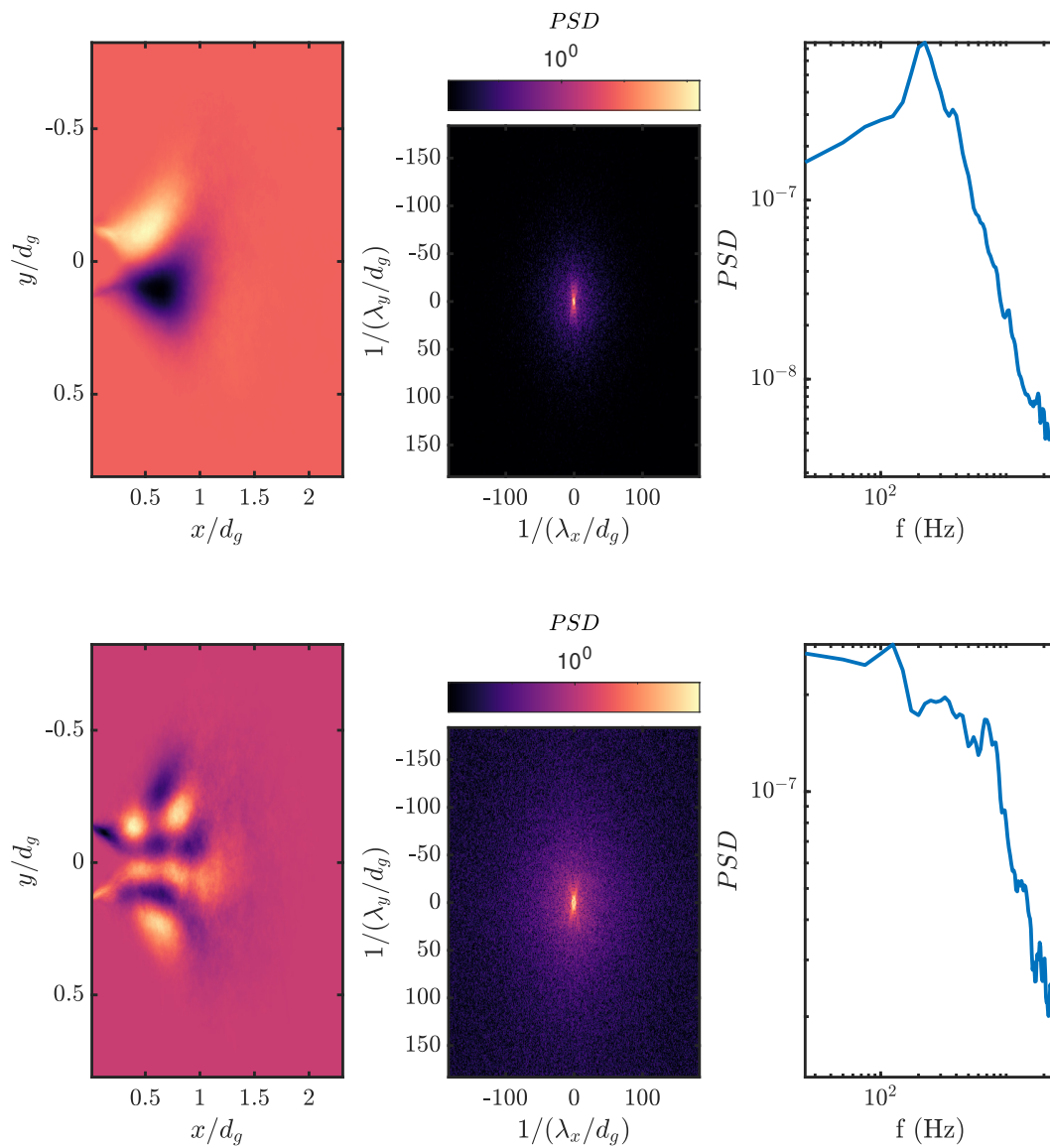
Figure 2.5: POD modes (left), shown along with their 2D FFT (middle) and FFT of the corresponding time vector (right) for modes #1 (top) and #22 (bottom). Higher order modes contain shorter wavelengths in space and higher frequencies in time.

2.2 Results

2.2.1 Liquid Core Lengths

Figure 2.6 shows snapshots of atomization at three momentum ratios with (right) and without (left) electric field. The influence of the electric field is readily apparent in the increased curvature and decreased intact length of the liquid core.

The radial electric field results in significantly shorter intact lengths at all momentum ratios explored, as opposed to the axial electric field that leaves the intact length approximately unchanged (figure 2.7). The mean liquid core length reveals the same trend as the intact length indicating a clear reduction due to the axial electric field across all momentum ratios explored 2.7. For the case of the radial electric field, there is a smaller reduction in the liquid core length for the two smallest momentum ratios. The observed liquid cone lengths (especially at low M) are in good agreement with the expression derived by Lasheras and Hopfinger [32]:

$$\frac{L_c}{d_l} \approx \frac{6}{\sqrt{M}} \frac{1}{(1 - B_1\sigma/\mu_g U_g)^{1/2}} \tag{2.1}$$

where B_1 is a coefficient weakly dependent on the gas Reynolds number, μ_g is the gas dynamic viscosity and σ is the interfacial surface tension.

Interestingly, Figure 2.8 shows that the standard deviation of the liquid length remains relatively unaffected by the electric field, whereas the skewness is strongly affected by the axial electric field. All the values of the kurtosis are close to 3 (the kurtosis of a normal distribution) indicating that the distributions do not have very broad tails (Figure 2.8).

In addition to the intact length, we characterized the mean liquid cone geometry, in terms of the spreading angle and virtual origin (Fig. 2.9). For low momentum ratios, enhanced atomization, due to the axial electric field, leads to a much larger spreading angle. In contrast, for larger momentum ratios, the spreading angle is noticeably smaller whenever the electrostatic forces tend to repel the droplets away from the plates (i.e. for the case when the plates are held at the same potential as the liquid nozzle).
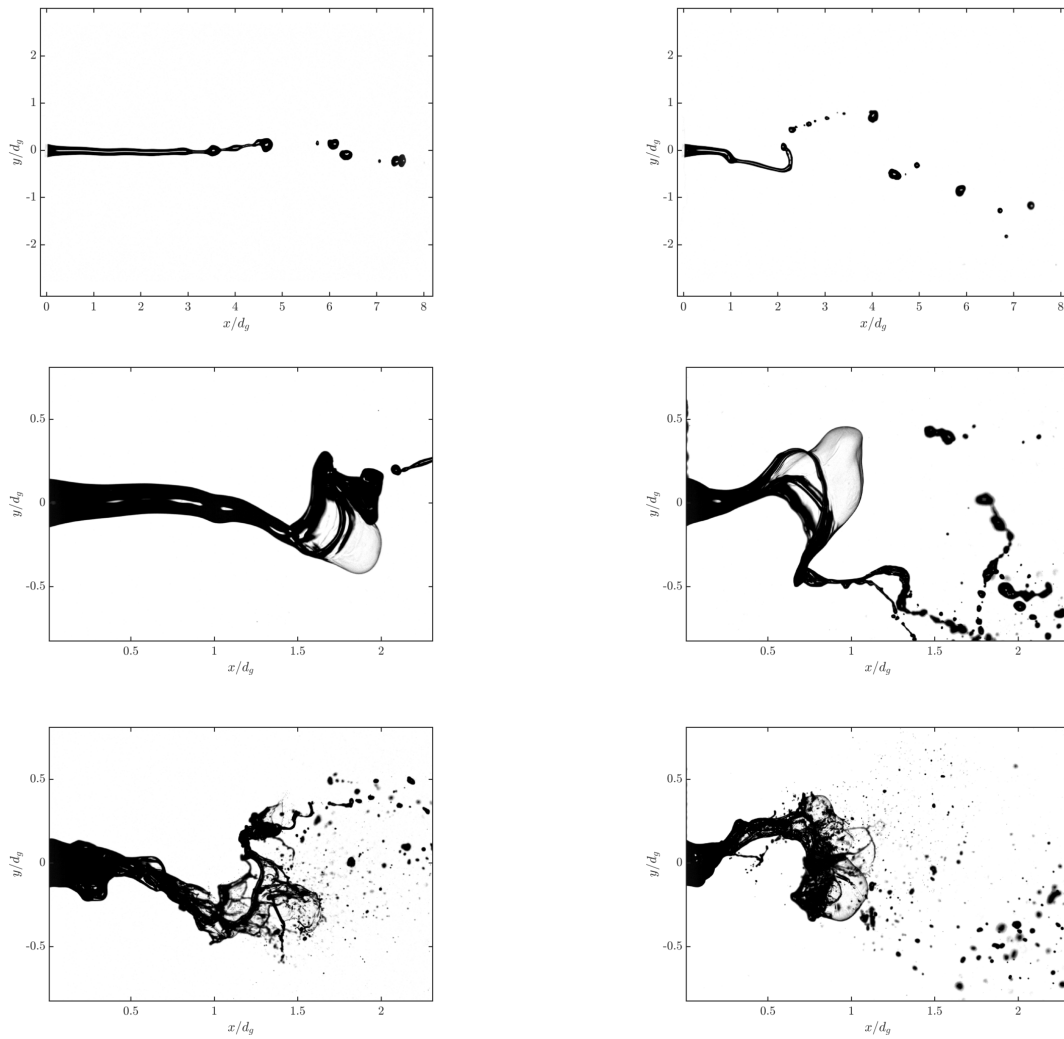
Figure 2.6: Snapshots of the liquid core at momentum ratios of 1, 2 and 5, with no electric field (left) and with the radially-oriented electric field (right). Notice the higher curvature and shorter intact length for the case with the electric field.
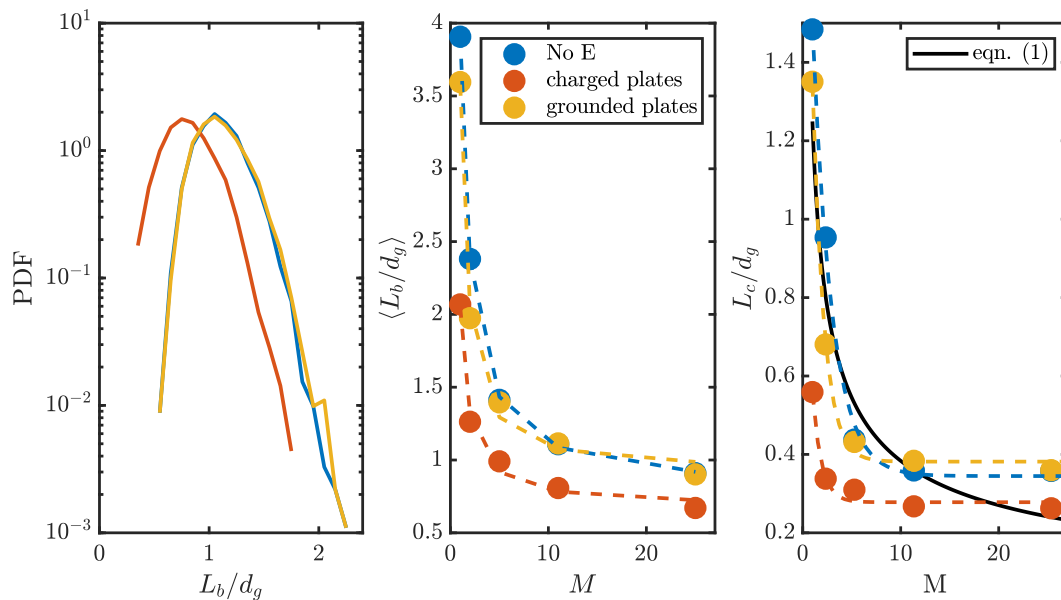
Figure 2.7: (left) Probability density function (PDF) of intact length for M=11. Only the radial electric field has a substantial effect in reducing the intact length. (middle) Mean intact length as a function of momentum ratio. (dashed lines are power laws fits, displaced by a constant). (right) Liquid core length as a function of M. The black line is the expression proposed by Rehab [52]. The fits are all exponentials plus a constant with $R^2 > 0.95$

.
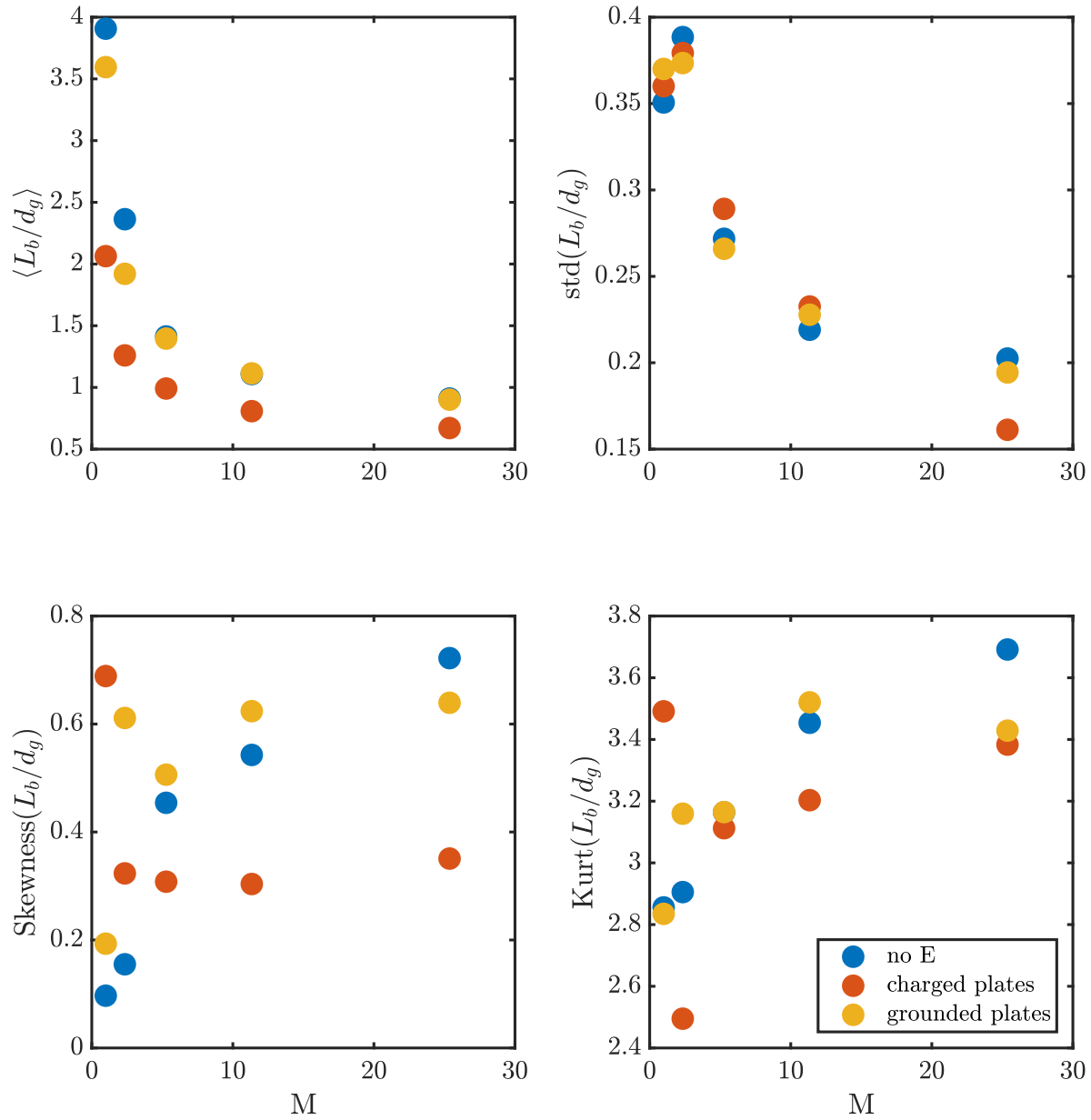
Figure 2.8: First four statistical moments of the liquid intact length.
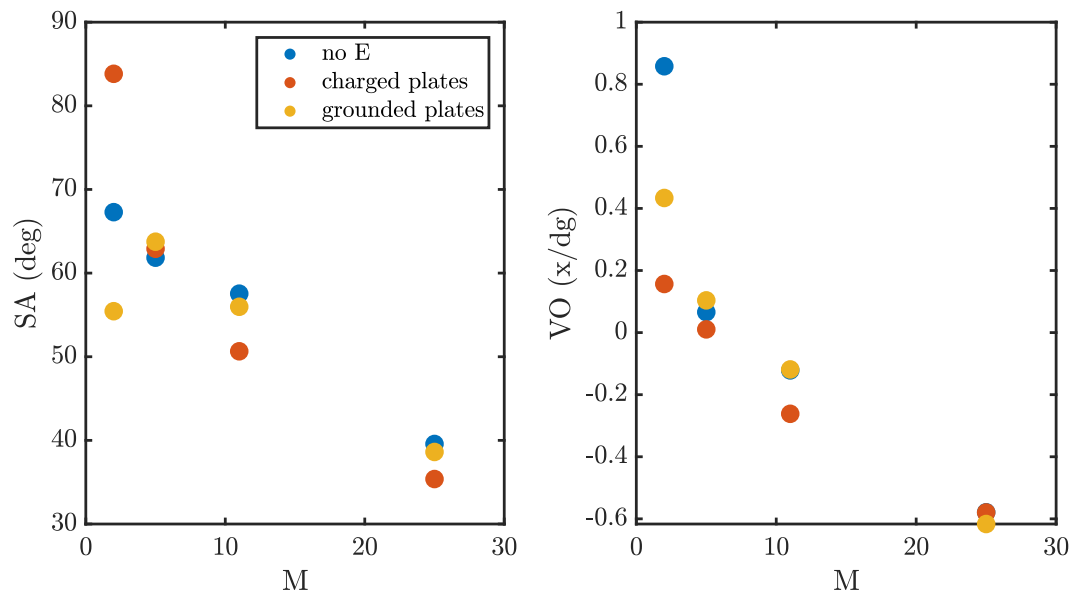
Figure 2.9: Spreading angle and virtual origin.

2.2.2 Liquid Core Frequencies

As shown in Fig. 2.10, no significant impact of the electrostatic field or the droplets electric charge on the flapping frequency was observed. In contrast to the flapping frequency, the shedding frequency does get modified by the electrostatic forcing. As with other spray characteristics, the impact of the radial electric field is strongest (figure 2.10).

The ratio of these two frequencies increases from about 1 at low momentum ratios to 2 at higher momentum ratios, revealing a differential effect of the hydrodynamic instabilities of the liquid-gas interface on the shedding dynamics and consequently on the intermittency of the droplet generation. Furthermore, the characteristic frequencies computed from the time series of the number of drops crossing the edge of the image, shown in figure 2.10 c, matched well with the liquid core shedding frequency.
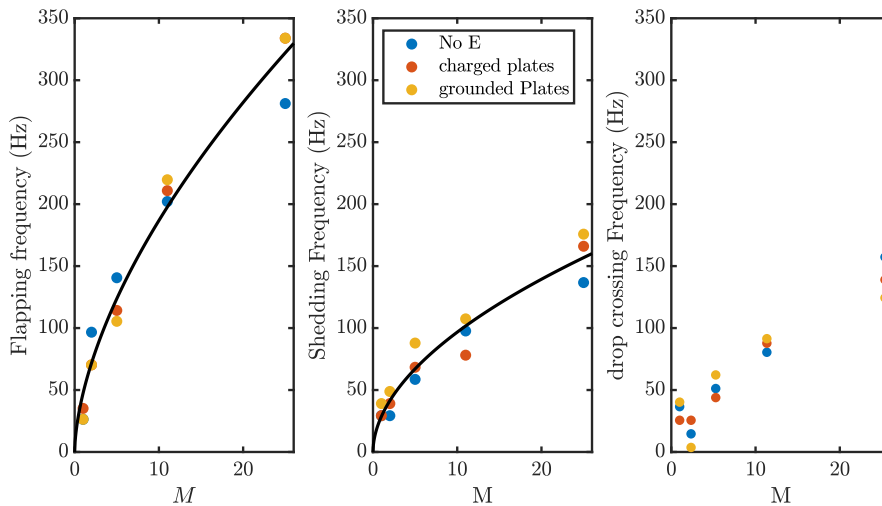
Figure 2.10:   : Flapping (left), shedding (center) and drop crossing (right) frequencies. It is worth noting that the flapping frequency is about twice both the shedding and drop crossing frequencies.

2.2.3   Empirical Dispersion Relations

In order to investigate whether the electrostatic forcing modified the dynamics of smaller scale features of the primary breakup, we computed empirical dispersion relations (Fig. 2.11). As expected for all the conditions, longer wavelengths (smaller wave numbers) corresponded to lower frequencies. More interestingly, the empirical dispersion relations clearly captured the faster dynamics prevalent at all length scales as the momentum ratio increased. Moreover, for the momentum ratio of 1, the empirical dispersion relation did reveal that the axial electric field resulted in faster dynamics at smaller scales. However, at higher momentum ratios, no configuration of the electric field resulted in noticeable changes in the dispersion relations.
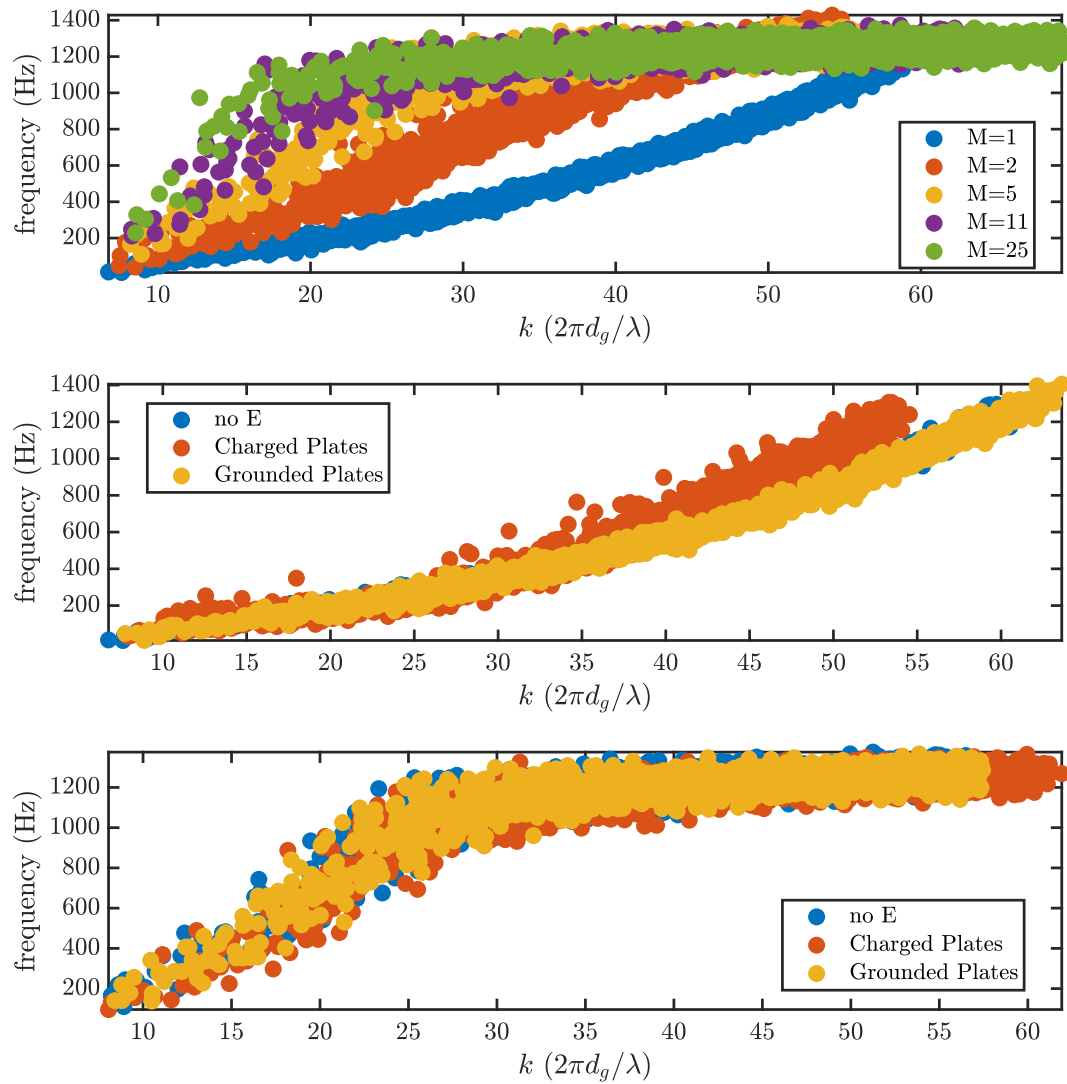
Figure 2.11: Empirical dispersion relation. As a function of M (top) and electric field for M=1 (middle) and M=5 (bottom).
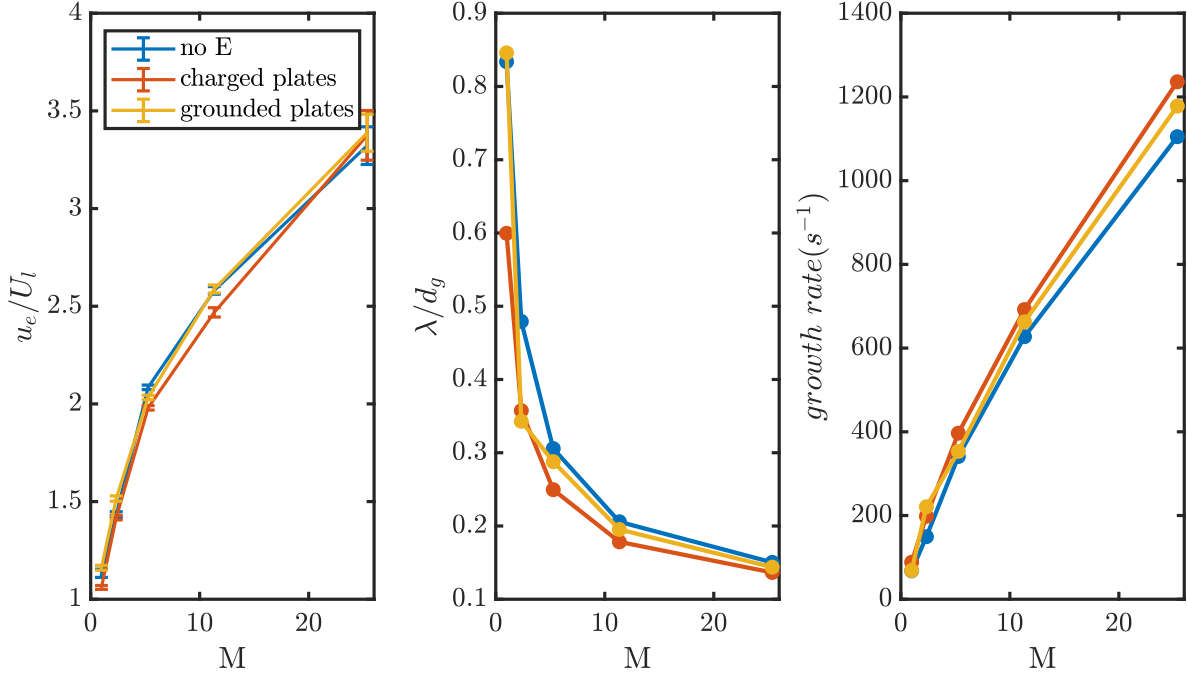
Figure 2.12: Entrainment velocity normalized by the mean liquid injection velocity, U_l, (left), wavelength of interfacial disturbances (middle) and growth rate of disturbances (right). The error bars are the standard error of the mean.

2.2.4 Initial Interfacial Instabilities

Along with the global characterizations of the spray, we explored the dynamics of the initial interfacial disturbances by tracking their position to evaluate their velocities, as well as their characteristic wavelengths. The entrainment velocity clearly increases with momentum ratio but appears unaffected by the electric field (figure 2.12). In contrast, the wavelength of these interfacial disturbances follows the same trend as the core length, with the charged plates configurations exhibiting systematically shorter wavelengths than the other two configurations. These two trends result in estimated growth rates that are always faster in the presence of the axial electric field.
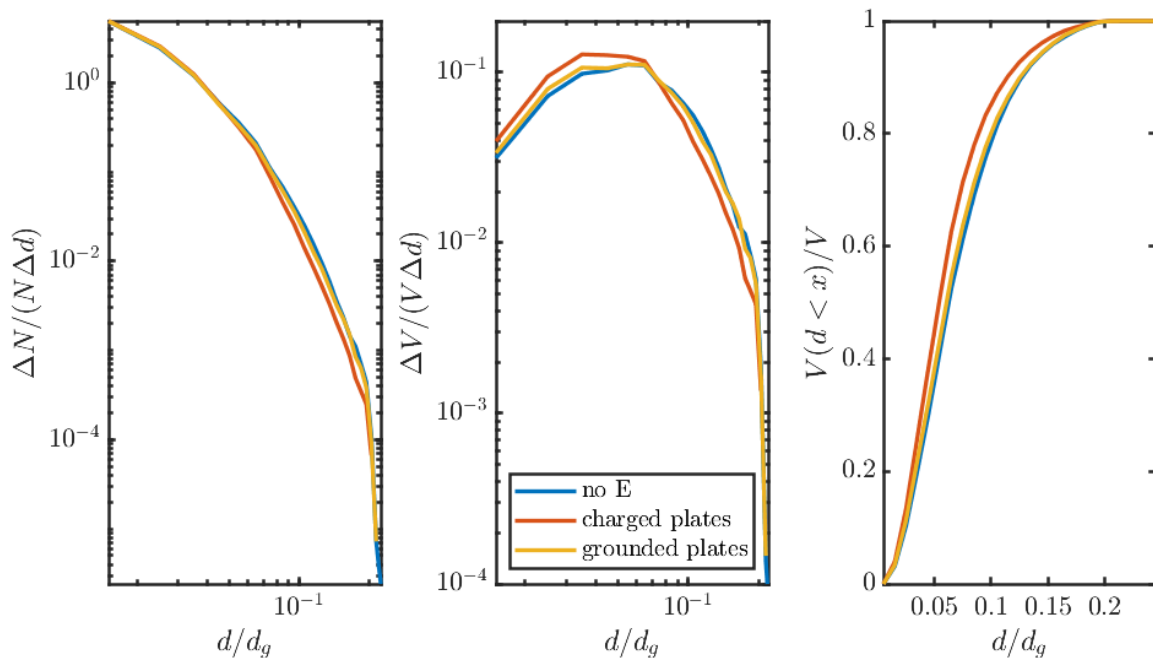
Figure 2.13: Drop size distributions for the three configurations at a momentum ratio of 5. Arithmetic drop diameter distribution (left), volume-weighted distribution (center) and volume weighted cumulative distribution (right).

2.2.5 Droplet Population Characterization

Finally, we performed optical identification of drop sizes in order to compute drop size distributions. As seen in Figure 2.13, there are small differences in the tails of the mean diameter distributions, indicating a smaller fraction of large drops in the presence of the axial electric field. The differences in the volume-weighted distributions are more noticeable and clearly show that smaller drops are a larger proportion of the total spray volume flux for the axial electric field case.

The small difference in the arithmetic drop distribution seen above was observed through most experimental conditions (except at the lowest momentum ratio) and can be expressed in terms of the arithmetic mean diameter (Figure 2.14). Higher moments of the drop size

distribution, however, were smaller in the presence of the axial electric field as compared with the other two configurations. In particular, the d_{43} values for the radial and axial electric field configurations were about 2% and 14% smaller than the values without electrostatic forcing, respectively, over the whole range of M explored here.
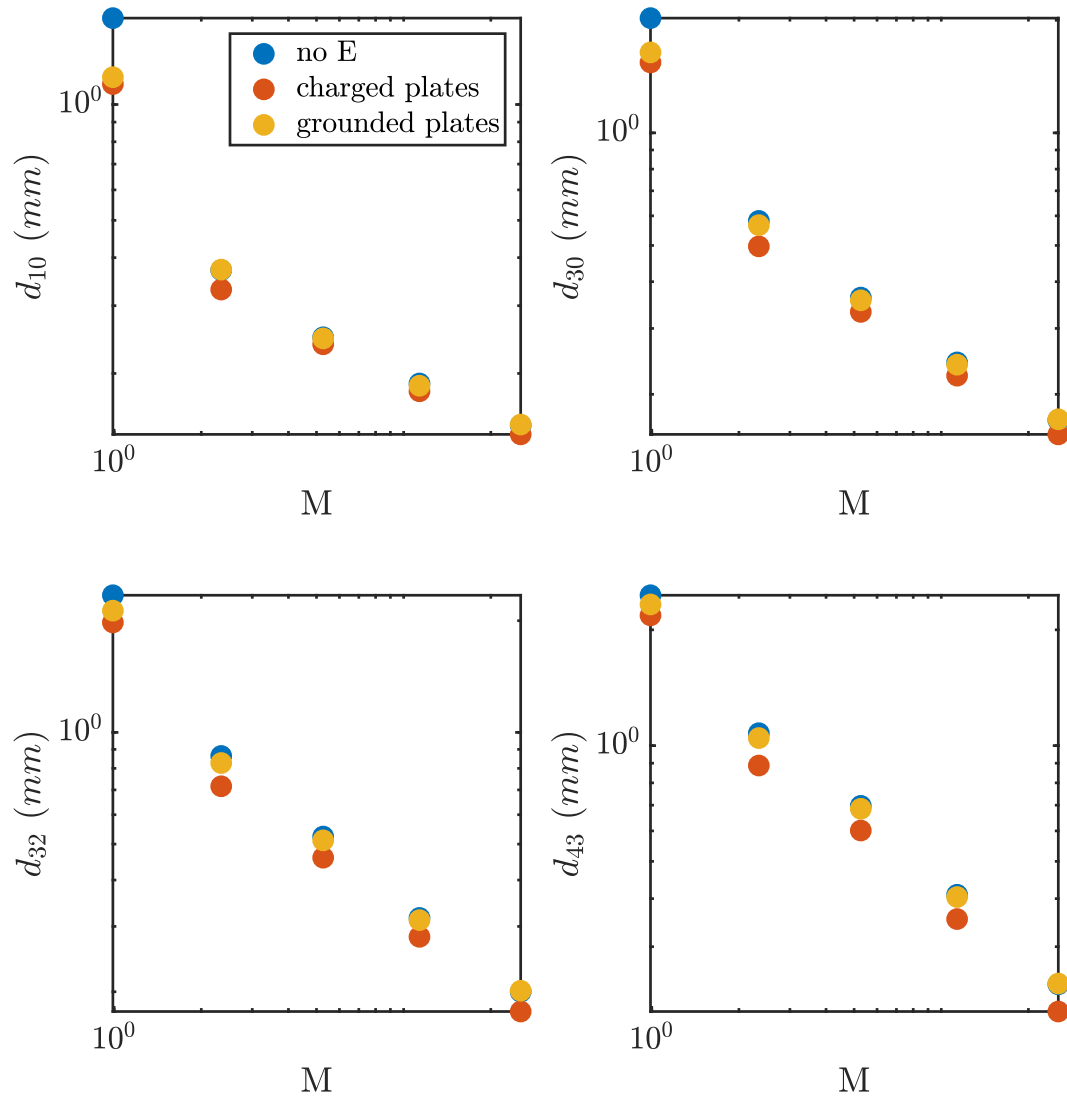
Figure 2.14: Drop mean diameters, (top-left) d_{10} arithmetic mean diameter;(top-right) d_{10} volume mean diameter;(bottom-left) d_{32} Sauter (area-weighted) mean diameter;(bottom-right) d_{43} De Brouckere (volume-weighted) mean diameter.

2.3 Discussion

Observations of the liquid core dynamics of coaxial atomization under electric field revealed that axial electric fields can significantly alter the wavelength and growth rate of interfacial instabilities, as well as notably shorten the liquid core lengths and reduce the mean drop diameters. This effect was observed to persist up to much higher momentum ratios than had been explored before in electrostatic atomization, where the ratio of electrostatic to aerodynamic forces (as estimated from the electrical Euler number and the momentum ratio) was well below unity (about 10^{-3}). These observations are consistent with linear stability analysis in the literature[35], whereby an axial electric field in the presence of surface charge increases the growth rate and shortens the wavelength of the interfacial instabilities.

Pertaining to the initial growth of interfacial instabilities, a shortcoming of the present work is that helical modes cannot be adequately characterized by two-dimensional shadowgraphy data. As indicated by earlier work [35, 61], electrostatically-assisted coaxial atomization presents strong helical modes in addition to the axisymmetric ones.

In contrast with what was observed for the initial interfacial instabilities and liquid core lengths, some of the more global metrics reveal little impact of the electrostatic forcing on the primary breakup dynamics. In particular, there was no discernible effect of the electrostatic forcing on the shedding and flapping frequencies, or on the characteristic frequency of the drop crossing times. Moreover, while the empirical dispersion relations clearly separate the dynamics for different momentum ratios, they only show noticeable change under the axial electric field at very low momentum ratios (of order unity). These observations suggest that the overall breakup dynamics are still dominated by aerodynamic forces.

A sizeable reduction in the mean drop diameters was observed under the axial electric field configuration. In particular, the reduction of the mean droplet diameter was largest for the higher moments of the distribution (volume-weighted or volumetric flux-weighted) indicating a difference caused by the electric field in the reduction of the largest drops formed by inefficient aerodynamic atomization. The histograms of the droplet diameter clearly confirm

this effect: a deficit in the number of the largest drops in the distributions. As shown by earlier work [2], the mean diameter of the resulting droplet population is proportional to the wavelength of the interfacial instabilities, a conclusion consistent with the observations presented in this work.

2.4   Conclusions

Electrostatic forcing is shown to noticeably impact the primary atomization in a coaxial atomizer, especially if the electric field is predominantly radial at the liquid nozzle exit. Our observations are consistent with the presence of Maxwell stresses that accelerate the liquid jet towards the turbulent gas stream, which would lead to an increased efficiency in the kinetic energy transfer from the gas and the liquid. Furthermore, these effects persist at higher momentum ratios than had been studied in the past. The Maxwell stresses, resulting from an electric field with strong axial component, were observed to shorten the wavelength of the interfacial instabilities, leading to shorter liquid core lengths and smaller droplet diameters. In contrast, an electric field with a radial component of similar strength, but smaller axial component, did not have such an impact on the length scale of the interfacial instabilities. More research is necessary to optimize the electric field characteristics that maximize the mechanical coupling between the phases, for improved atomization.

Chapter 3

EFFECT OF ELECTRIC FIELD INTENSITY ON PRIMARY BREAKUP FOR COAXIAL SWIRLING ATOMIZATION

The experimental results presented in the last chapter give a clear indication of the possibilities of electrostatic stresses in modifying the growth of the primary instabilities in two-fluid coaxial atomization. In particular, we observed that electric fields with a strong axial component that accelerates the liquid in a direction opposite of the flow were most effective in shortening the wavelength and increasing the growth rate of the initial interfacial instabilities an resulted in shorter liquid core lengths.

Unfortunately, although such an arrangement of the electric field proves useful in aiding in the atomization of the liquid jet, it is not the most amenable for utilization in multiphysics control of atomization for two main reasons. An electric field that accelerates the liquid in a direction opposite of the main flow direction can lead to loss of some of the liquid volume being transported downstream. More, critically said transported drops can be deposited in the gap between the two electrodes leading to arc discharges across them. In order to address this shortcomings, it is possible to increase the distance between the electrodes while increasing the potential drop so as to maintain strong electric fields. Finally, it is desirable for the electrostatic field to have a strong radial component so as to increase the transport of droplets away from the center line to achieve a more radially uniform liquid distribution.

3.1 Methods

The atomization system studied consists of a canonical two-fluid coaxial atomizer exposed to large electric fields generated by a set of two parallel plates held at high voltage. Figure 3.1 shows a schematic of the system with the most relevant physical dimensions, as well

as the results of a Finite Element Method simulation illustrating the voltage and electric fields in the atomization region. Atomization was achieved by exposing the laminar liquid jet, ($Re_l = 1,200$), emerging from the liquid nozzle to a turbulent coaxial gas stream and a strong electric field. The working fluid was a mixture of water and sodium chloride with a conductivity of $126 \pm 6\mu S/cm$ and the working gas was standard air. The main non-dimensional groups that characterize atomization and transport in the system under study include: the liquid and gas Reynolds numbers ($Re_i = U_i d_i/\nu_i$), the gas-to-liquid momentum ratio($M = \rho_g U_g^2/\rho_l U_l^2$), the electrical Euler number ($Eu = \epsilon_0 E_0^2/\rho_l U_l^2$) and the ratio of hydrodynamic time scales to the electrical relaxation time $T = \sigma_l d_l/\epsilon_0 U_l$, where $U, \rho, \nu, d_i, \epsilon_0, E_0$,and σ_l are the average exit velocity, density, kinematic viscosity, nozzle diameter, permittivity of free space, electric field strength, and electrical conductivity, and the subscripts l and g denote the liquid and gas phases, respectively. The average velocities are calculated from the volume flow rate and the cross-sectional area of the nozzle exit and the diameters are the liquid nozzle inner diameter and the gas nozzle effective diameter. The electric field strength can be approximated from the solution for the electric field between two concentric cylinders held at a potential difference ΔV, namely, $E_0 = \Delta V/r_l \ln(R/r_l)$ where r_l is the liquid jet radius (estimated as half the liquid nozzle diameter) and R is the distance from the liquid jet to the plates (the estimates using this solution are in good agreement with the FEM simulations). We explored momentum ratios up to 100 (corresponding to a gas Reynolds number up to 92,700), swirl ratios between 0 and 1, voltages up to 90 kV corresponding to electric Euler number up to 10.

We estimated the bulk volumetric charge density from the liquid volume flow rate and the current emanating from the liquid nozzle. The current was measured with a digital multimeter with nanoampere precision and temporal resolution of the order of a millisecond.

Figure 3.2 details the results of the FEM simulation in more detail. Notice that both the axial and radial components of the electric field decay away from the nozzle at comparable rates and the maxima of each component at each downstream location is of the same order of magnitude. More importantly, the electric field profile decays much more slowly than
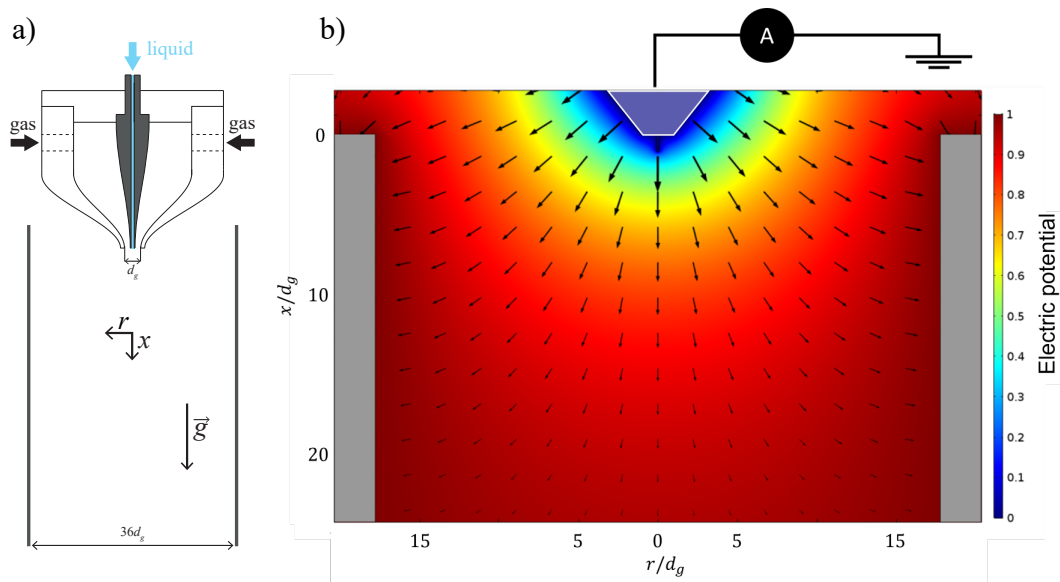
Figure 3.1: (left) Side cut of the experimental setup, the atomizer sits between two large metallic plates to which a high voltage is applied. The outer diameter of the gas nozzle is $d_g = 1$ cm and the plates are approximately 36 d_g apart. (right) Finite Element Method (FEM) simulation of the voltage and electric field vectors for a simplified geometry for the nozzle (shown in white outline). The nozzle is grounded through an ammeter to measure the current emanating from it.
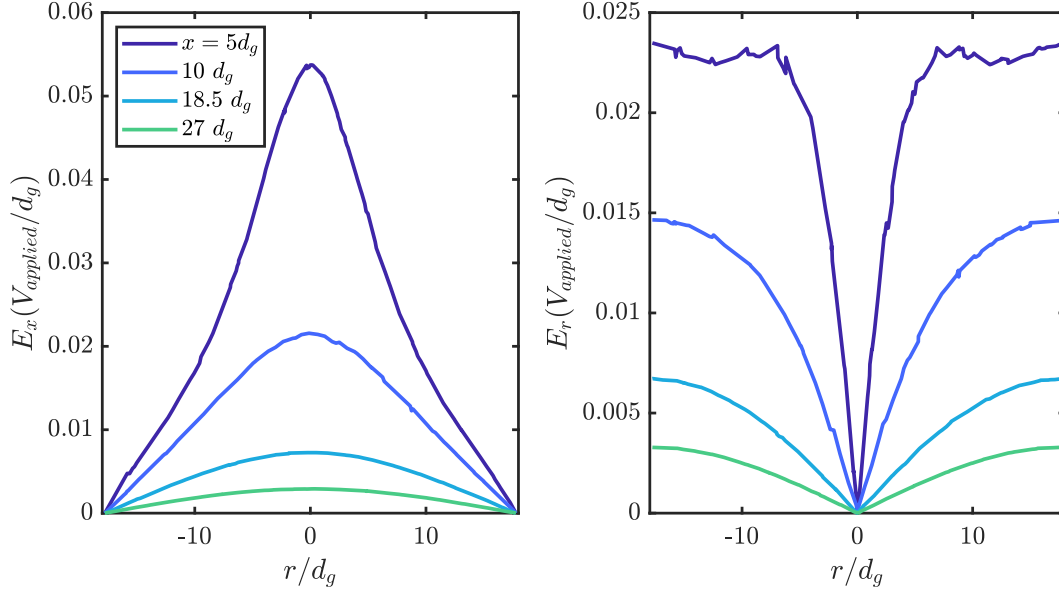
Figure 3.2: Radial profiles of the axial (left) and radial (right) components of the electric field for three axial locations downstream from the nozzle. The profiles are the result of interpolation from the FEM simulation shown in figure 2.2.

a radially divergent electric field (e.g. what would obtain if the nozzle was held at high potential relative to a distant ground), and the radial component of the electric field does not decay radially. These observations are more relevant to the transport of the charged particles in the midfield. Very close to the nozzle the electric field is dictated by the complex geometry of the liquid jet, but in general the strong potential gradients in that region will lead to an electric field pointing axially and radially away from the nozzle.

3.2 Curvature Measurements

In addition to the metrics characterizing the large scale geometry of the spray (intact length, spreading angle and virtual origin) and the dynamics of these large features (flapping and shedding frequencies) that were described in the previous chapter we computed metrics from the identification of the instantaneous liquid jet core morphology. After the liquid jet was

identified the arc length at each point was computed from the distance between consecutive points and this arc length was used to represent the contour of the jet as a parametrized curve (see figure 3.3. The sum of the local arc length measurements are a proxy for the total interfacial length between the gas and the liquid phase in a plane. Cubic splines (that ensure continuity of the second derivative) were fitted to the two spatial coordinates as a function of arc length and the derivatives were computed from the spline polynomials. These derivatives give the two dimensional curvature as: $curvature = (x'y'' - y'x'')/(x'^2 + y'^2)^{3/2}$, where the prime denotes the derivative relative to arc length parameter.

The total arc length was also used to characterize the presence of small scale features in the liquid core. To this end we obtain the average of the ratio of the instantaneous arc length to the instantaneous liquid core length. This ratio approaches 2 for a long cylinder and π for a pending drop, and increases with increasing tortuosity of the curve enclosing the image of the liquid core.
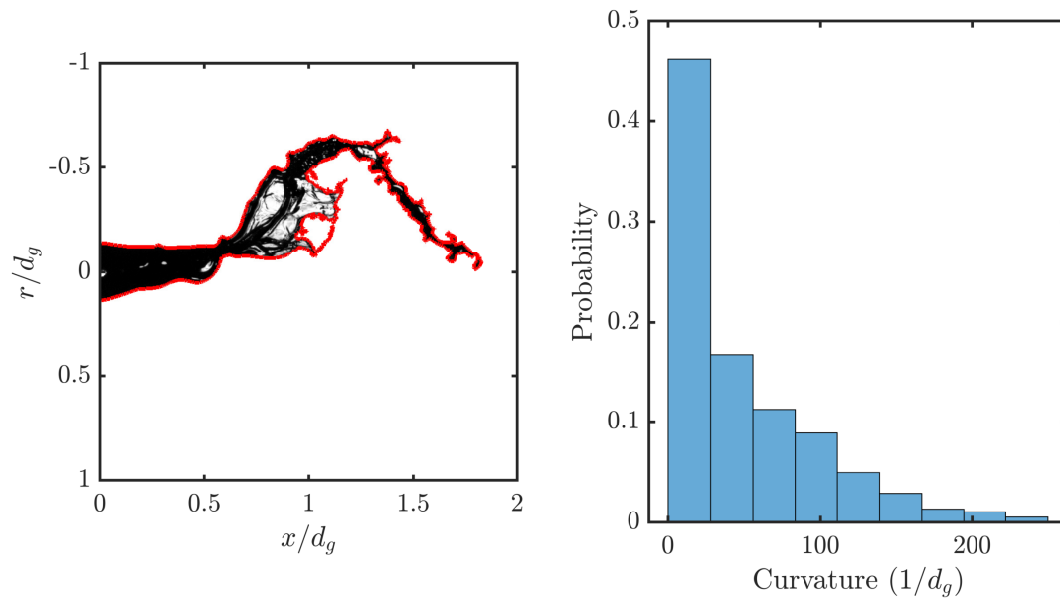
Figure 3.3: Illustration of curvature calculation. The liquid jet is identified from the backlit images and the surface approximated using a piecewise cubic spline, shown in red here (left). The derivatives in two spatial directions relative to the arc length parametrization are used to estimate the curvature along the liquid jet profile, the probability distribution of the curvature from the image on the left is shown in the right.

3.3   Results

Purely electrostatic breakup was achieved for sufficiently large electric field strengths. As shown in figure 3.4, starting with a laminar liquid jet the breakup absent electrostatic forcing is characterized by the well established Plateau-Rayleigh mechanism (figure 3.4 a). As the electric field strength is increased, we first observe slight deviations form this Plateau-Rayleigh breakup (figure 3.4 b), with the formation of Taylor cones and tip streaming after the formation of a drop. Further increases in electric field strength (figure 3.4 c) lead to the formation of helical or whipping instabilities, and even further increases in electric field strength significantly reduce the liquid intact length (figure 3.4 d). In all of this cases even though droplets with diameters orders of magnitude smaller than the liquid jet radius are formed, it appears that the bulk of the liquid volume is carried by big drops (with diameters of similar magnitude as the liquid jet).

As can be observed in figure 3.5 the breakup dynamics are radically changed due to the gas co-flow. At low gas-to-liquid dynamic pressure ratios ($M = 1$ in figure 3.5 a and b) in the absence of electric field the breakup resembles an enhanced Plateau-Rayleigh Breakup (figure 3.5 a). In stark contrast the electric field at 90 kV leads to the occurrence of bag breakup (figure 3.5 b) and much smaller drops. As the gas co-flow is increased the aerodynamic stresses clearly dominate the large scale geometry of the breakup (e.g. at $M = 5$ in figure 3.5 c and d) but the electric field introduces many small scale features, for instance the ramified structure shown in the red square in figure 3.5 d.

We quantify the large scale geometry of the liquid core using the metrics described in the previous chapter, namely, the liquid intact length (L_b), the spreading angle (θ) and the axial location of the virtual origin (x_{VO}). Changes in these metrics indicate a strong effect of the electrostatic forcing mostly for the two lowest momentum ratios (1 and 2). Moreover, the effects due to electrostatic forcing were more noticeable at low swirl ratios.

The liquid intact length was observed to decrease with increasing applied voltage for the lowest momentum ratio ($M = 1$) for all values of the swirl ratio tested, for $M = 2$ for swirl
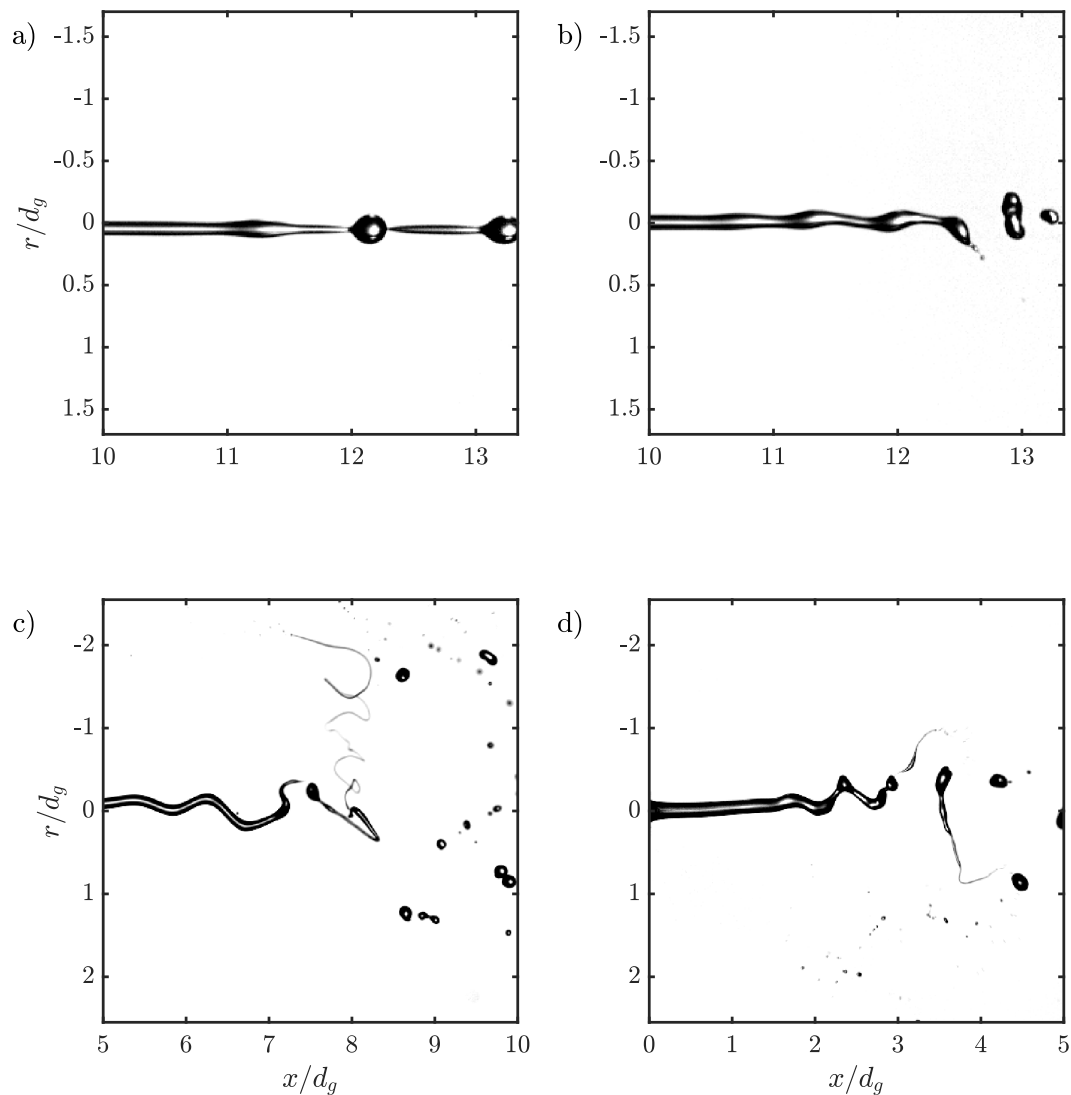
Figure 3.4: Snapshots of electrostatic atomization without gas co-flow at applied voltages of 0 (a), 30 (b), 60 (c) and 90 kV (d). We can see that the electric field modifies the main breakup mechanism with features that are not observed in any atomizing conditions without EHD forcing.

ratios up to 0.5 and for $M = 5$ and no swirl. The effect of the electrostatic forcing for larger momentum and swirl ratios was negligible as shown in figure 3.6 (left). As can be seen in
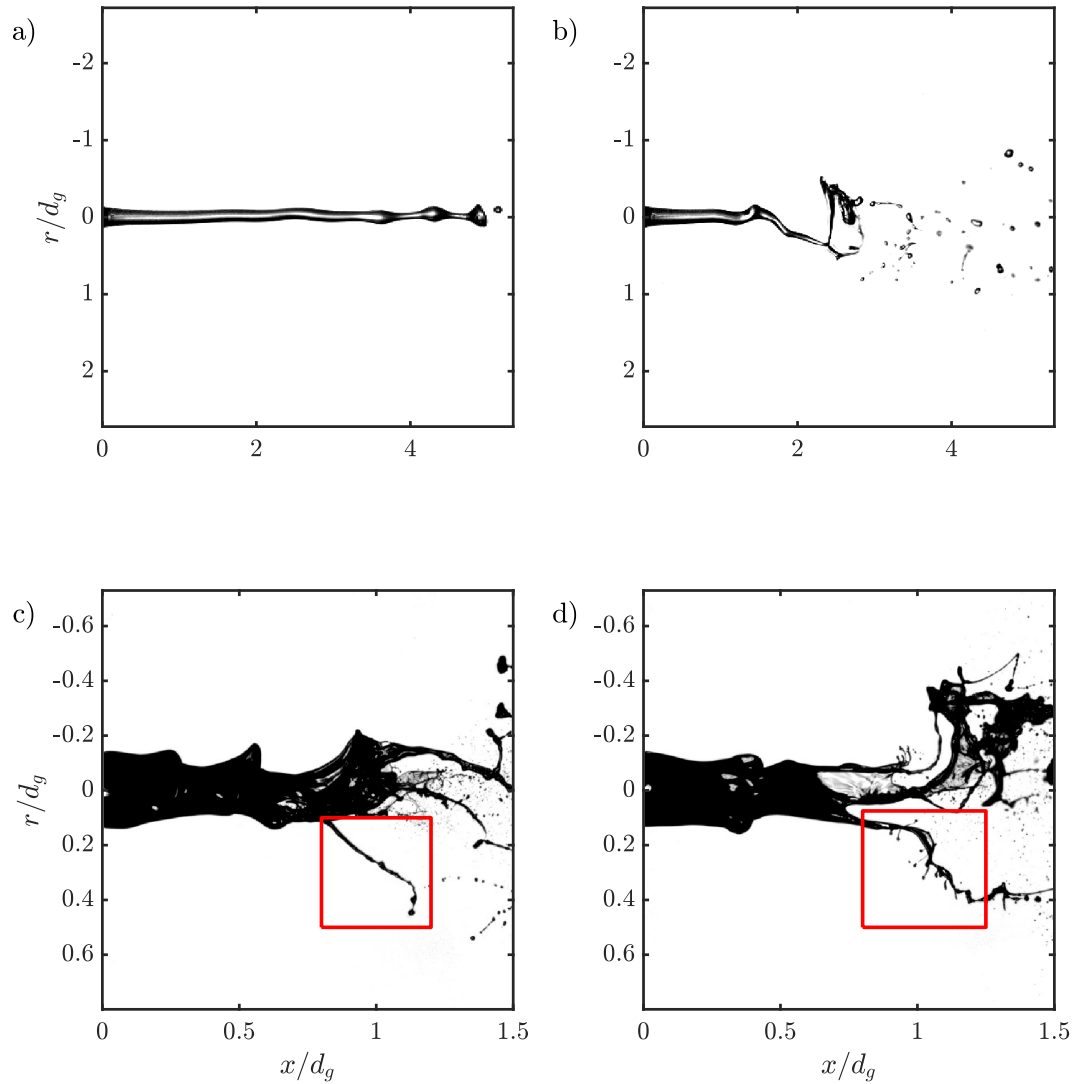
Figure 3.5: Snapshots at Momentum ratios of 1 (top) and 5 (bottom) and applied voltages of 0 (left) and 90 kV (right). We can see that the electric field modifies the main breakup mechanism at low momentum ratios. At high momentum ratios the main effect of the electrostatic field is at a smaller length scale.
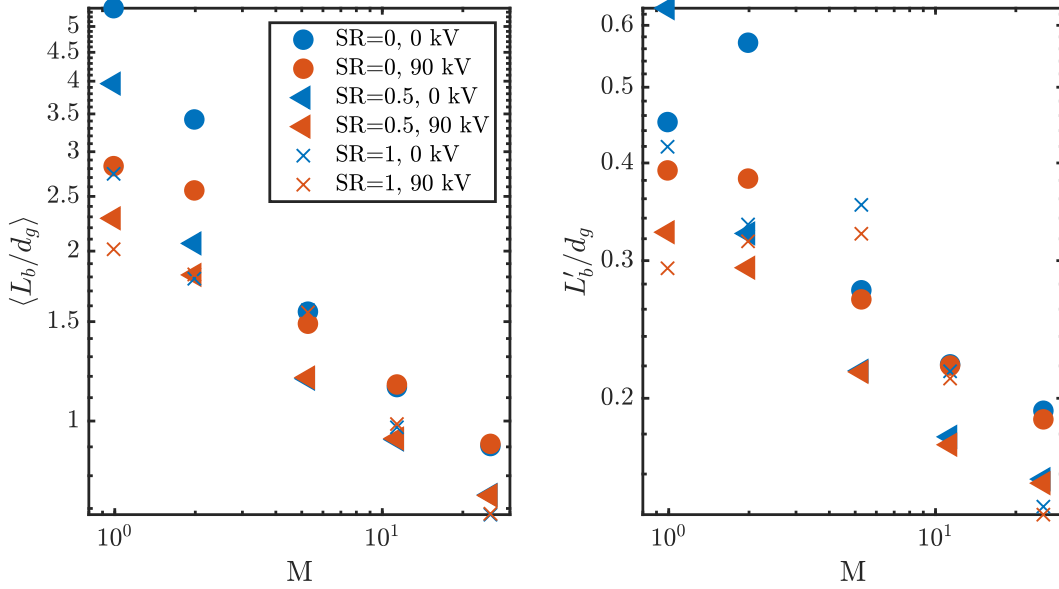
Figure 3.6: Mean intact length (left) and standard deviation of the intact length (right) as a function of Momentum for swirl ratios of 0, 0.5 and 1 and voltages of 0 and 90 kV.

figure 3.6 (right) the effects on the variance of the liquid intact length due to electrostatic forcing were similar to the effects on the mean intact length.

As the electric field induced much stronger breakup at a momentum ratio of one, the spreading angle was substantially increased (figure 3.7, left) and the virtual origin position approached the nozzle (figure 3.7, right). Similar effects were observed for $M = 2$ at sufficiently low swirl ratio (less than half). At higher swirl or momentum ratios the values of spreading angle and x_{VO} were very similar regardless of the applied voltage. These results indicate that the mean liquid distributions in the near field at momentum ratios larger than about 5 were very similar with and without electrostatic forcing.

In addition to characterizing the geometry of the average liquid distribution of the spray, we quantified the two most prominent frequencies of the liquid core dynamics. As can be seen in figure 3.8 electrostatic forcing was only seen to significantly increase the flapping frequency at low momentum and swirl ratios. On the other hand the shedding frequency
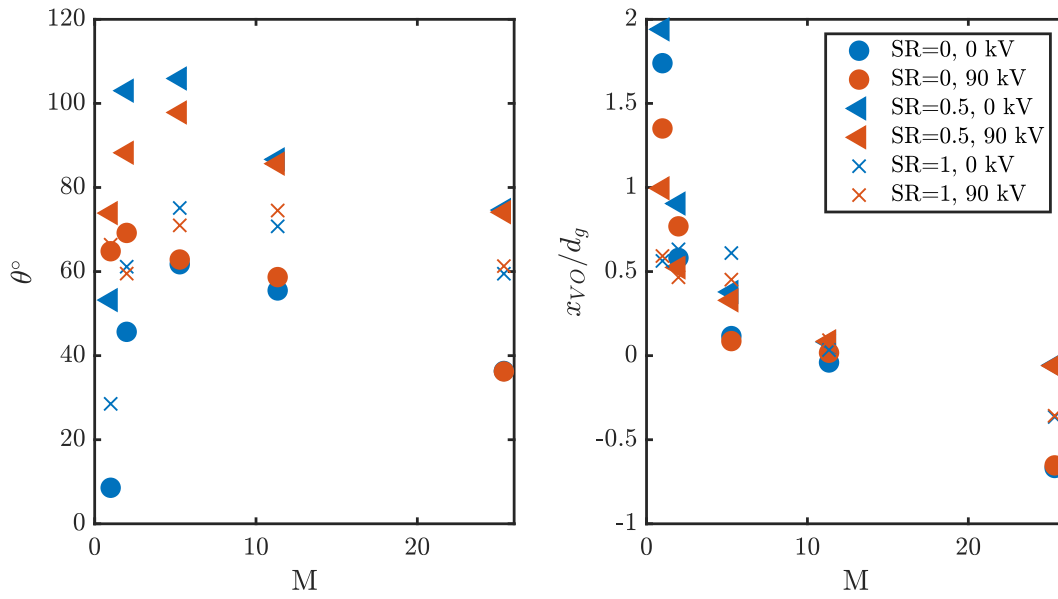
Figure 3.7:   Spreading Angle (left) and axial location of the virtual origin (right) as a function of Momentum for swirl ratios of 0, 0.5 and 1 and voltages of 0 and 90 kV.
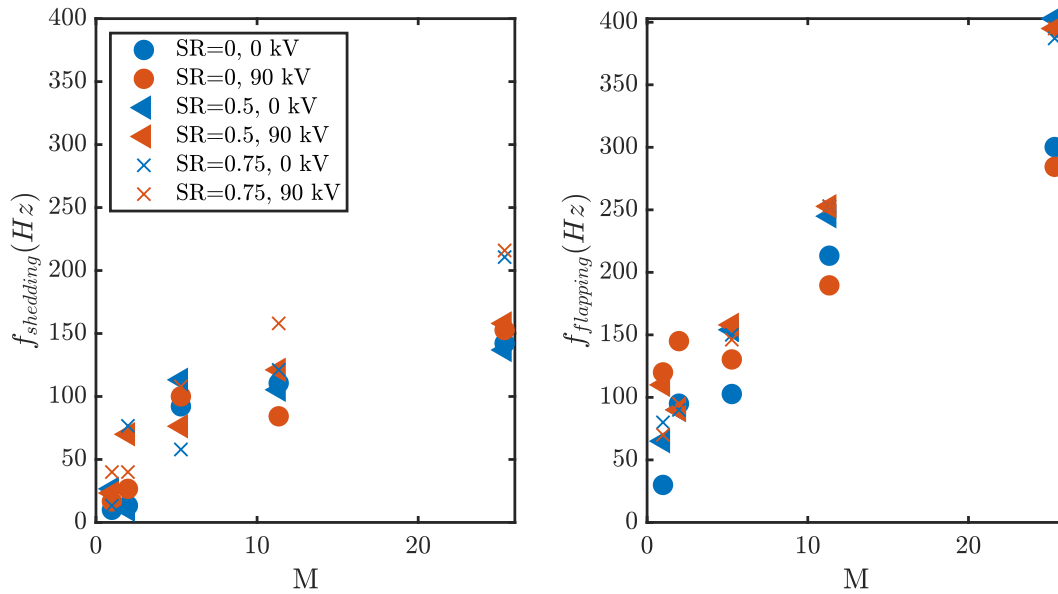
Figure 3.8:   Shedding (left) and flapping (right) frequencies as a function of momentum for swirl ratios of 0, 0.5 and 0.75 and voltages of 0 and 90 kV.
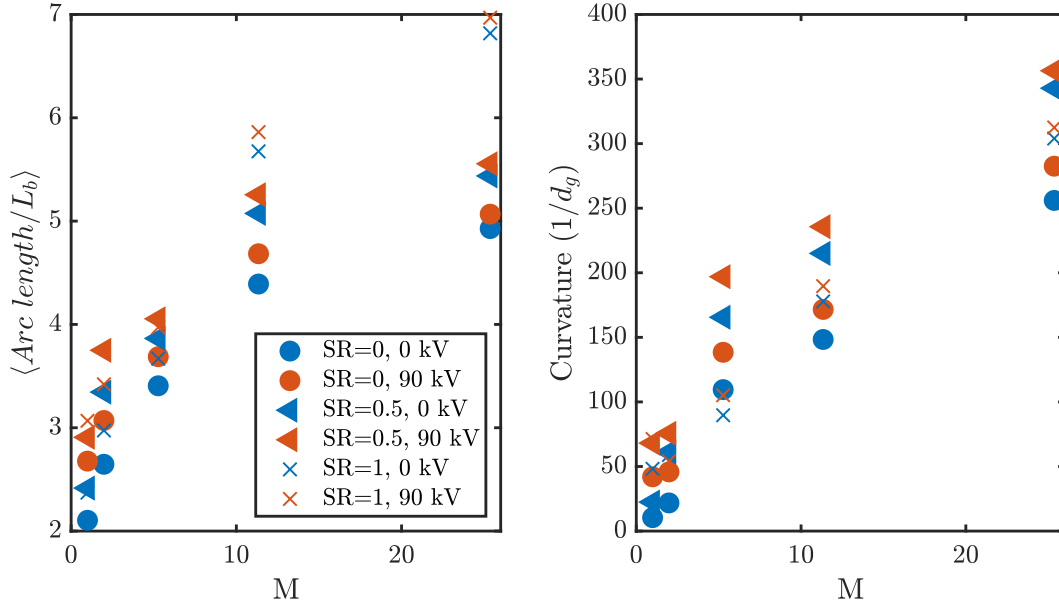
Figure 3.9: Mean value of the ratio of instantaneous total arc length to intact length (left) and median of the mean curvatures (right) as a function of Momentum for swirl ratios of 0, 0.5 and 1 and voltages of 0 and 90 kV.

(which is the timescale associated with evolution of the intact length) appeared to be mostly unaffected by the electrostatic forcing.

So far results indicate that the large scale average distribution of the liquid in the near field is only affected at low momentum and swirl ratios. In contrast two metrics that depend on smaller scale features show differences due to electrostatic forcing across the swirl and momentum ratios explored. Figure 3.9 shows the mean ratio of arc length to intact length (left) and mean curvature (right). Both of these metrics shows consistent increases due to electrostatic forcing across the conditions explored, the only exceptions being the changes in curvature for $M = 2$ and $SR = 1$ (figure 3.10). The mean ratio of arc length to intact length was observed to increase for all momentum and swirl ratios, with the largest increases being around 30% for the smallest momentum and swirl ratios. Moreover, this ratio increased monotonically as a function of applied voltage in an approximately linear fashion.
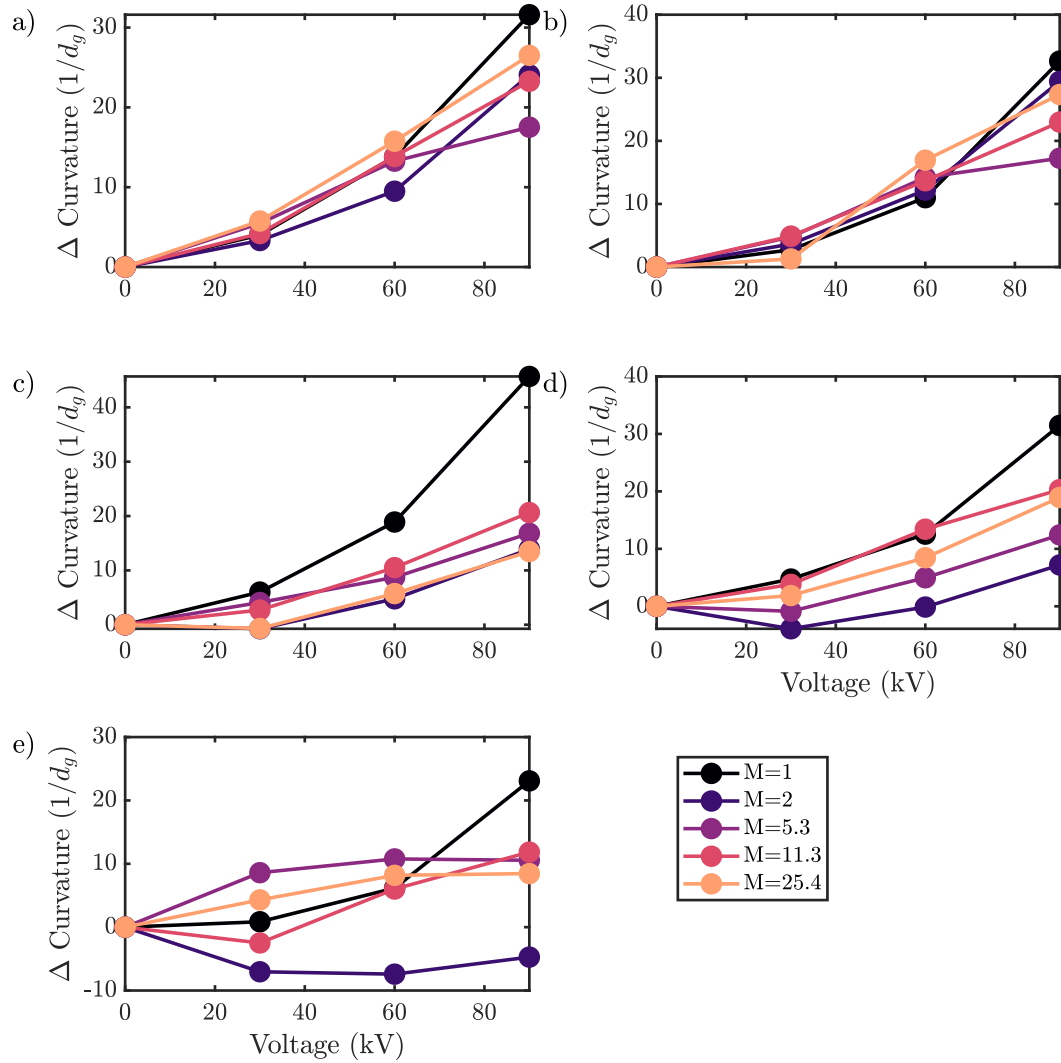
Figure 3.10: Changes in the median of mean curvatures (relative to the case with no electric field) as a function of applied voltage for the five momentum ratios and for swirl ratios of 0, 0.25, 0.5, 0.75 and 1 (a, b, c, d, e, respectively).
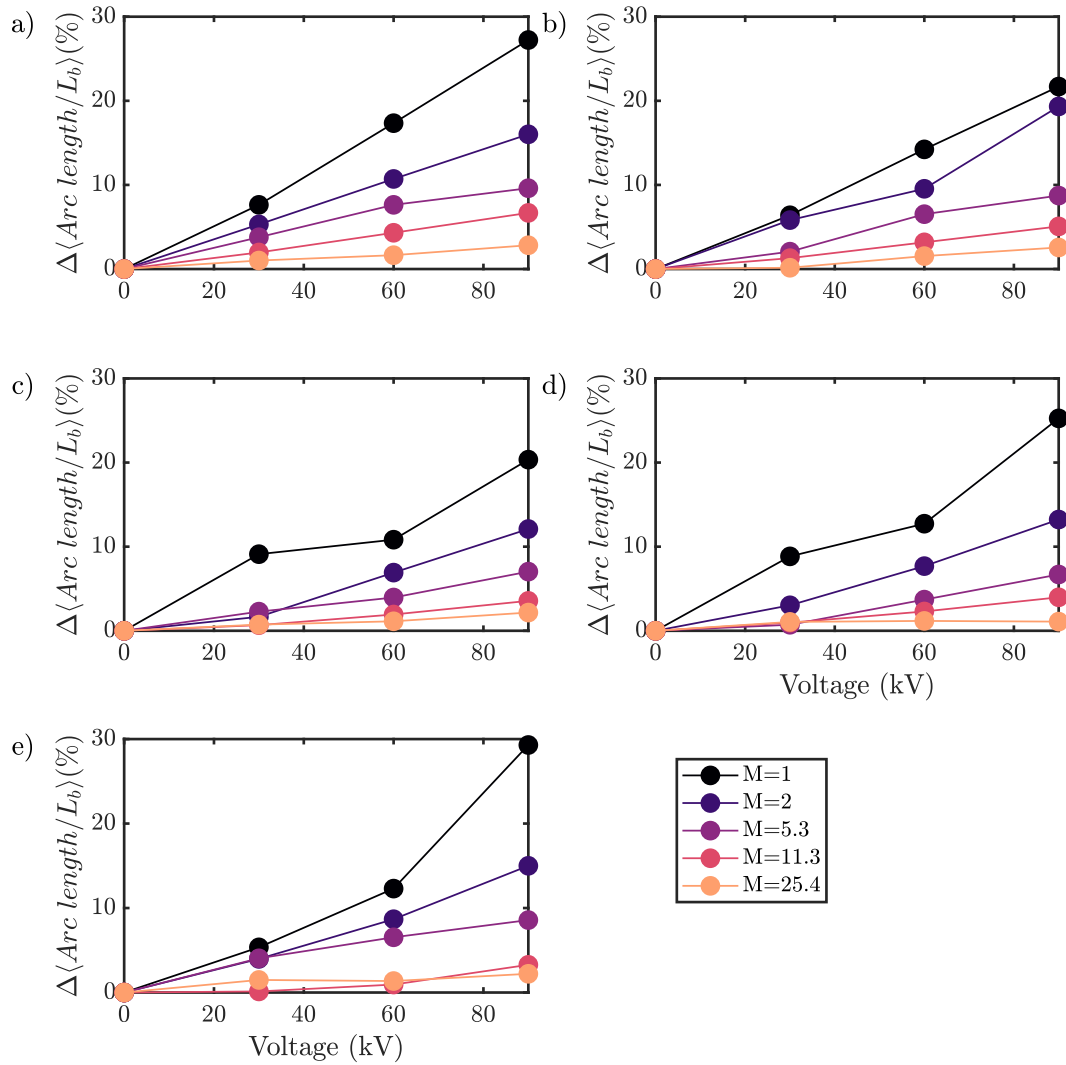
Figure 3.11: Percent changes in the mean ratio of total arc length to intact length (relative to the case with no electric field) as a function of applied voltage for the five momentum ratios and for swirl ratios of 0, 0.25, 0.5, 0.75 and 1 (a, b, c, d, e, respectively).

3.4 Electrostatic Forces Modify the Breakup Mechanisms in Coaxial Atomization

The experimental results presented here indicate that electrostatic breakup in conducting electrolytic solutions can be the dominant breakup mechanism in electrostatically assisted coaxial atomization. We observe a transition as the gas-to-liquid dynamic pressure ratio is increased to about half the maximum electric Euler number where the aerodynamic breakup dominates the large scale features of the liquid core deformation, including the intact length and the spreading angle. Increasing the swirl ratio also lowers the value of the gas-to-liquid dynamic pressure ratio at which this transition occurs.

In contrast with the transition described above, the electrohydrodynamic forces change the breakup mechanisms at smaller scales. Following the growth of flapping and Kelvin-Helmholtz instabilities, the resulting sheets and ligaments exhibit features characteristic of electrohydrodynamic breakup, such as tip-streaming, helical whipping and branching. The small scale features provide regions of high electric potential gradients, and thus strong electric fields and electrostatic forces that can give rise to regimes of electrohydrodynamic breakup that were not observed in the absence of gas co-flow, such as the ramified breakup shown in figure 3.5. The formation of all of these small scales features was quantified using the curvature and arc length to intact length ratio of the liquid core. The metrics were seen to consistently increase with increasing applied electric potential.

This modification of small scale structures in the liquid core provide evidence of the capabilities of electrohydrodynamic forces in destabilizing the liquid jet in coaxial atomization even for high momentum ratios. Moreover, these observations indicate that the reduction of the mean drop diameters documented in the following chapters is at least in part due to the enhancement of the primary breakup through a drastic modification of the interfacial perturbations

Chapter 4

DROP SIZE AND VELOCITY STATISTICS OF ELECTROSTATICALLY ENHANCED TWO-FLUID COAXIAL ATOMIZATION

We present the results of an experimental investigation of electrostatically assisted atomization using Phase Doppler Particle Analysis (PDPA) over a wide range of gas-to-liquid momentum ratios ($M = 5 - 100$) and for voltages up to 75 kV. Electrostatic forcing on the spray were observed to increase both the axial and radial components of the droplets' velocities, with a much more pronounced increase in the radial velocity. We also observed a decrease in the characteristic droplet diameter, that is approximately linear with increasing applied voltage. Moreover, the radial droplet distributions indicate transport of droplets in the radially outwards directions, leading to flatter profiles of the mean diameter. Our results are consistent with the trajectories of droplets with charge densities that are a decreasing function of droplet size.

4.1 Phase Doppler Particle Analyzer

We obtained measurements of droplets' axial and radial velocities using Laser Doppler Velocimetry (LDV) simulataneously with measurements of the droplet diameters from Phase Doppler Interferometry (PDI). We used the TSI LDV/PDI system (FSA4000 Signal Processor, PDM1000 Photo Detector Module) in backward scattering with reflection as the dominant mode at an observation angle of 150°. This system can reliably record droplet sizes between approximately 1.5 and 350 microns. The system operates with two laser beams (green and blue with wavelengths of 514.5 nm and 488 nm respectively), where one of the lasers provides both the diameter measurements and the axial velocity measurements and

the other light wavelength signal provides the radial velocity measurements. As the measurements of the two components of the velocity are not ensured to be simultaneous, a coincidence matching algorithm was run to assign radial velocities to size measurements based on the timing of the measurements (to within 50 microseconds interarrival time difference between blue and green beams).

The PDPA system performs measurements in a small probe volume defined by the emitter and receiver optics as well as by the gaussian profile of the laser beams. We estimated the probe area and probe volume following the methods described in previous work and summarized in equations 4.1 and 4.2 below.

$$A_{probe} = wL = \frac{ws}{|\beta|sin\theta} \tag{4.1}$$

$$V_{probe} = \frac{\pi}{4}w^2L = \frac{\pi}{4}\frac{w^2s}{|\beta|sin\theta}, \tag{4.2}$$

where the projected probe length L is given by $L = s/\beta sin\theta$, and β is the magnification factor computed from the lenses in the receiver, s is the size of a spatial filter in the receiver and θ is the detection angle. For our study here, $\beta = 250/750$, $s = 150\mu m$ and $\theta = 150^o$. The probe volume has a size dependent width w that arises from the fact that the scattered light intensity depends on the droplet size and the laser beams have a gaussian profile, so that smaller droplets can only be observed when they are closer to the center of the beam. This size dependent probe volume width is estimated from the axial velocity and the gate time of the droplets (the gate time is the residence time of the droplet in the probe volume). For the results shown here, the projected probe length was 900 microns and typical probe volume widths were between 150 and 600 microns, yielding a probe area of around half a square millimeter and a probe volume of about a quarter of a cubic millimeter.

Estimating the size dependent probe area is important not only for calculating fluxes and volume fractions but also because it helps correct for sampling biases as larger droplets are effectively being sampled over a larger sampling area. Thus, in our calculations of the droplet diameter statistics, we incorporate a weight that is inversely proportional to the size

dependent probe area width. We can express this in terms of the relative probability that a drop of size d_i will be observed at a given location can be estimated by:

$$p_i = \frac{N_i/w_i}{\sum_j N_j/w_j} \tag{4.3}$$

Where N_i is the number of observed drops in class i. Moreover, we estimated the statistics for the whole spray droplet population by compiling the samples collected radially. Thus, for the characterization of the global spray droplet population, we assign weights to the samples that depend on the cross section area of the spray represented by the measurement at a given point, as well as by the collection time for the measurements at that point, as described in equation 4.4.

$$p_i = \frac{\sum_j N_{ij} A_j/w_i T_j}{\sum_i \sum_j N_{ij} A_j/w_i T_j}, \tag{4.4}$$

where N_{ij} is the number of samples in particle class i collected at radial position j, T_j is the sampling time for the measurements at location j and A_j is the area across which we estimate the measurements at position j are representative. The areas A_j are annuli centered at a radial sampling location, except for the measurements at the centerline which are circles. Thus, we can estimate the droplet size distribution across the whole spray, in terms of the mean diameters:

$$d_{nm} = \left(\frac{\sum p_i d_i^n}{\sum p_i d_i^m} \right)^{1/(n-m)} \tag{4.5}$$

Of particular interest are the arithmetic mean, d_{10}, the surface-averaged mean, d_{20}, the volume-averaged mean, d_{30}, the Sauter mean, d_{32} and the volume flux-weighted mean d_{43} diameters.

4.2 Results

4.2.1 Volumetric Charge Density

Results of the volumetric charge density are shown in figure 4.1 . As expected, the charge density increased with increasing voltage and the behavior of the charge voltage curves could
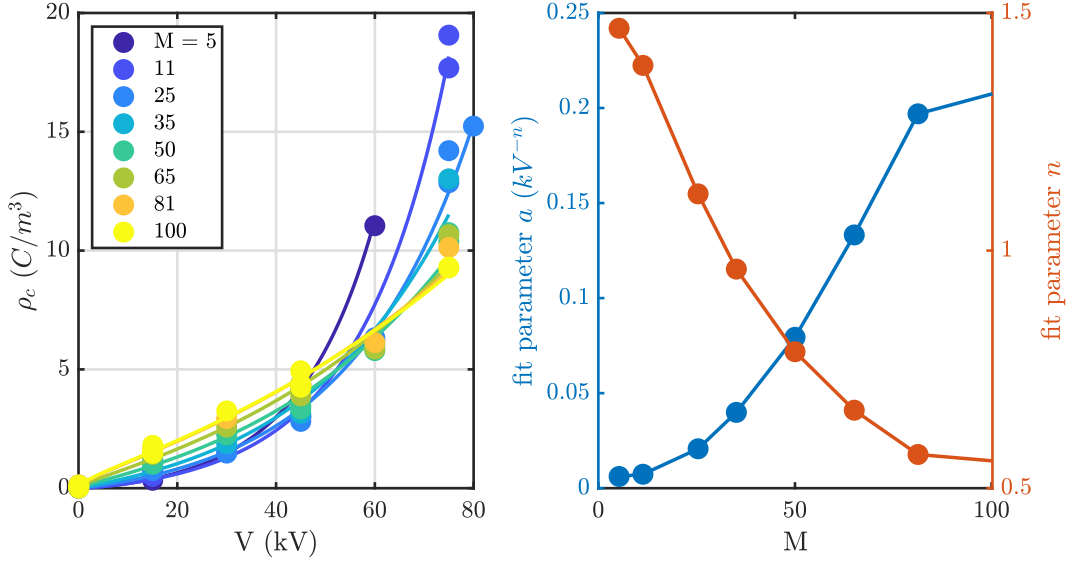
Figure 4.1: Electric charge volume density as a function of applied voltage for a range of momentum ratios (left). Estimated values of the parameters obtained by fitting the function in eqn. 4.6 (right).

be accurately approximated by a function of the form shown in equation 4.6. For values of applied voltage less than 60 kV, higher momentum ratios yielded higher charge densities, however this relationship was inverted at higher voltages. This behavior can be captured by an increase in the parameter a and a decrease in parameter n with increasing momentum ratio as shown in the right panel of figure 4.1.

$$\rho_c = e^{aV^n} - 1 \tag{4.6}$$

4.2.2   Velocity Profiles

In the absence of an electric field, the average droplet velocities closely resembled the self-similar profiles of a canonical turbulent round jet. Accordingly, we introduce here a normalization of $<u>$ and r by the centerline velocity $<u(r=0)>$ and the radial distance $r_{1/2}$ at which the velocity value become half of the centerline value, respectively. As shown in
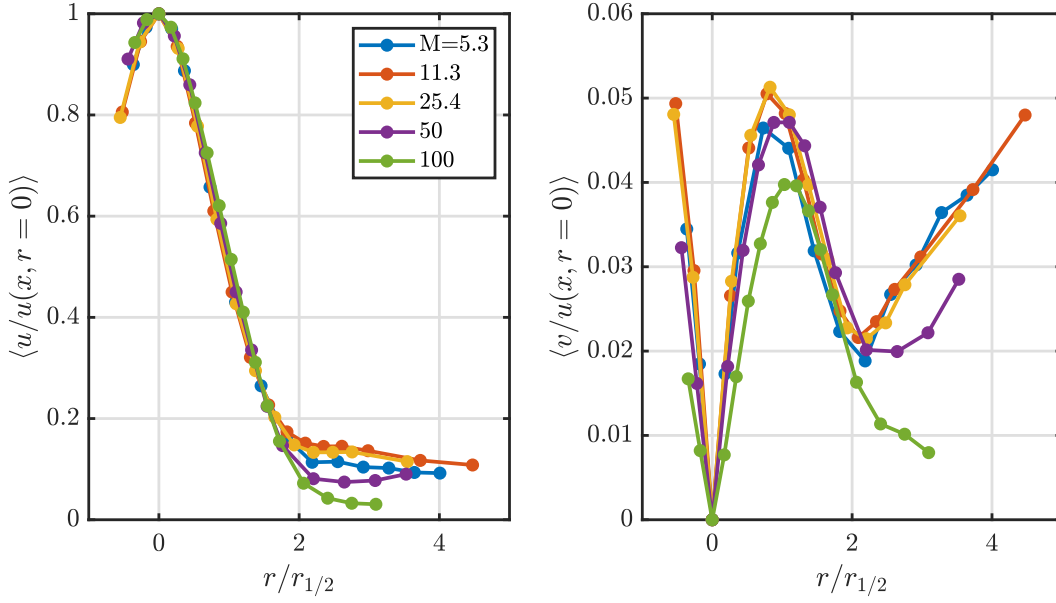
Figure 4.2:   Average axial velocity divided by the centerline axial velocity for measurements taken $10d_g$ downstream of the nozzle (left). Average radial velocity divided by the centerline axial velocity (right).

figure 4.2, the average axial and radial velocities are radially symmetric and can be approximated by a self-similar profile, especially for radial distances less than about two times $r_{1/2}$. For larger radial distances, larger particles driven by inertia contribute more to the mean velocities, thus yielding larger velocities than what would be observed for tracers.

As shown in figure 4.3, both the axial and radial average velocities are affected by the electrostatic actuation. The effect on the axial velocity is most readily noticeable at low momentum ratios. For instance, we observed an increase of around 22% of the centerline axial velocity at 60 kV. Nonetheless, significant increases in the radial velocities were observed across all momentum ratios. As shown in figure 4.3, the increases in both radial and axial velocities were most apparent far from the center of the spray. It is worth noting that, at a sufficient distance away from the centerline, the radial velocities have an approximately linear gradient and that this gradient increases with increasing applied voltage. On the

other hand, the axial velocities away from the centerline did not show such strong trends, but rather they were simply shifted toward higher values.

We illustrate the impact of the electric field on the average velocities across all experimental conditions explored in figures 4.4 and 4.4. We can see that at the centerline the increase in the axial velocity is small relative to the velocity in the absence of an electric field. However, the radial velocity can differ noticeably in the presence of an electric field. Close to the centerline the radial velocity seems to increase monotonically as a function of applied voltage. In contrast the behavior at a distance of $3r_{1/2}$ from the center is nonmonotonic with increasing applied voltage. Notably for an applied voltage of 15 kV we observed a reduction in both the axial and radial velocities.

In terms of the relative change in velocity (i.e. velocity in the presence of electric divided by velocity in the absence of electric field), we can see that the most notable feature is the increase in the radial velocity, especially away from the center of the spray. Near the center of the spray (at $r_{1/2}$) the average radial velocity under an electric field was observed to be up to twice the velocity absent an applied voltage. More strikingly, near the edge of the uncharged spray (at $3r_{1/2}$) the average radial velocity was observed to be up to almost an order of magnitude larger, due to the strongest applied electric field.

In addition of characterizing the mean velocities across all particles, we computed the two components of the velocities for a subset of the droplets that satisfied coincidence criteria from the measurements of the green and blue lasers. As shown in figure 4.6, closer to the nozzle and to the center, smaller droplets have faster axial velocities than larger droplets. However, moving away from this location where the largest axial velocity is recorded, the larger droplets have larger axial velocities than the smaller droplets. In contrast, large droplets only have larger radial velocities for the location closest to the nozzle, and the difference between the radial velocities for small and large droplets increases with radial position.
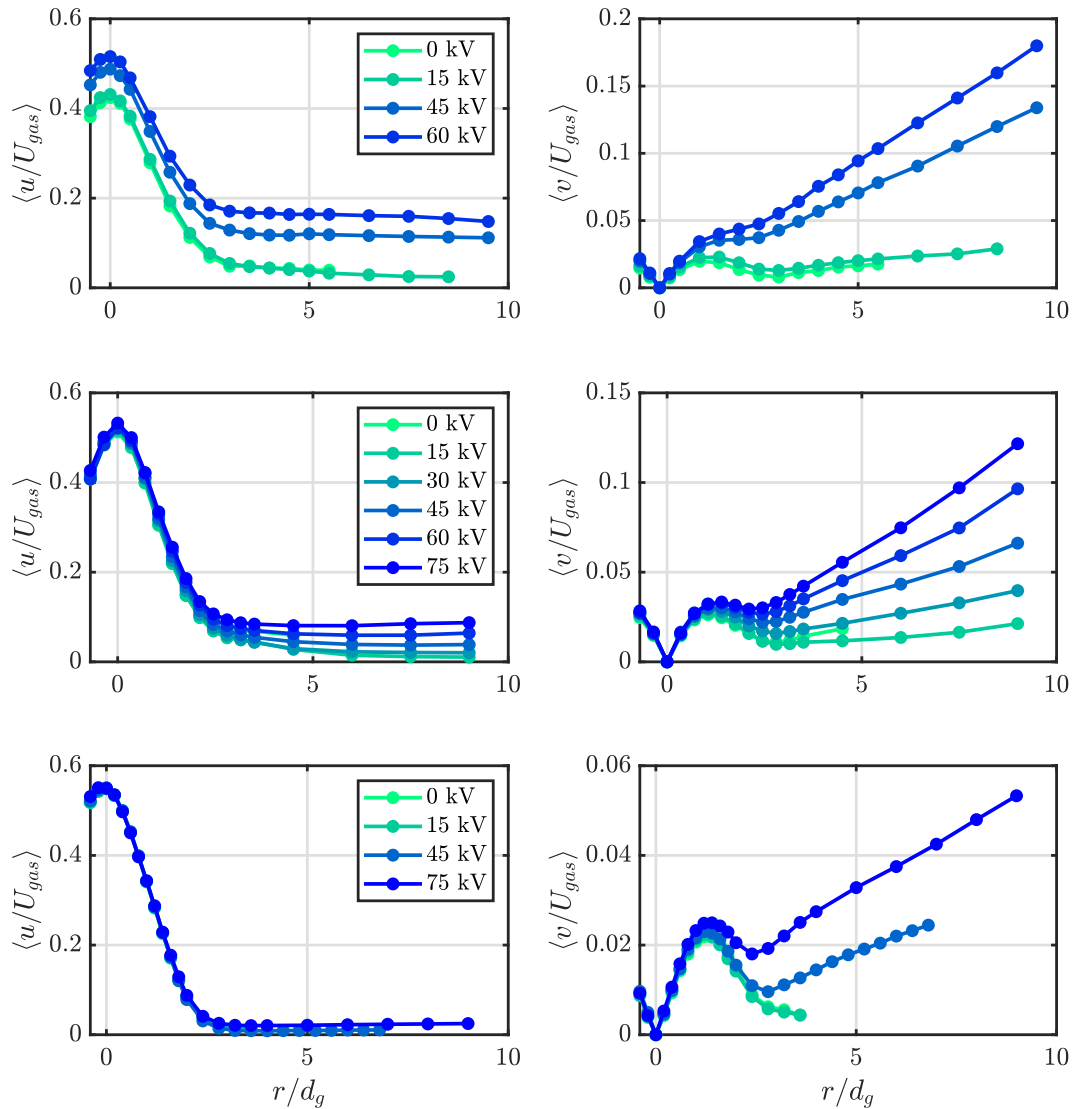
Figure 4.3:   Average axial (left) and radial (right) velocity profiles measured $10d_g$ downstream of the nozzle and normalized by the mean exit gas velocity at the nozzle for momentum ratios of 5, 25 and 100.
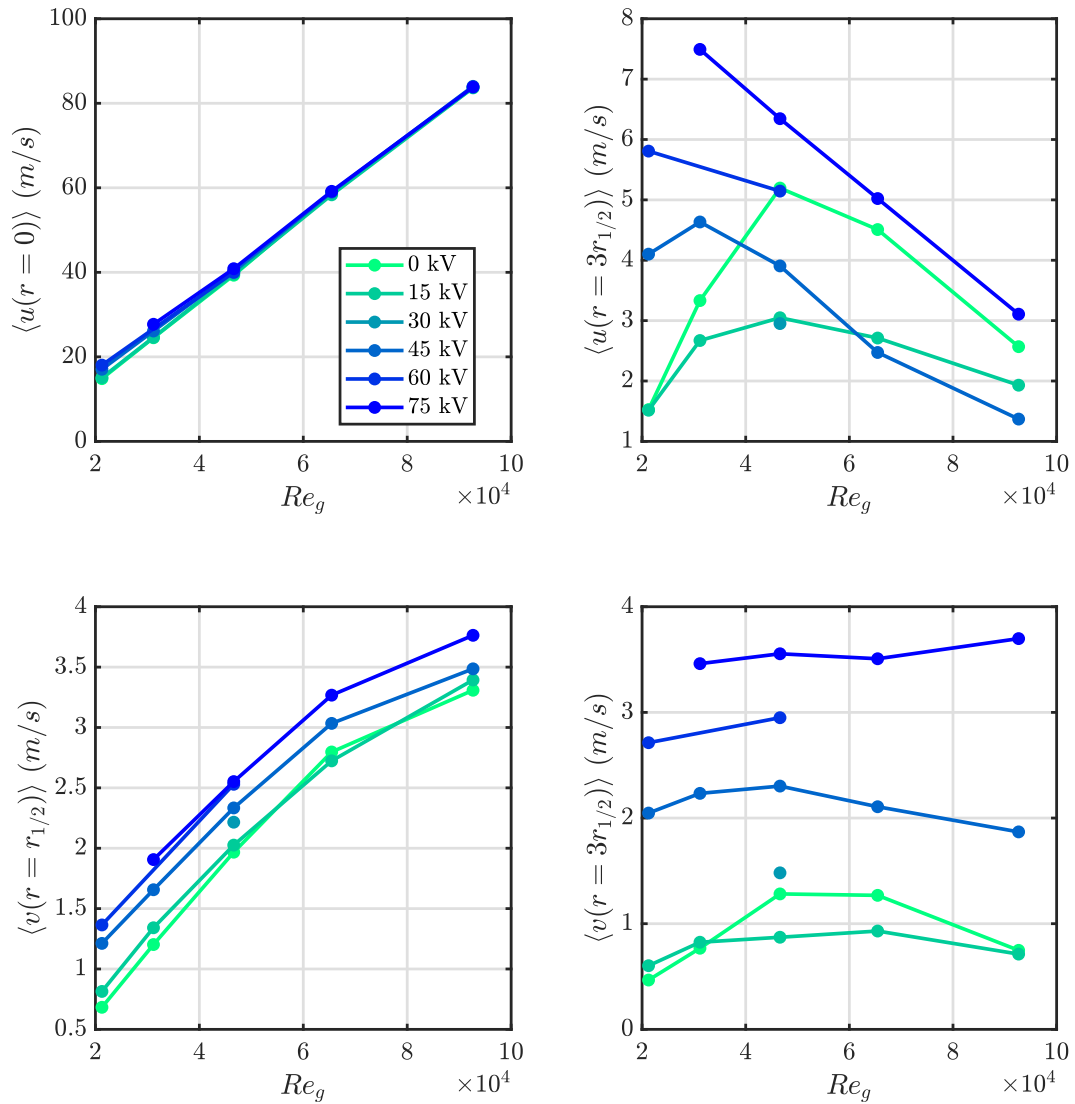
Figure 4.4: Axial and radial velocities as a function of gas Reynolds number. Centerline axial velocity (top left), axial velocity at $3r_{1/2}$ (top right), radial velocity at $r_{1/2}$ (bottom left) and at $3r_{1/2}$ (bottom right). The $r_{1/2}$ is computed from the mean axial velocity without any applied electric field.
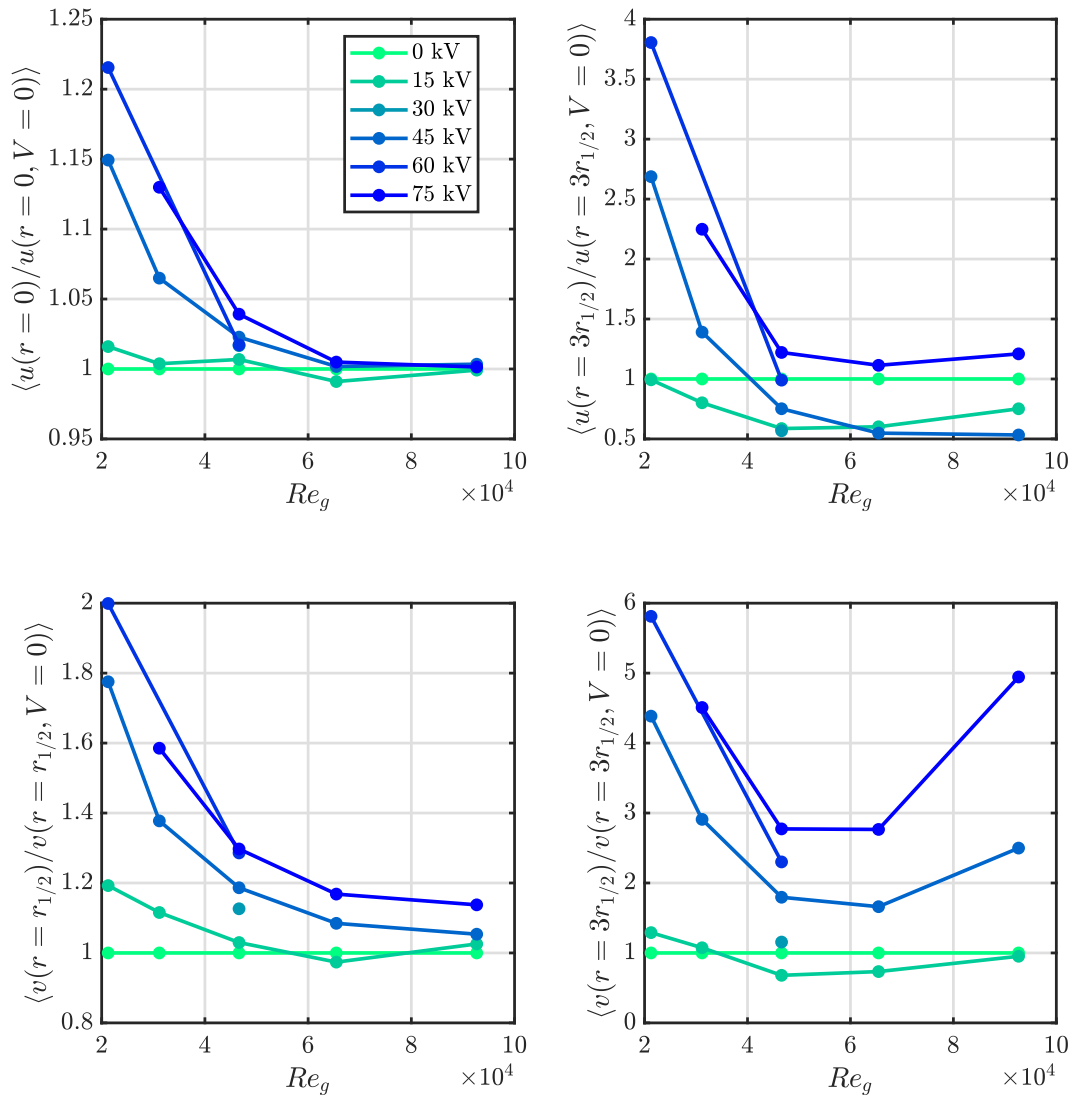
Figure 4.5: Same quantities as depicted in figure 4.4, divided by the corresponding quantity at 0 volts to illustrate the fractional change.
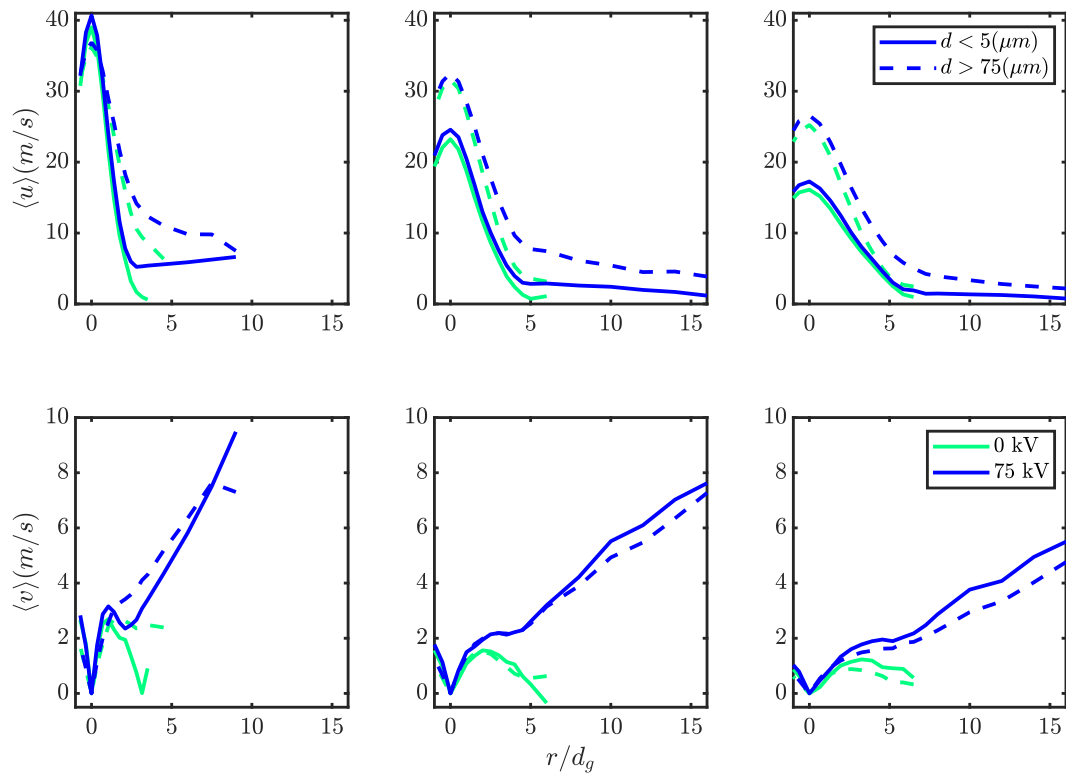
Figure 4.6: Velocities without applied voltage and at 75 kV at a momentum ratio of 25 computed for particles with diameter less than 5 microns (solid) and more that 75 microns (dashed). The axial (top) and radial (bottom) velocity profiles are shown for three downstream locations: $10d_g$ (left), $18.5d_g$ (center) and $27d_g$ (right).

4.3   Diameter Measurements

4.3.1   Mean Diameter Radial Profiles

Diameter measurements revealed significant reductions in droplet sizes associated with the presence of electric charge and an external field, across the range of conditions studied. The mean diameter profiles in the presence of an electric field differed significantly from the profiles without external field. In the absence of an electric field, the arithmetic mean diameter tends to increase monotonically with radial position, yielding a concave profile (upwards) for the mean diameter as a function of radial position (as shown in figure 4.7). In contrast, the mean diameter profiles under an applied electric field display non-monotonic behavior, with a maximum that decreases with increasing electric field strength. Moreover, the volumetric liquid flux distribution across the spray becomes more evenly distributed radially with increasing electric field strength.

The impacts of the electric field actuation are more apparent at lower momentum ratios, as shown in figure 4.8, as was the case for the velocity fields. One important caveat is that for the lowest momentum ratios (M=5 and 11) the higher order statistics (i. e. d_{32}, d_{43} and volumetric flux) are not fully converged, as they include important contributions from very scarce large droplets (> 150 microns) that are not always captured by the PDI measurements. This may result in non-trivial changes in the measured droplet population that are due to more volume being captured as big droplets are broken up into smaller droplets when an electric field is applied. This could explain, for instance, the unexpected increase of d_{32} found for small radial distances for $M = 5$ when the electric field is applied.

4.3.2   Droplet Diameter Statistics in a Cross Section of the Spray

In order to compute representative statistics for the droplet population across the whole spray, we used Equation 4.4 to combine the pointwise measurements at different radial locations. This procedure yields probability distributions, such as the ones shown in figure 4.9, that represent the droplet population across a plane perpendicular to the spray axis. We
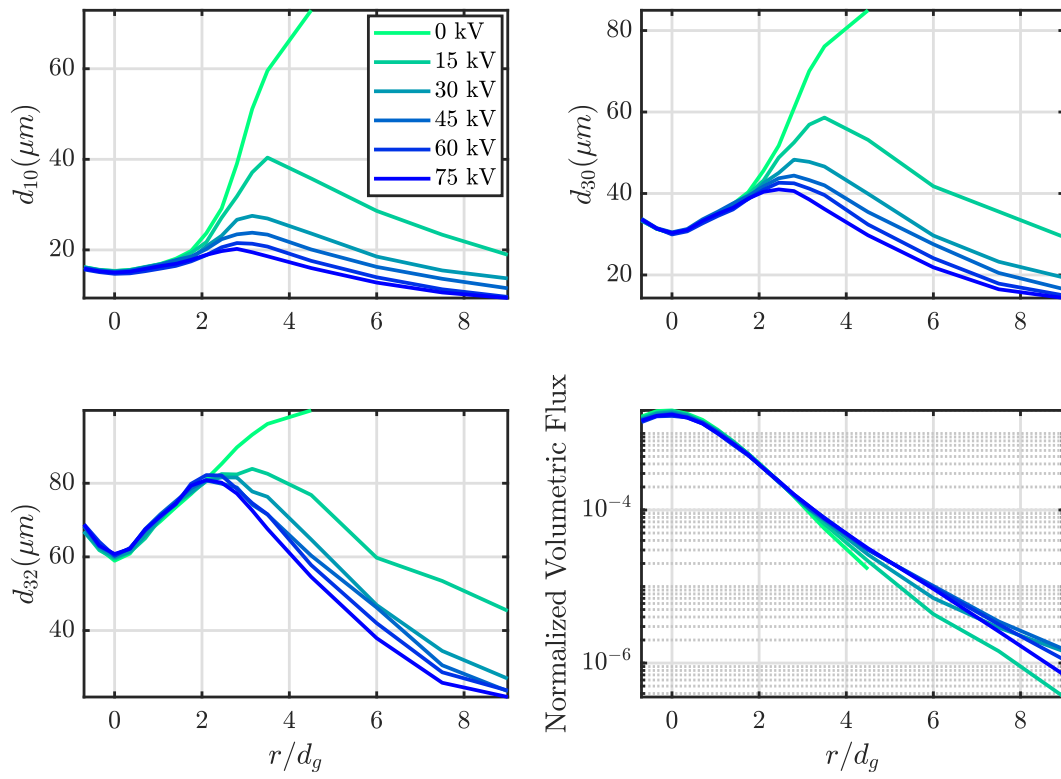
Figure 4.7: Profiles of mean diameters and normalized volumetric flux for a momentum ratio of 25 at different applied voltages.
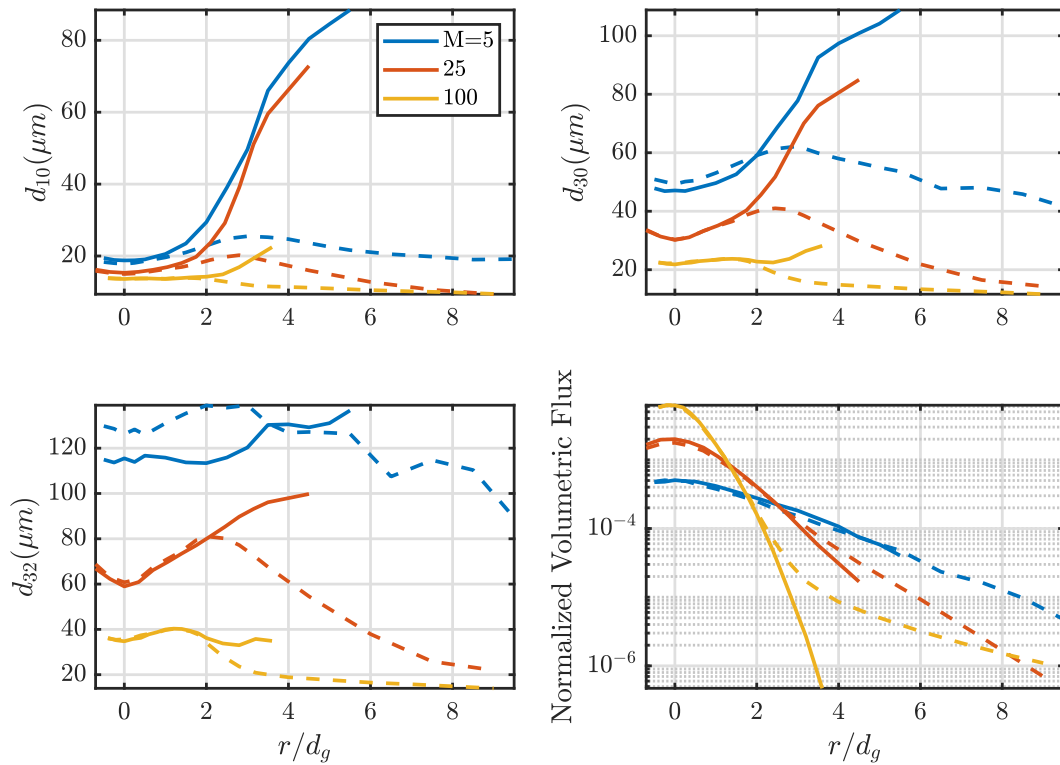
Figure 4.8: Profiles of mean diameters and normalized volumetric flux for three momentum ratios, with no electric field (solid) and with applied voltages (dash) of 60 kV at M=5 and 75kV at M=25,100.
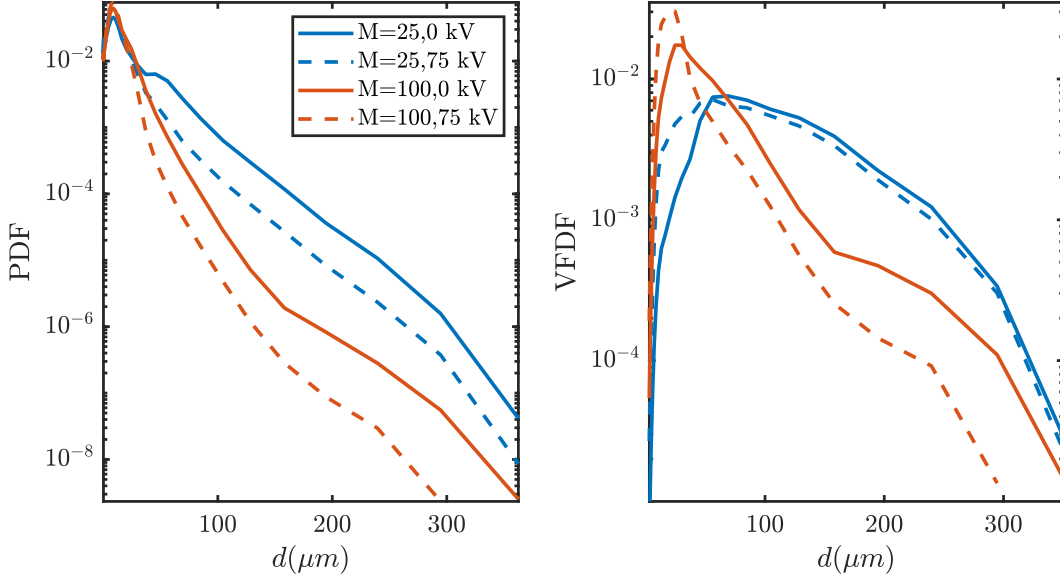
Figure 4.9: Probability distribution function (left) and volume flux density function (right) computed from a cross section of the spray.

observe a significant reduction in the relative occurrence of larger drops due to the electrostatic forcing, even at the highest momentum ratios. In addition to the Probability Density Function (PDF), we can compute a Volume Flux Density Function (VFDF), according to equation 4.7 below, that illustrates the relative contribution of each particle size class to the total liquid volume flux. As in the case of the PDF, we see that electrostatic forcing shifts the VFDF so that smaller droplets contribute a larger portion of the total spray liquid volume.

$$g_i = \frac{1}{\Delta d_i} \frac{p_i d_i^3}{\sum_j p_j d_j^3} \tag{4.7}$$

We summarize the results for the mean diameters characterizing the droplet distribution across all the experimental conditions explored, in figures 4.10 and 4.11. For d_{10}, d_{20} and d_{30}, we see decreases that are approximately linear with applied voltage. Interestingly, the relative changes in the values of these mean diameters are of a similar magnitude across all momentum ratios, with decreases of up to 40% relative to the unelectrified conditions.

Moreover, the reductions in the mean diameters due to the electrostatic forcing are of a similar magnitude than those achieved by significantly increasing the momentum ratio. This means that for instance, the mean diameters for M=25 under electric field become of the same order of magnitude that for the unelectrified M=100.

An exception to the trend discussed above was observed for the Sauter mean diameter (d_{32}) and the volume-flux-weighted mean diameter (d_{43}), in the two lowest momentum ratios ($M = 5, 11$). For these two momentum ratios, the tails of the distribution are not well converged by the PDPA measurements (due to the weight of very large drops over 200 $/mum$) and can lead to significant uncertainty in estimating the higher order statistics of the distribution. Moreover, the problem can be further aggravated by the breakup of drops that would fall outside the measurement range in the unelectrified case. These very large drops could break up due to electrostatic effects and generate smaller droplets (although still large ($O(100\mu m)$) when compared to the smallest droplets in the distribution), thus generating an apparent increase in the frequency of large droplets due to the applied voltage. Nonetheless, for momentum ratios above 25, the expected linear decreases in d_{32} and d_{43} were observed as a function of applied voltage.

4.3.3 Volume Fraction Measurements

We computed estimates of the volume fraction, ϕ, at each measurement location based on the probe volume defined in equation 4.2 and the residence time of the droplets in this probe volume:

$$\phi = \frac{\pi}{6} \frac{1}{T_s} \sum_i \frac{t_i d_i^3}{V_i}, \tag{4.8}$$

where the summation is done over all particles, V_i is the diameter dependent probe volume, T_s is the total sampling time at a given measurement location and t_i is the residence time in the probe volume as given by the PDPA gate time. To be more precise, this estimates the time averaged volume fraction for each measurement location. Figure 4.12 shows the
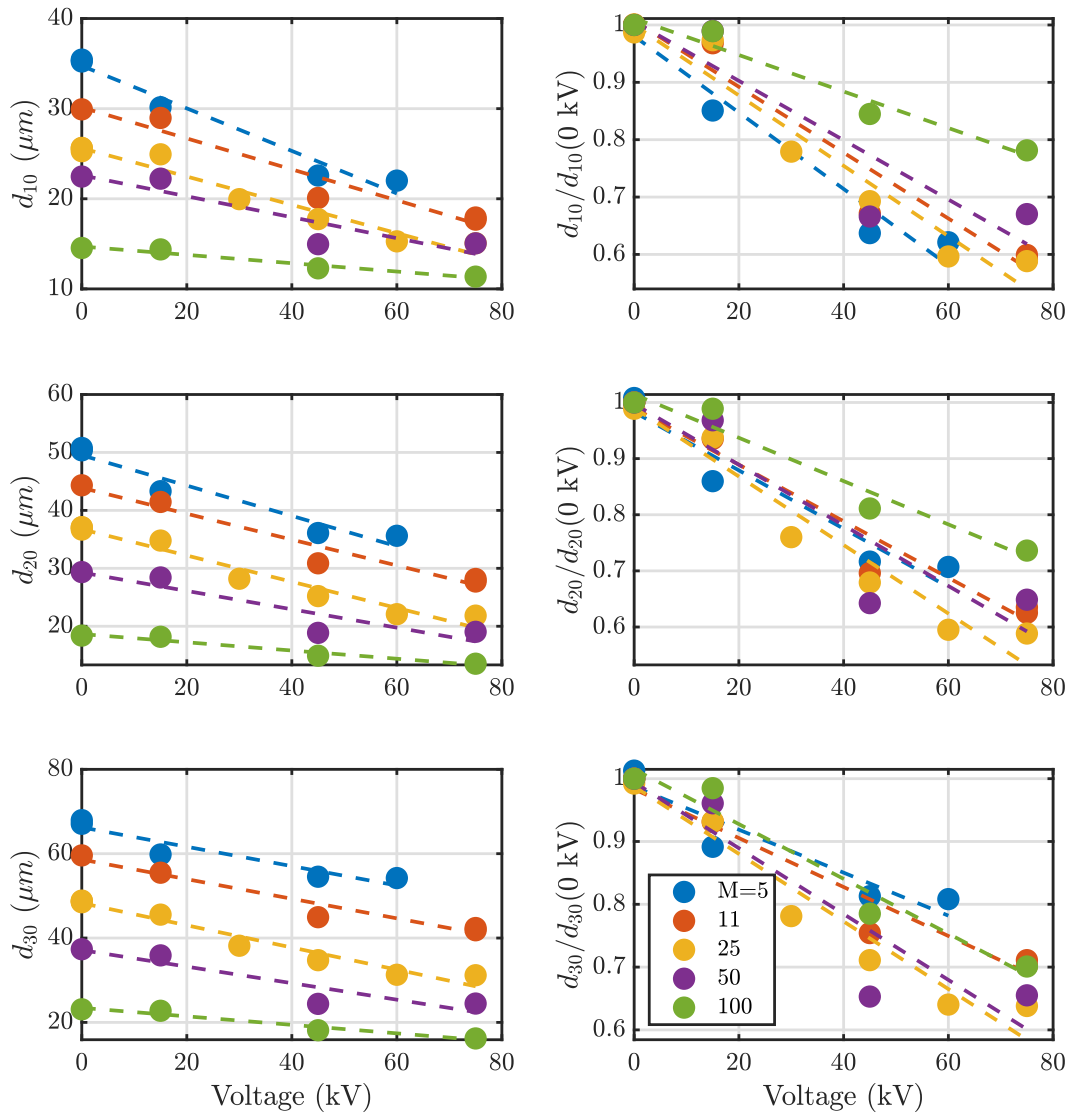
Figure 4.10: Mean diameters as a function of applied voltage for five momentum ratios. The mean diameters in microns (left) and normalized by the corresponding values at zero voltage to illustrate fractional changes (right). Dashed line show linear fits to illustrate the trends observed for increasing electrify field strength.
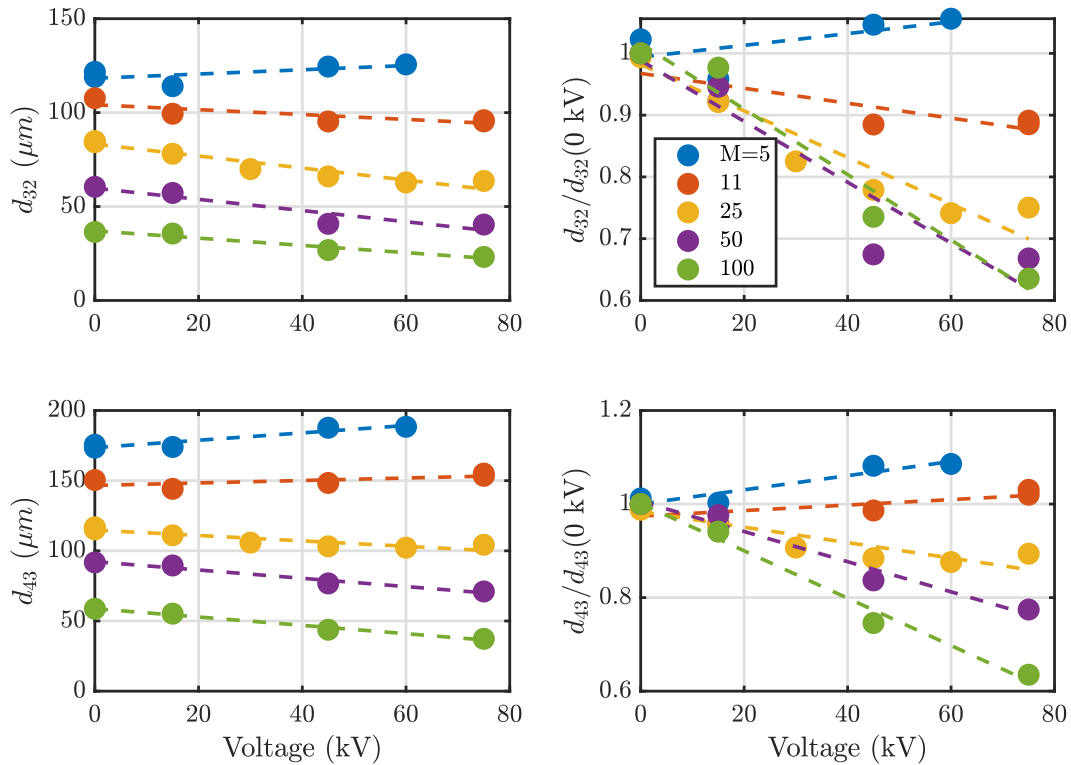
Figure 4.11: Mean diameters as a function of applied voltage for five momentum ratios. The mean diameters (left) and normalized by the corresponding values at zero voltage to illustrate fractional changes (right). Dashed line show linear fits to illustrate the trends observed for increasing electrify field strength. The observed trends at M=5,11 are suspected to come from an experimental bias of the PDI in determining the large drop size found at these momentum ratio in the absence of an electric field.

volume fraction for a momentum ratio of 25 at different voltages and at three downstream locations. Electrostatic forces generate volume fraction profiles that are broader and more uniform, with smaller concentrations in the centerline and higher concentrations away from it. Moreover, these differences become more apparent with increasing axial distance downstream from the nozzle.
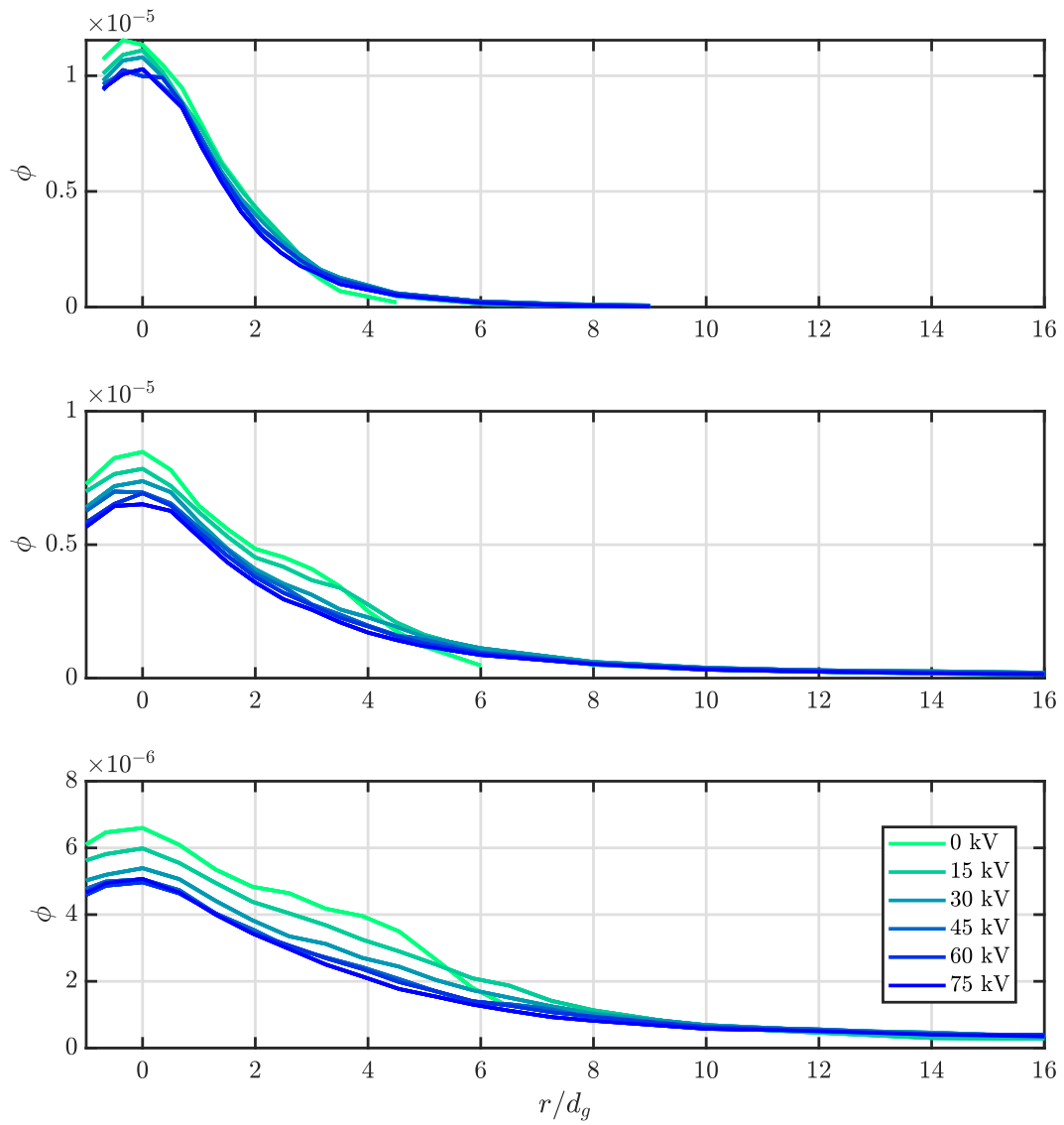
Figure 4.12: Volume fraction as a function of radial position for M=25 and at three downstream locations: $10d_g, 18.5d_g$ and $27d_g$ (from top to bottom).

4.4   Discussion

The results presented here clearly demonstrate that applying an electric field to a coaxial spray results in smaller droplet sizes and charged droplets that experience radial acceleration. Moreover, these two effects compound to produce more uniform profiles of mean diameters as well as liquid volume flux. In addition to the overall decrease in droplet size, there appears to be preferential radial transport of smaller droplets, as evidenced by the larger radial velocities experienced by small droplets at large enough distances from the nozzle.

The preferential transport of drops of a given size can be explained as the result of the competing effects of inertia, drag and electric forcing. As a first order conceptual approach, we can describe these competing effects by looking at the equation of motion for a rigid sphere experiencing quasi-steady drag (see for instance the derivation by Michaelides and Feng [42]) under a uniform electric field :

$$m\frac{d\mathbf{u}}{dt} = \frac{1}{2}\rho_g u_r^2 C_D A\hat{\mathbf{u}}_r + \mathbf{E} \tag{4.9}$$

$$\frac{d\mathbf{u}}{dt} = \frac{3\rho_g}{4\rho_l d}u_r^2 C_D\hat{\mathbf{u}}_r + \frac{\rho_c}{\rho_l}\mathbf{E} \tag{4.10}$$

where $\mathbf{u}$ is the droplet velocity, $\mathbf{u}_r = \mathbf{U} - \mathbf{u}$, is the droplet's velocity relative to the gas velocity $\mathbf{U}$, ρ_c is the volume charge density, E is the electric field and C_D is the drag coefficient. The key quantity to be estimated here is the volumetric charge density of the drop. Although the data presented here cannot give a direct estimate of this quantity, we can test whether certain scaling laws found in the literature hold. In particular, it has been observed that, for pure electrosprays, the charge per unit volume scales similarly to the Rayleigh limit[21], that is $\rho_c \propto d^{-3/2}$. Indeed, if the charge densities do not scale as the Rayleigh limit but rather follow a power law with a different exponent, say n, then for $n < -3/2$ sufficiently small droplets would exceed the limit and, for $n > -3/2$, sufficiently large droplets would exceed this limit. Of course, this does not preclude the possibility that the charge density exhibits a much more complex relationship with drop size.

Assuming the $\rho_c \propto d^{-3/2}$ scaling law holds, we can compare the magnitude of drag to electrostatic forces as a function of size. For the sizes and velocities explored in the present study, we can safely say that the droplet Reynolds number remains well under 1000 so that we can use an approximation to the drag coefficient as proposed by Putnam [50]:

$$C_D = \frac{24}{Re_d} \left(1 + \frac{1}{6} Re^{2/3} \right) \tag{4.11}$$

So that in the low Re limit, when $C_D \approx 24/Re_d$, we can see that the terminal velocity scales as $u_t \propto d^{0.5}$. On the other hand, for the high Re limit, when $C_D \approx 4/(Re_d^{1/3})$, we can see that the terminal velocity scales as $u_t \propto d^{-0.25}$. This implies that there is a maximum terminal velocity at some finite size of diameter, and that this maximum occurs at smaller diameters with increasing electrostatic force (increased charge and increased electric field strength). As the applied voltage is increased, both the charge and electric field strength increase, thus biasing the electrostatic transport in favor of smaller droplets. Additionally, the role of inertia implies that smaller droplets, that slow down faster as they move away from the center of the jet will have more time to be displaced to the edge of the spray due to electrostatic forces.

A finite difference simulation of droplet trajectories, using the dynamics in equation 4.10, was used to test the different velocity profiles generated by different electric charge density power laws. We started by generating a random sample of droplets taken from a lognormal distribution that approaches the distributions observed in our experimental data. Then, solutions to equation 4.10 were computed by using a self-similar jet flow for the gas velocities as well as approximations to the electric field obtained from the finite element simulations. The results in figure 4.13 show the different profiles for different values of the scaling law $\rho_c = q_0 d^{-n}$, where the coefficient q_0 is chosen so that the bulk charge density matches the experimentally measured charge density. We see that if the charge density does not decay fast enough with diameter, e.g. n=1, the profile of the mean diameter is monotonically increasing. The simulations with n=1.5 are in good qualitative agreement with experimental results and the simulated velocities are in good quantitative agreement with the experimental

results. For a parameter value n=2, the simulated velocities are significantly larger than the observed ones and the mean diameters decay too quickly with radial distance. This extremely simplified model captures key characteristic of the electrostatic transport of droplets.

In addition to offering insight into the transport of droplets due to electrostatic forcing, the hypothesis of the power law for the electric charge density offers a potential mechanism for the reduction in droplet sizes in electrified spray. Indeed, the presence of charge can disrupt drops and produce secondary breakup below the Rayleigh limit due to the compounded effect of the destabilizing electrical and hydrodynamic forces. Breakup of charged dielectric droplets in sprays below the Rayleigh limit has been reported in the literature[60]. Nonetheless, the present work cannot differentiate between the impact of electrostatic forcing on primary and secondary atomization and the relative importance of each in reducing droplet size. However, it is clear that the reported effects of the applied electric field go well beyond modification of the transport of droplets and that high electric fields result in smaller droplets across the spray over a large range of atomization conditions.
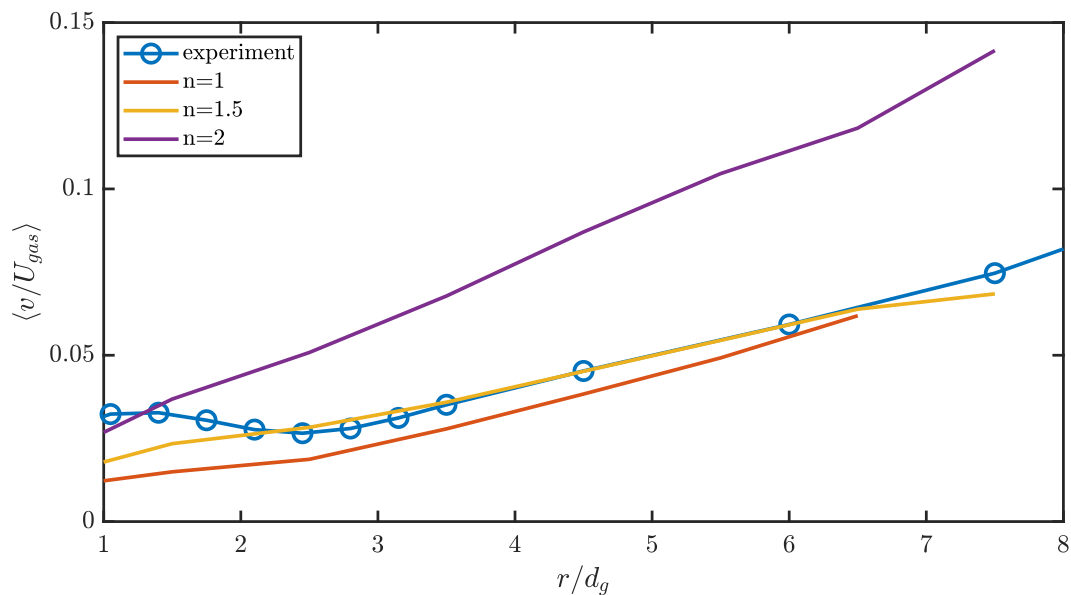
Figure 4.13: Finite difference simulation results for the mean radial velocity based on flow conditions at M=25 and 60kV.

4.5 Conclusions

An experimental study of electrostatically assisted coaxial atomization under a broad range of conditions revealed that strong electric fields can significantly reduce the droplet sizes even at high values of the momentum ratio. The resulting charged drops also experience accelerations due to electric forces, with the most prominent effect being that of radial transport. The combination of smaller droplets and preferential radial transport of small droplets results in flatter profiles of the mean diameters as well as in more uniform profiles of liquid volume flux. The observed results were consistent with the electric charge density following a power law with a $n = -1.5$ exponent, as predicted by the Rayleigh limit criterion for stability of charged dielectric drops. Detailed simulations could yield more insights into the relative importance of primary and secondary atomization modification by electric fields and could help better constrain the electric charge distribution of the droplet population. These results show that electrostatic forcing can be used as a robust form of forcing for the

multiphysics control of sprays.

Chapter 5

ELECTROSTATIC FORCING ON SWIRLING COAXIAL ATOMIZATION

This thesis has already discussed how electrostatic forcing can reduce the droplet sizes in conventional electrostatic atomization and accelerate the droplets leading to enhanced radial transport. In this chapter, the thesis considers the case of swirl in the co-flowing gas jet and its effect on the spray formation and development. It has been reported that addition of swirl to the gas jet of a coaxial atomizer can enhance the breakup of the liquid jet, increase the spreading rate and decrease the droplet diameters in the centerline of the spray [26, 32]. In what follows, only swirling coaxial sprays with swirl ratios above a critical threshold are considered. As described by Lasheras and Hopfinger [26], this critical threshold can be estimated in the range $1 < M < 1000$ by the following empirically derived expression:

$$S_{cr} = [2M \ln(d_g/d_l)]^{-1/2} (1 + M/6)^{1/2} \qquad (5.1)$$

According to the expression above, the critical swirl ratio for a momentum ratio of five is about 0.34, whereas for a momentum ratio of 11, it would be about 0.28. The expression above yields an asymptotic value for the critical swirl ratio of about 0.23 as the momentum ratio increases. In this chapter, we present results for three swirl ratios (SR): 0, 0.5 and 0.75 (where at least one is supercritical for any Momentum Ratio), for the same momentum ratios and voltages as the ones explored in the previous chapters.
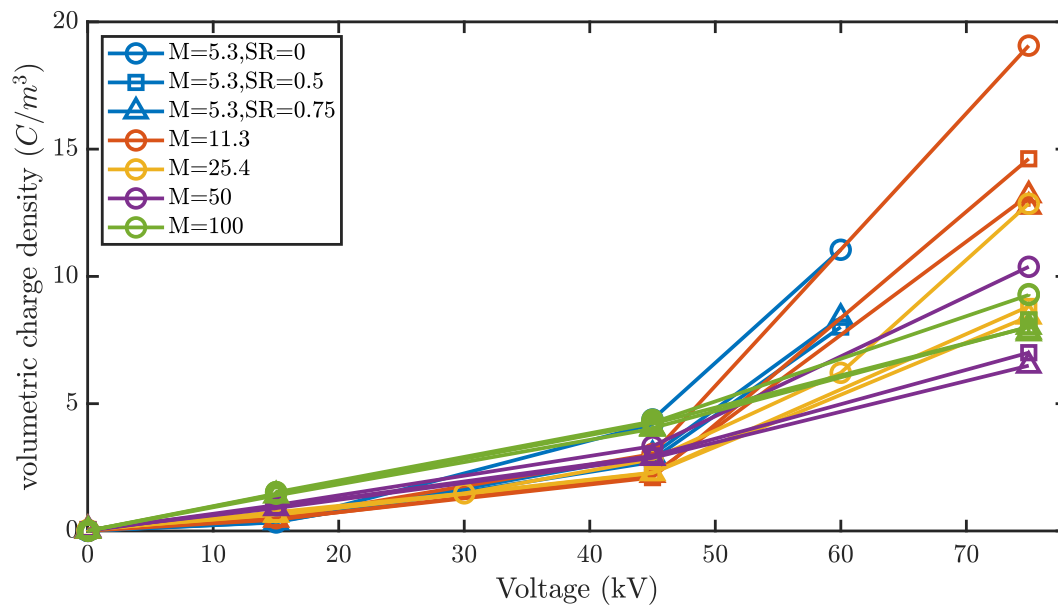
Figure 5.1: Volumetric charge density as a function of applied voltage for all the momentum and swirl ratios studied.

5.1 Results

5.1.1 Electric Charge Density

Addition of swirl was not observed to significantly change the electric charge density dependence on applied voltage. The same pattern observed in the previously presented results, with no gas swirl, holds. The only difference is that addition of swirl appears to reduce the charge density slightly at high voltages, as shown in figure 5.1. At high voltages, increasing either swirl or momentum ratio results in a reduction of the liquid electric charge density.

5.1.2 Mean Velocities

As we can see in figure 5.2, addition of swirl to the gas flow does not change the self-similar nature of the mean radial profiles of the axial velocity. It does, however, impact the spreading rate as described by the $r_{1/2}$ value, and it increases the relative magnitude of the

mean radial velocity. It is worth noting, however, that for a given momentum ratio, a higher swirl ratio results in lower radial velocities (at a given downstream position). We observed a substantial increase in the $r_{1/2}$ value due to swirl, with values for $SR = 0.75$ being twice the values without swirl, for all momentum ratios.

The modification of the mean velocity due to electrostatic forcing, for the swirling flow cases, were largely the same as in the absence of swirl. Small relative increases in the axial velocity can be observed, with the largest increases being away from the spray centerline. The ensuing reduction in axial velocity that accompanies an increase in swirl ratio at a fixed momentum ratio implies that the axial electrostatic acceleration is more prominent at high swirl ratios. On the other hand, increasing swirl ratio was not observed to substantially increase the radial velocity, as shown in figure 5.3. Note that the measurements extend to larger radial positions in the presence of swirl, as more droplets are found near the edge of the spray compared to the no-swirl cases, allowing converged measurements there. This will be further evident when droplet fluxes are discussed in the next section.

As can be appreciated in figure 5.3, the radial velocity profiles at the edges of the spray are approximately linear, with the slope increasing as a function of applied voltage. We computed the radial velocity gradients with a linear fit to the mean radial velocities at the edge of the spray. Figure 5.4 shows the values for the slope, for which the linear fit had an R^2 value greater than 0.9, along with the 95% confidence interval bounds. We can see that the gradient increases monotonically with the applied voltage and has only a small dependence on the momentum ratio (figure 5.4, left). Similarly, the radial derivative of the radial velocity does not depend strongly on the swirl ratio, except for the largest momentum ratios (figure 5.4, right). For the two highest momentum ratios, an increase in swirl resulted in smaller mean velocity gradients. This was accompanied by an increase in the mean diameters at the edges of the spray for the highest momentum ratios.

The electrostatic effect on the mean axial velocities near the centerline is similar for all measured swirl ratios. As seen in figure 5.5 (top left), near the spray centerline the aerodynamic forces appear to dominate and there is only a very moderate increment in
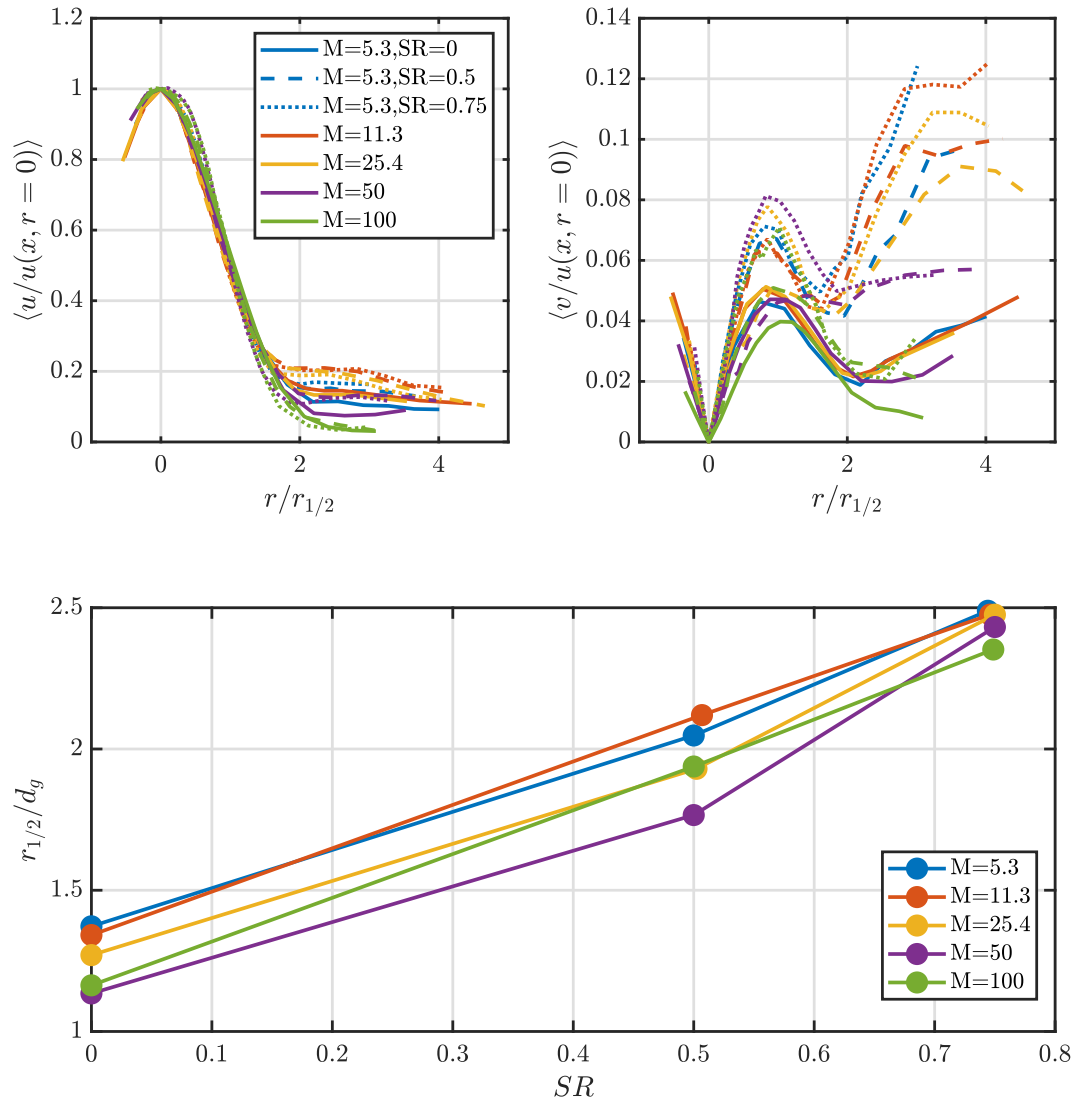
Figure 5.2: Mean axial and radial velocities for all momentum and swirl ratios with no electric field (top left and right, respectively); $r_{1/2}$ as a function of swirl ratio (bottom).
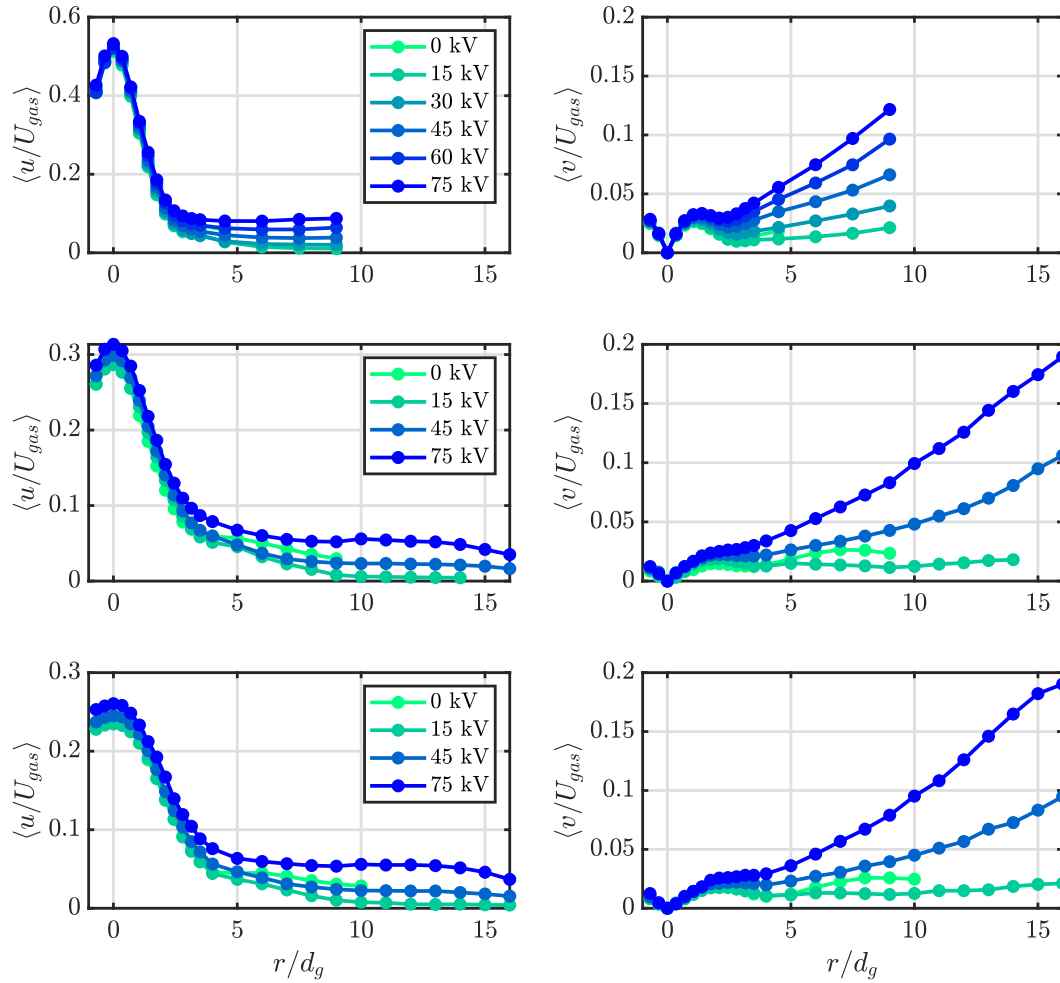
Figure 5.3: Axial (left) and radial (right) mean velocities at a momentum ratio of 25 for swirl ratio 0 (top), 0.5 (middle) and 0.75 (bottom) at several applied voltages.
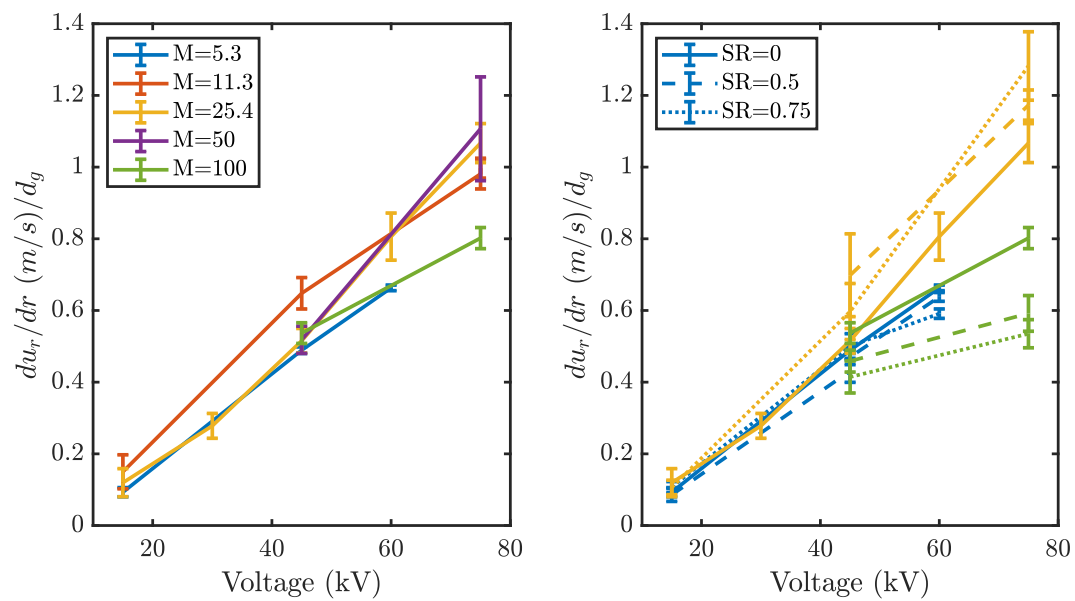
Figure 5.4: Radial gradients of radial velocity for SR=0 (left) and for three swirl ratios and three momentum ratios, 5, 25 and 100 (right). The error bars depict the 95% confidence interval for the estimates of the gradient.

mean axial velocities even for the highest electric field strength. The mean axial velocities away from the centerline (figure 5.5 top right) display concave down profiles at all momentum and swirl ratios for zero applied voltage. Interestingly, at low M ($M \leq 25$), the axial velocity away from the centerline increases due to the electrostatic forcing for all swirl ratios, whereas for high M ($M \geq 50$), it decreases for swirl ratio greater than 0.5. In contrast, the radial velocities are seen to increase with applied voltage at all locations and swirl ratios (figure 5.5 bottom). Far from the center of the spray, however, the mean radial velocity in the absence of swirl is fairly constant with momentum ratio (figure 5.5, bottom right, for 75 kV). In contrast, adding swirl to the flow with increasing momentum ratio reduces the increase in radial velocity far from the centerline at high voltages (figure 5.5 bottom right).

The changes in the mean velocity profiles reported above, average the impact of the electric field over droplets of all sizes. However, both the axial and radial velocities are strongly dependent on the droplet size, as is shown in figure 5.6. Droplets larger than 75 μm displayed faster axial velocities than drops smaller than 5 μm in diameter, both with and without an electric field, except at the centerline for swirl ratios 0 and 0.75 and at the edge of the spray (figure 5.6 top). On the other hand, addition of swirl did significantly alter the differences in radial velocities across droplet size classes. For a swirl ratio of zero (figure 5.6, bottom left), the radial velocities of both droplet size classes follow a linear dependency, and remain close to each other. For swirl ratios of 0.5 and 0.75, however, large droplets have much higher radial velocities near the centerline, followed by a linear increase with a mild slope, whereas small droplets have slower radial velocities near the centerline followed by a steeper radial increase. As a result, the mean velocity profiles of these two droplet classes cross at a radial distance of $\approx 6d_g$ from the centerline.

5.1.3 *Mean Diameter Profiles and Normalized Liquid Volume Fluxes*

We considered in an earlier chapter the impact of electrostatic forcing on the mean diameters and fluxes for coaxial atomization without swirl. We now consider how the mean diameter profiles change due to combined swirl and electrostatic forcing. Results for momentum ratio
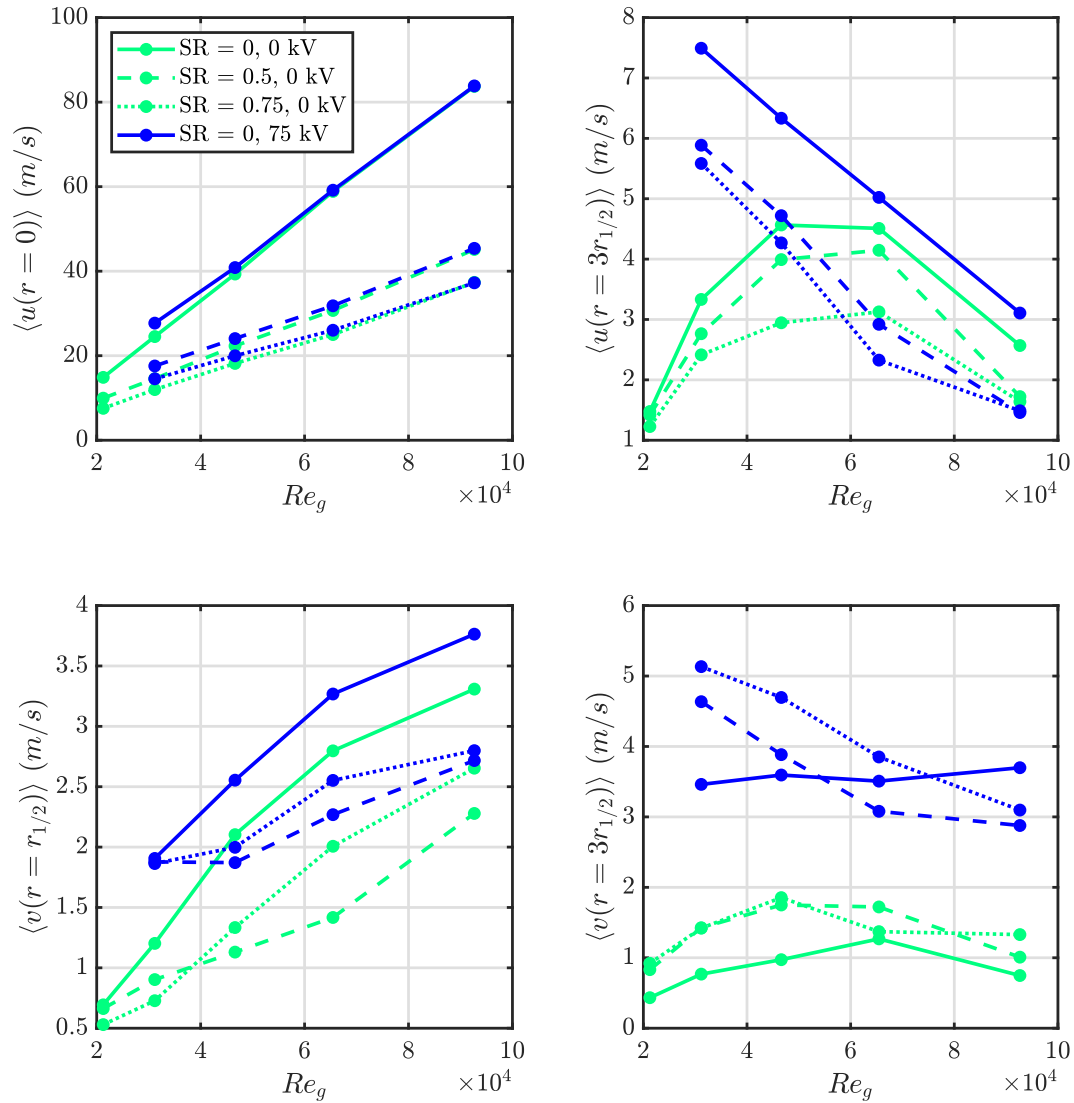
Figure 5.5: Mean velocities for three swirl ratios at 0 and 75 KV. Mean axial velocity in the centerline (top left) and near the spray edge at $3r_{1/2}$ (top right). Mean radial velocity near the centerline at $r_{1/2}$ (bottom left) and near the spray edge at $3r_{1/2}$ (bottom right).
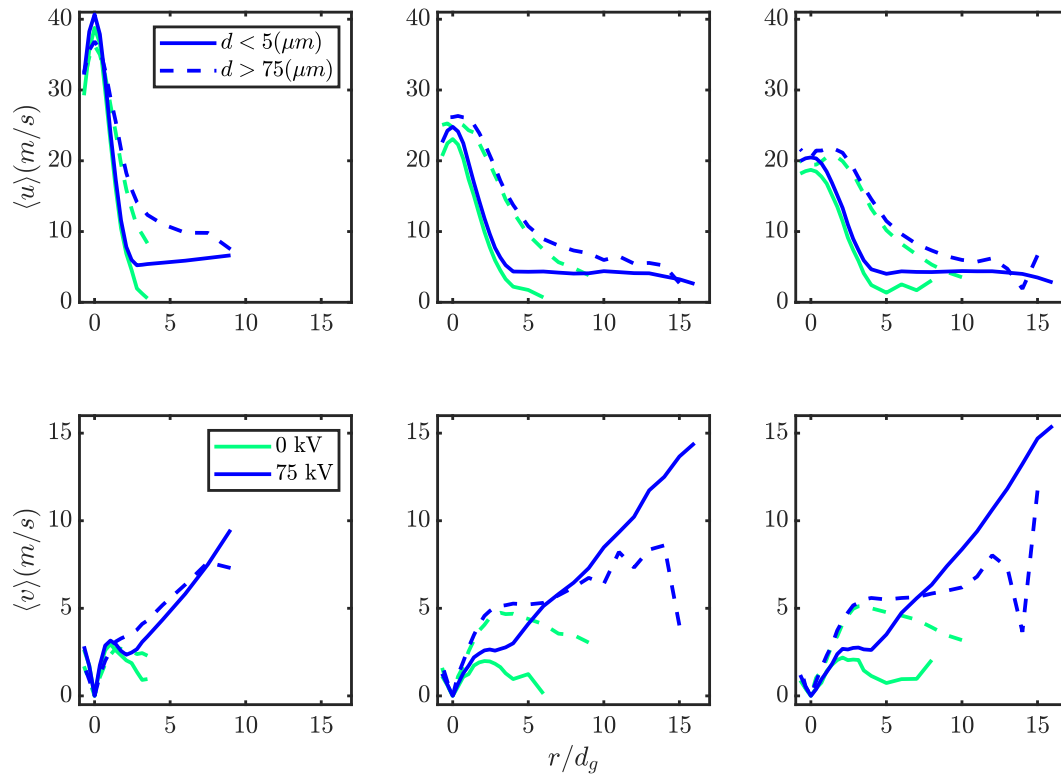
Figure 5.6: Mean axial (top) and radial (bottom) velocities M=25 for swirl ratios of 0 (left), 0.5 (middle) and 0.75 (right). The mean velocities are shown at 0 and 75 kV for two droplet classes: droplets less than 5 μm in solid lines and drops greater than 75 μm in dashed lines.

of 25, at three swirl ratios and for no applied voltage and at 75 kV are shown in figure 5.7. The arithmetic mean diameter (d_{10}, figure 5.7, top left) with the addition of swirl retains its concave shape but with much smaller mean diameters near the center of the spray and broader profiles, indicating the presence of large droplets much farther from the centerline than without swirl. The same decrease in d_{10} due to electrostatic forcing can be seen for a swirling gas flow. However, the onset of the negative gradient occurred farther downstream and was concomitant with a maximum of the mean diameter that was larger than in the absence of swirl. Similar trends were observed for the volume mean diameter (d_{30}, figure 5.7, top right) and the Sauter mean diameter (d_{32}, figure 5.7, bottom left), but the maxima of the volume mean diameter under electrostatic forcing was similar for all swirl ratio whereas, for the Sauter mean diameter, the maxima decrease with increasing swirl ratio. It is also worth noting that at the edges of the electrified spray, the mean diameters displayed minimum values that were very similar for all swirl ratios.

The normalized liquid volume flux (normalized so that the integral of the flux across the spray cross-section is unity), reveals stark differences due to the addition of swirl (figure 5.7, bottom right). As opposed to the highly concentrated flux that decreases monotonically away from the centerline observed in the non-swirling flow, addition of swirl results in flux profiles with non-monotonic dependence on the radial coordinate. These profiles display local minima in the center and maxima at radial positions $\approx 4d_g$. Thus, we can observe how addition of swirl spreads the liquid flow over a much broader cross-sectional area. In all cases, electrostatic forcing only changed the liquid volume flux at the edges, smoothing the decay of the flux, but without strongly affecting the flux for $r < 5r_{1/2}$.

Figure 5.8 shows the same quantities presented in figure 5.7, but for a momentum ratio of 100. Overall, the trends are similar but some of the effects of swirl are much more pronounced at this high M. First, notice that the arithmetic and volume mean diameters in the absence of an electric field show much larger values at the edges of the spray due to the addition of swirl (figure 5.8, top). Moreover, the values of these mean diameters for the electrified cases are larger at the edges in the presence of swirling gas flow. Moreover, in the absence of swirl,
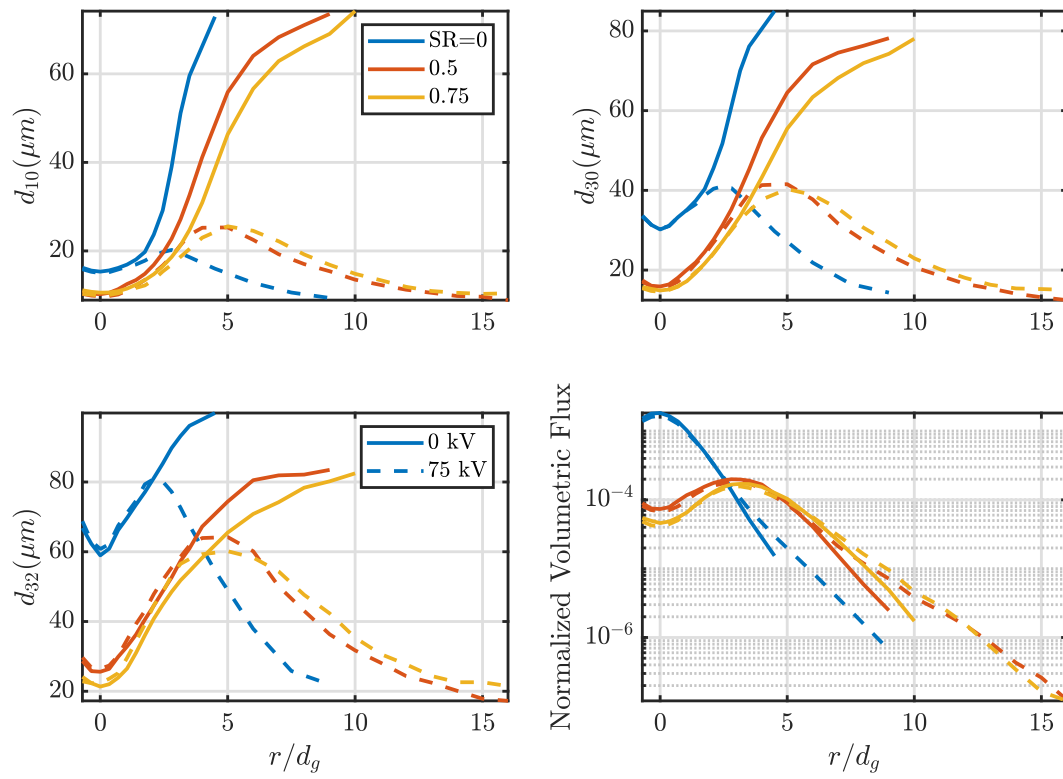
Figure 5.7: Profiles of mean diameters and normalized volumetric flux for M=25, three swirl ratios and at 0 and 75 kV.
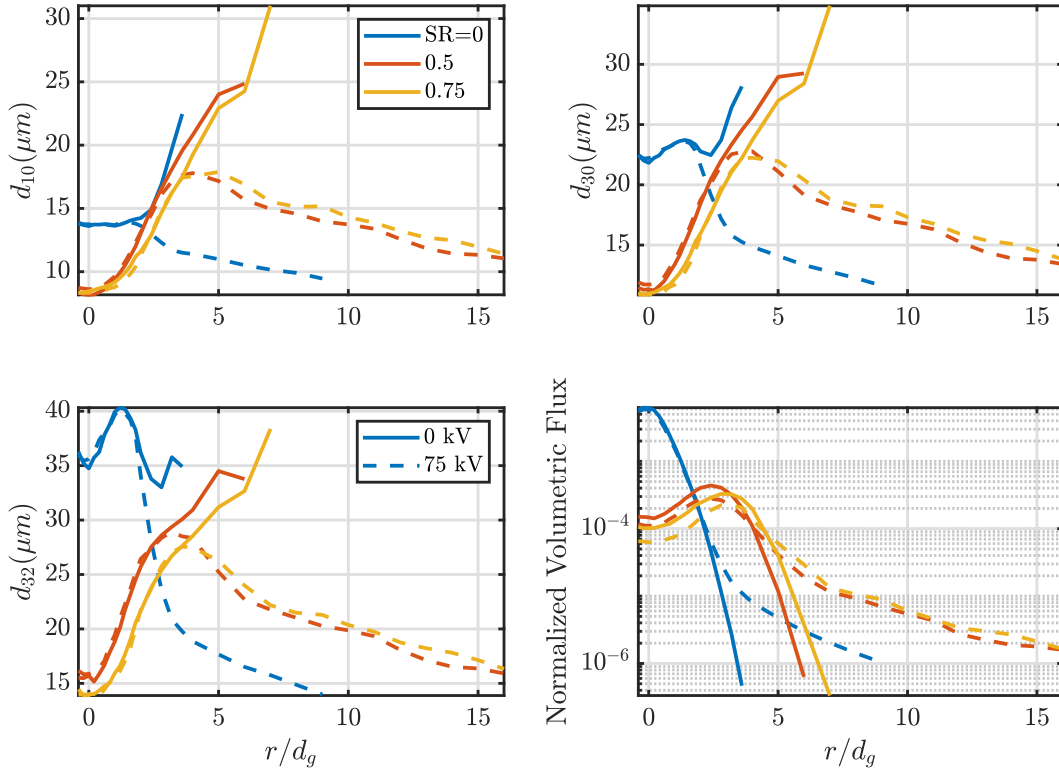
Figure 5.8: Profiles of mean diameters and normalized liquid volume flux for M=100, three swirl ratios and at 0 and 75 kV.

electrostatic forcing results in very sharp decreases in the volume and Sauter mean diameters away from the centerline, followed by more gentle decay after an inflection point. Finally, the liquid volume fluxes at this high momentum ratio have steeper radial dependencies, and electrification in this case is much more effective at redistributing the liquid flux across a wider area. The flux is indeed affected over the whole range of radial distances when electric forcing is added, unlike at lower momentum ratios.

5.1.4 Spray Statistics across Transverse Planes

We computed spray statistics across planes perpendicular to the spray longitudinal axis, as discussed in the previous chapter, in order to assess the impact of both swirl ratio and

electrification on the whole droplet population. An example of the resulting distributions for M=100 can be seen in figure 5.9, for two swirl ratios and two voltages. The distributions indicate that, at SR of 0.75, there is a substantially smaller contribution from the largest droplets (greater than 100 μm), as can be seen by the smaller tails of the PDF and the VFDF. Addition of swirl also appears to result in an increase in the number of "mid-sized" droplets (droplets with sizes in the order of tens of microns), as can be seen by the broader peak of the PDF for the SR=0.75 case. As before, electrostatic forcing reduces the number of the largest droplets, even in the presence of high swirl. It is important to point out the stark contrast between the two extreme cases at the highest momentum ratio of 100, that is between the case with no swirl and no electric field, and the case with both swirl and electric field, especially as it pertains to the VFDF. In the former case, droplets larger than 100 μm still contribute to a significant portion of the liquid volume flux, whereas in the later, the volume flux is comprised of droplets in a much narrower band of sizes, of the order of tens of microns. This is due to the synergistic contributions of both swirl and electric charge/field, that both affect the VFDF in a similar manner, i.e. producing of smaller droplets overall, most likely through the break-up of larger droplets that would be present in the absence of swirl and electric field.

To summarize the results of the droplet population statistics, we use the mean diameters described in earlier chapters. Figures 5.10 and 5.11 are similar to the plots of mean diameters shown in the previous chapter but include the measurements with swirl. The reader will notice that addition of swirl did not change the trends with increasing voltage for any of the differently weighted droplet diameters. The main difference worth noting is that addition of swirl resulted in larger arithmetic (d_{10}) and surface area mean (d_{20}) diameters, similar volume mean (d_{30}) diameters and smaller Sauter mean diameters (d_{32}) and volume-flux-weighted mean diameters (d_{43}). This can be understood in the context of the distributions shown above, where addition of swirl leads to sprays with narrower droplet size distributions.
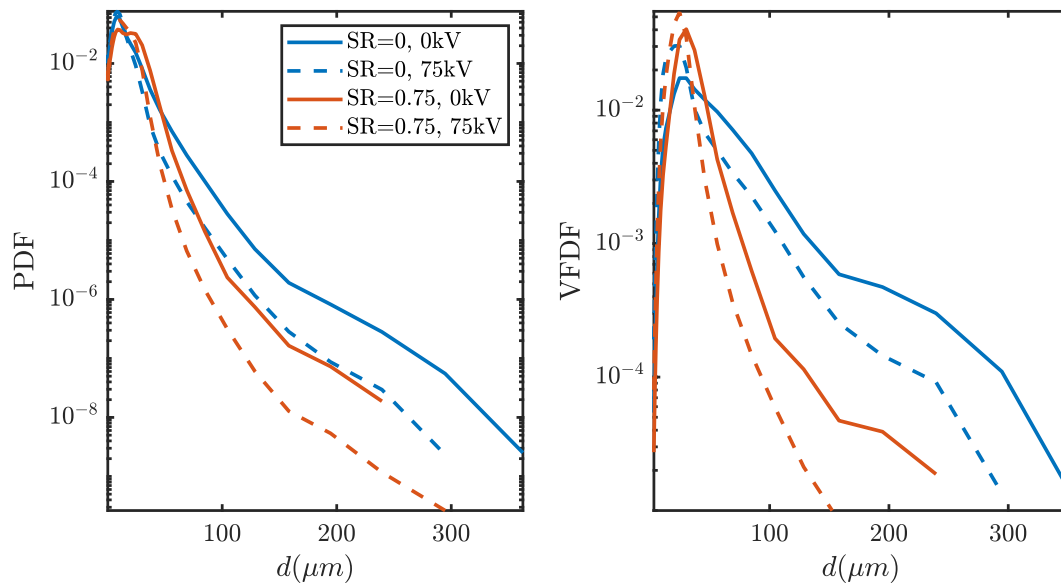
Figure 5.9: Probability density function and liquid volume flux density function for M=100 at 0 and 75 kV and SR 0 and 0.75 computed for a cross section of the spray.

5.1.5   Volume Fraction Measurements

Finally, let us consider results for the volume fraction of the spray. Figures 5.12-5.14 show volume fraction profiles at the three swirl ratios studied and for several applied voltages, at M=5 (figure 5.12), M=25 (figure 5.13) and M=100 (figure 5.14). The volume fraction profiles for the swirling flow cases show the non-monotonic dependence on radial coordinate, reminiscent of the behavior observed for the liquid volume flux. The maxima of the volume fraction were observed at locations between 3 and 4 d_g for swirl ratios 0.5 and 0.75. In all cases, the effect of the electric field was to reduce the maximum volume fraction as well as the radial slope, thus generating smoother and flatter volume fraction profiles. These effects are most striking for the lowest momentum ratio. Notice that variations in the volume fraction for M=5, SR=0.75, and 75 kV are about one sixth of the variations in volume fraction for the same momentum ratio in the absence of swirl and electrostatic forcing.
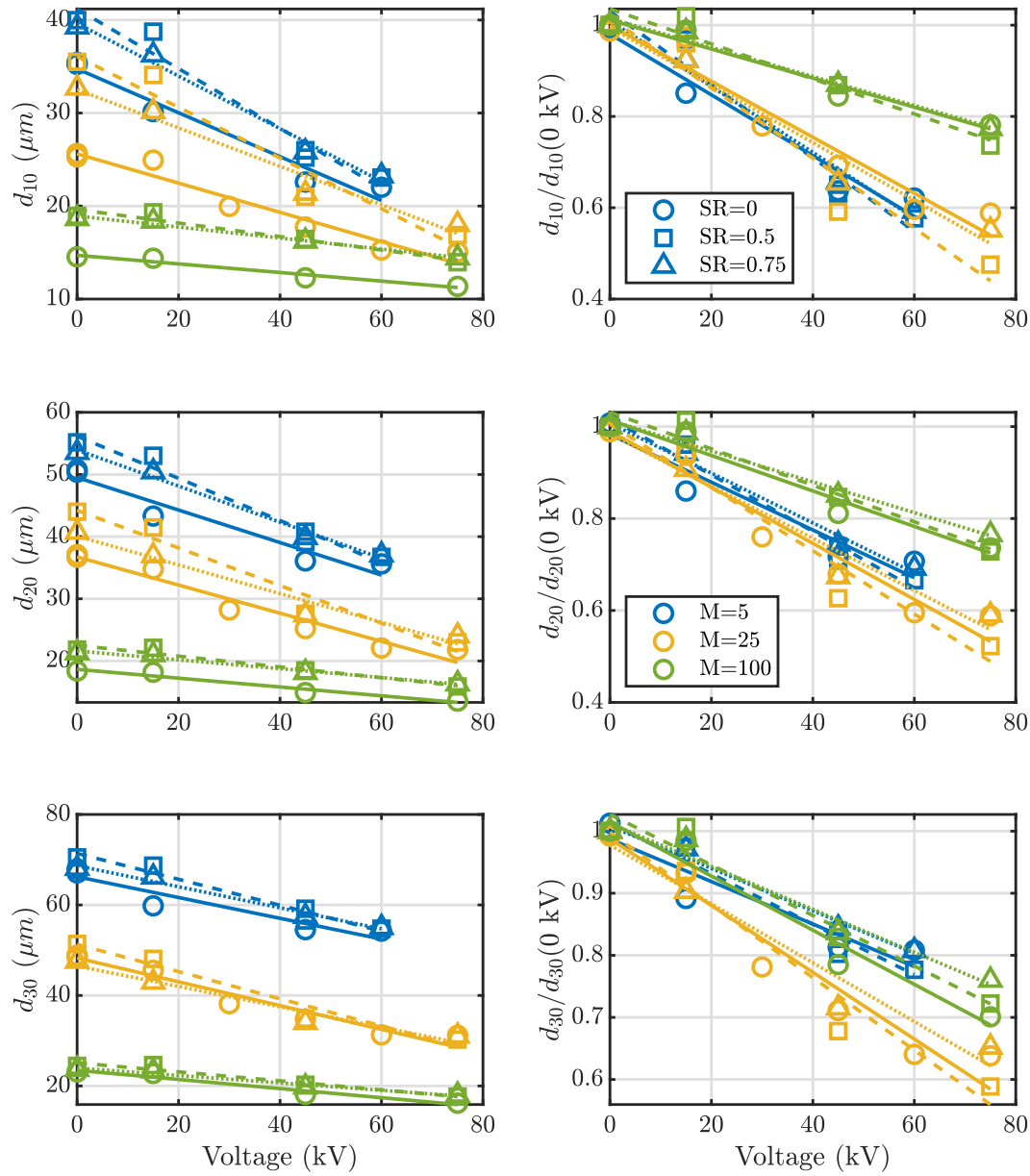
Figure 5.10: d_{10}, d_{20}, and d_{30} as a function of applied voltage for three momentum ratios and three swirl ratios. The mean diameters in microns (left) and normalized by the corresponding values at zero voltage to illustrate fractional changes (right). Dashed lines show linear fits to illustrate the trends observed for increasing electrify field strength.
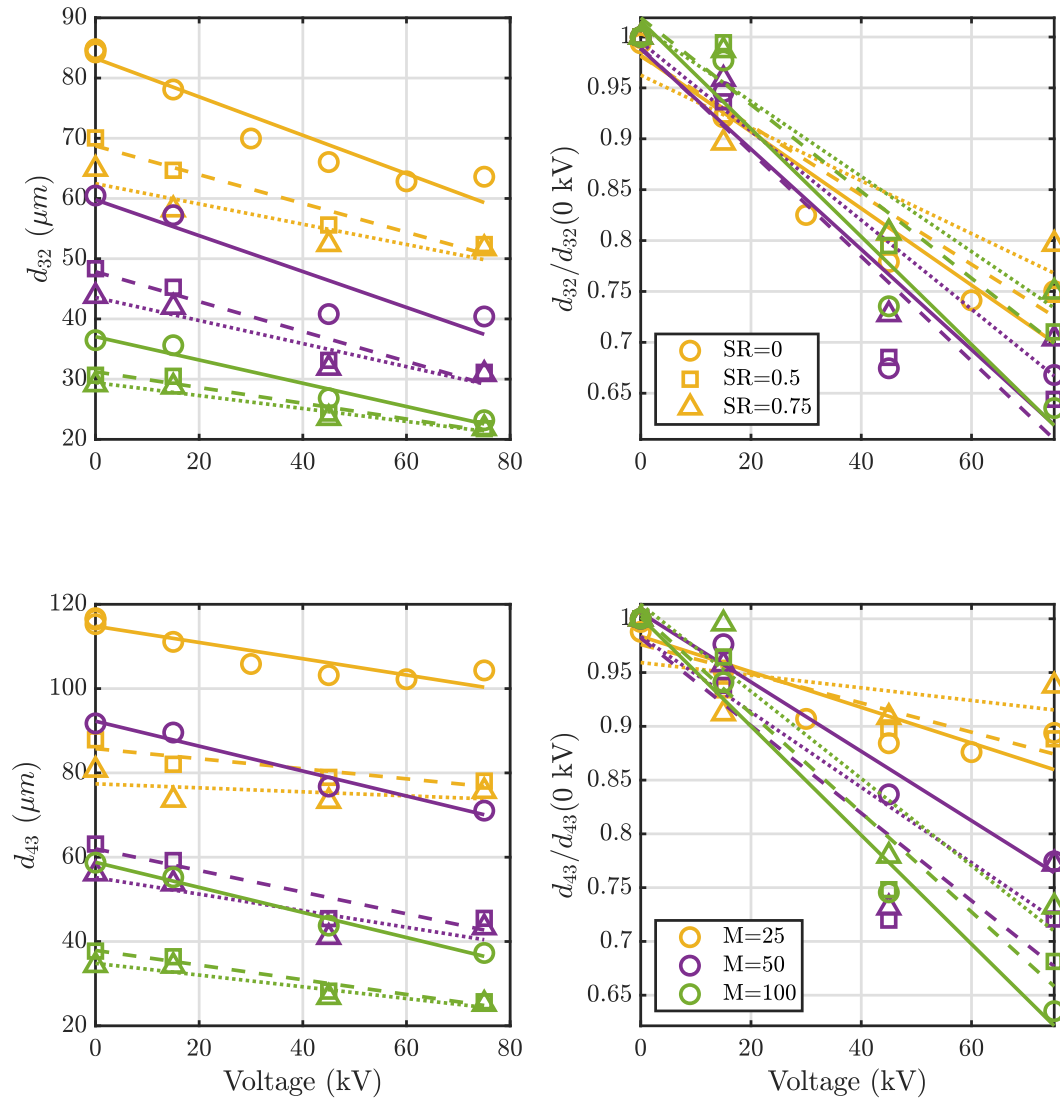
Figure 5.11: d_{32} and d_{43} as a function of applied voltage for three momentum ratios and three swirl ratios. The mean diameters in microns (left) and normalized by the corresponding values at zero voltage to illustrate fractional changes (right). Dashed lines show linear fits to illustrate the trends observed for increasing electrify field strength.
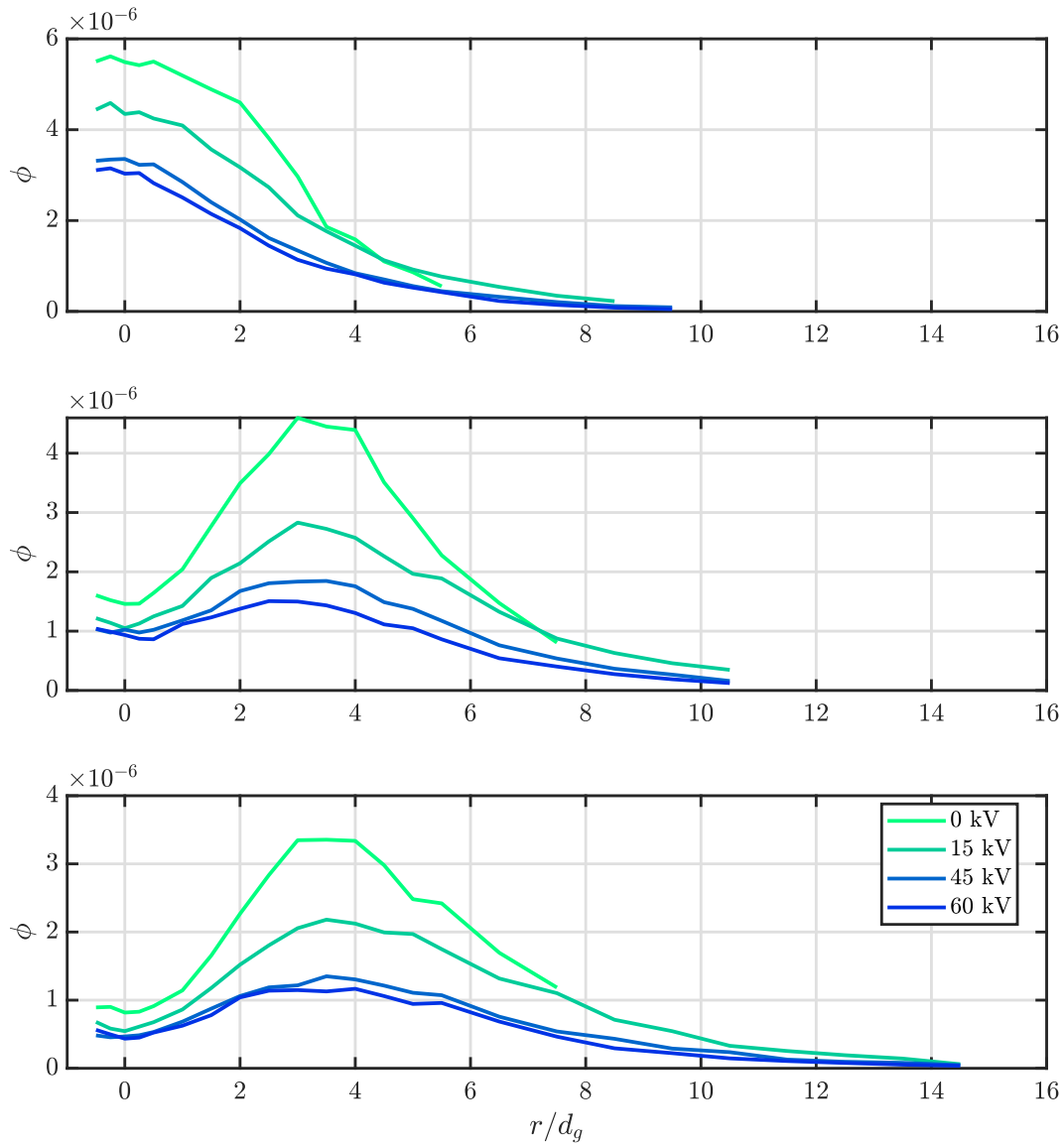
Figure 5.12:   Volume fraction at M=5 and SR=0 (top), 0.5 (middle) and 0.75 (bottom).
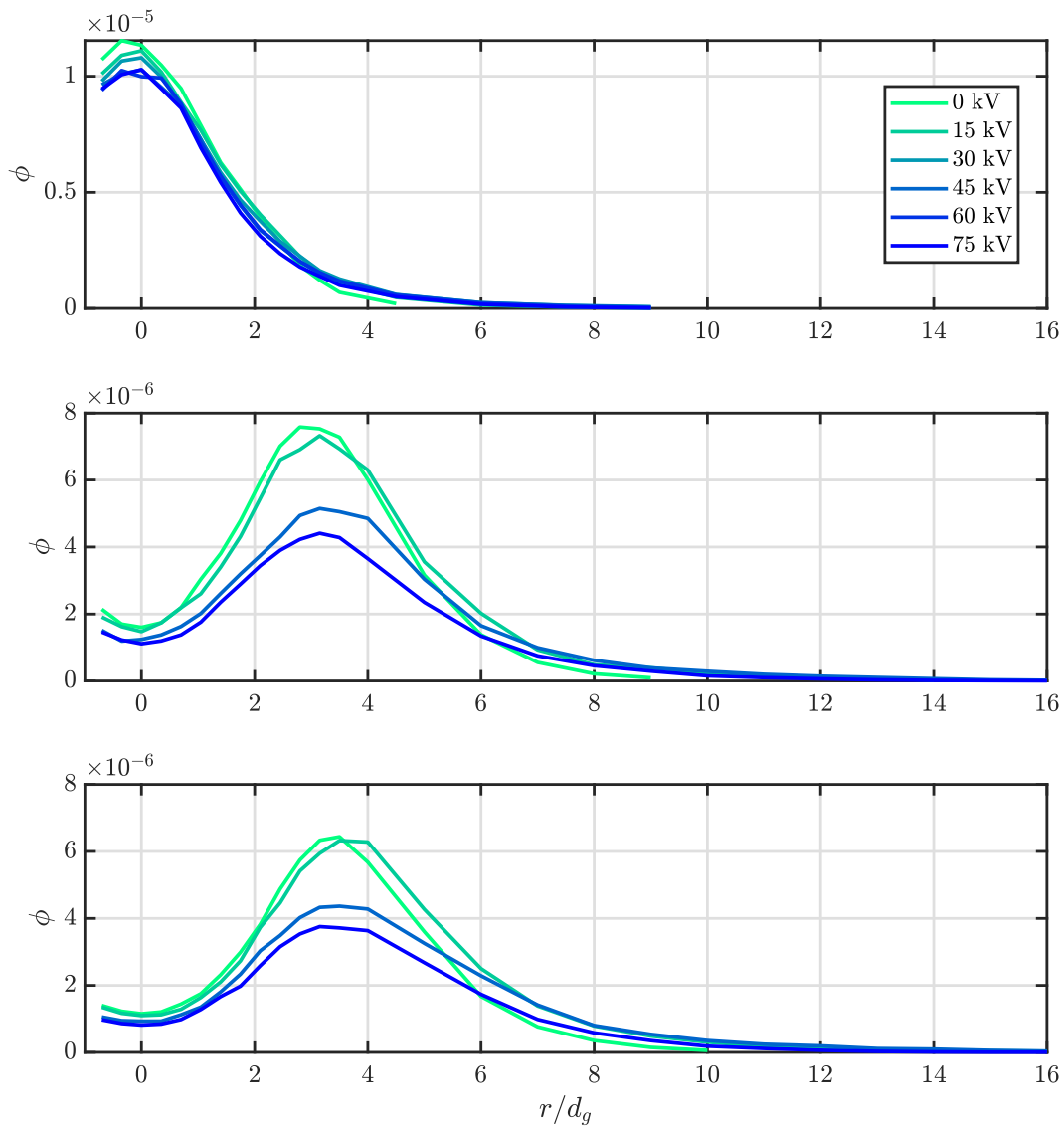
Figure 5.13: Volume fraction at M=25 and SR=0 (top), 0.5 (middle) and 0.75 (bottom).
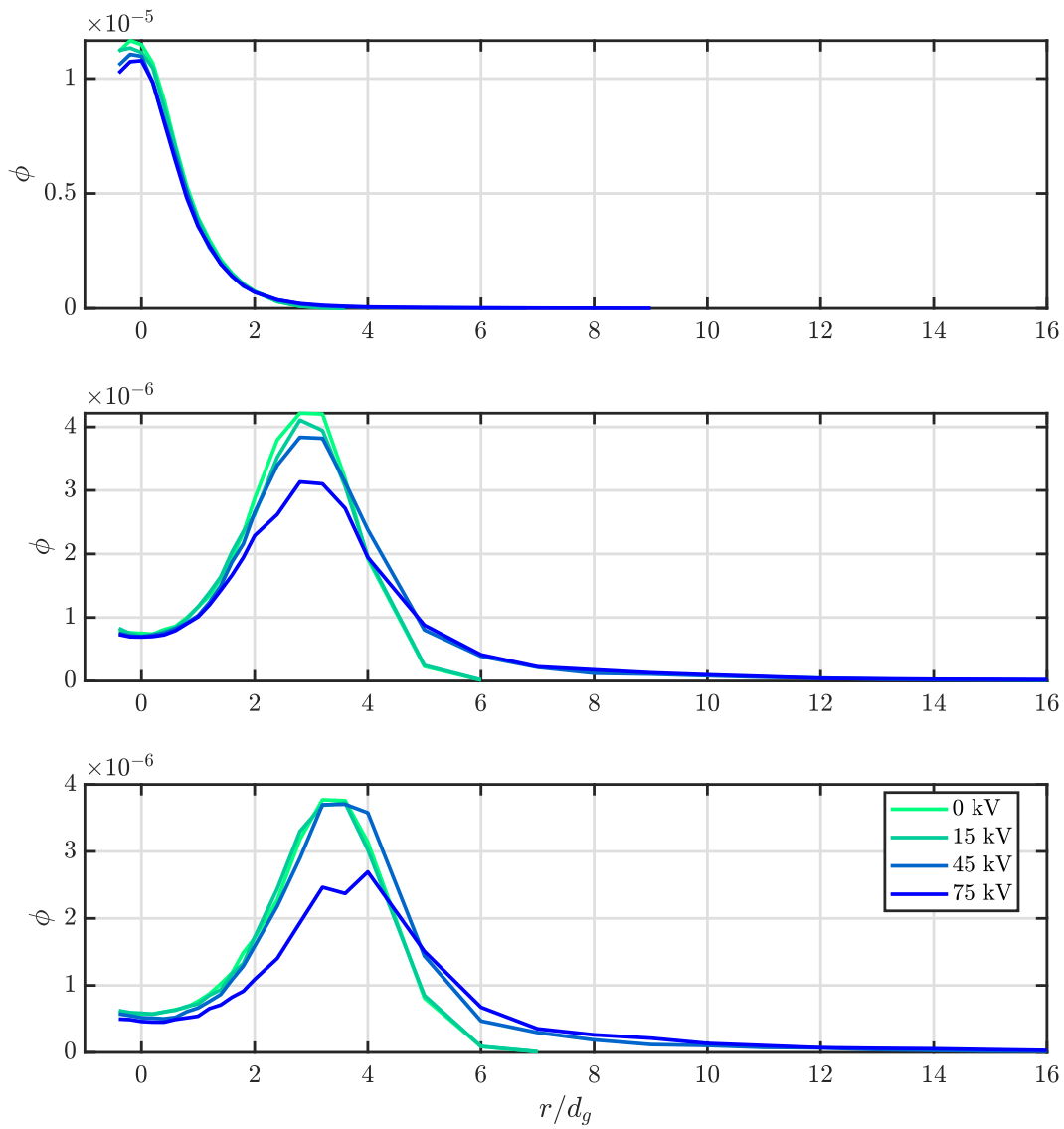
Figure 5.14: Volume fraction at M=100 and SR=0 (top), 0.5 (middle) and 0.75 (bottom).

5.2 Discussion

We explored the combined effects of swirl and electric charge/field on the velocities and sizes of the droplets produced by a coaxial atomizer. The addition of swirl resulted in a faster spreading gas jet that imparted large radial velocities to the droplets with greater inertia, modifying the liquid volume flux and volume fraction profiles, so that they had non-monotonic dependency with the radial coordinate. These profiles exhibit maxima at radial locations close to $2r_{1/2}$. Moreover, increasing the swirl ratio increases the mean velocity differences across different droplet class sizes. Furthermore, the increased spreading rate due to swirl and electrostatic acceleration resulted in sprays with detectable fluxes up to the edge of the electric field plates.

The similarity of the values of the radial gradients of radial velocities across momentum and swirl ratios in the presence of electric charge/field indicate that the electrostatic forcing represents the dominant force on the droplets away from the center of the spray. These gradients were observed to decrease with increasing swirl ratio, only for the two highest values of the momentum ratio; an observation that can be explained by looking at the mean diameter profiles. The mean diameters at the edge of the electrified spray for a momentum ratio of 25 were similar for all swirl ratios (figure 5.7), whereas the mean diameters at the edge of the electrified spray for momentum ratio of 100 increased with increasing swirl ratio (figure 5.8). This indicates that for the largest momentum ratios, the swirl can impart enough inertia to relatively small droplets, that are already accelerated by the electric field, that they can reach the edges of the spray. This combined effect results in a spray that is substantially different than the base state ($SR = 0$, $E = 0$) with a narrower distribution of droplet sizes and smaller mean diameters.

The results presented here illustrate the wide range of spray profiles and droplet size distributions that can be generated with a relatively simple coaxial atomizer with variable swirl and electrostatic forcing. One of the most striking features arising from the combined effect of swirl and electrostatic actuation is the reduction of the Sauter mean diameter and

the narrowing of the droplet size distributions, reductions that can be achieved at a negligible energetic cost relative to the cost of increasing the momentum ratio (we can compare the electric power output of the order of a few watts, with the power required for gas compression that drives the gas flow rates, which is of the order of thousands of watts). In addition, combining the effects of swirl and electrostatic forcing allowed for fairly uniform spatial distributions of liquid volume fraction. These experimental observations are a good indication of the possibilities for multiphysics spray control, where a simple system with three control parameters (Q_{ns}, Q_{sw} and E) can provide a wide range of possible spray spatial distributions and characteristic droplet sizes. This work also shows that, even for high momentum ratio sprays relevant to industrial applications such as coatings or combustion, electrification has a strong effect on the spray features that can be harnessed in real-world situations.

Chapter 6

FEEDBACK CONTROL OF COAXIAL ATOMIZATION BASED ON THE SPRAY LIQUID DISTRIBUTION

We demonstrate a novel implementation of real-time feedback control on the structure of the spray produced by a two-fluid coaxial atomizer. The ratio of angular to longitudinal gas flow rates, called swirl ratio, as well as the total amount of gas coflow are used as the actuation at the nozzle. The swirling and swirl-free gas flow rates are individually set by the control algorithm, with the control objective set based on an optical absorbance radial profile that is related to the liquid volume fraction across the spray. We analyzed the liquid volume fraction profiles measured in open loop by means of singular value decomposition and principal component analysis (PCA) and found that the different states of the spray across a wide range of operating conditions can be described with fidelity by three principal components. The control algorithm maps the resulting state PCA projections to the control variables. Real time control of the spray is achieved over a wide range of operating conditions (gas-to-liquid momentum $1 - 20$ and swirl ratios $0 - 1$).[1]

Here, we present a method to perform feedback closed-loop control of a spray atomizer where the control input consists of measurements of light attenuation across the depth of the spray at 10 gas diameters downstream of the nozzle and where the control actuation is on the swirl and no-swirl gas flow rates (defined over ranges that span the desired momentum ratios and swirl ratios of interest). We demonstrate the feasibility of real-time spray control in a two-fluid atomizer, using a three-parameter Principal Component Analysis (PCA) description of the state of the spray from fast measurements and a two-input control algorithm.

---

[1]This chapter is and adaptation of work published in reference [46]
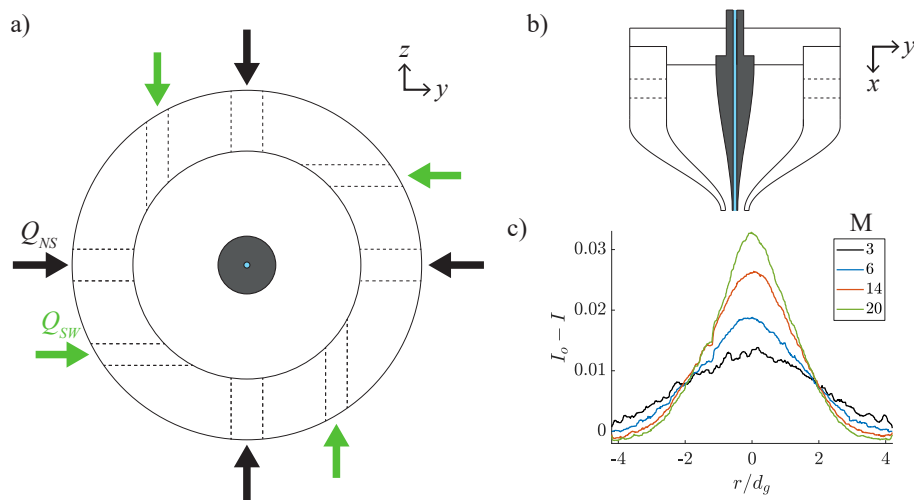
Figure 6.1: (a) Transverse cut of the nozzle along the gas inlets plane showing the liquid channel in the middle and the eight inlets for gas. (b) Cross section of the nozzle along the liquid channel axis. (c) Representative samples for the absorbance profiles, in arbitrary units, at different momentum ratios in the absence of swirl.

6.1   Spray Transverse Profile Attenuation Measurements

6.1.1   Light Attenuation Measurements and Analysis

Light attenuation through line propagation across the spray is measured by a linear CCD camera (Thorlabs model LC100) with a red LED panel providing a uniform source of illumination, in a configuration analogous to shadowgraphy. Representative spray transverse profiles of light attenuation, associated with liquid volume fraction, are shown in figure 6.1. Despite the low optical density of the spray in the mid-field, the attenuation across the spray cross-section is of the order of a few percent, which is well within the line camera 12-bit resolution and above the measurement noise, which was characterized before data collection as 0.04 percent of the unattenuated signal.

We study swirl ratios in the range 0 to 1 and momentum ratios in the range 2 to 20. Data shown here spans this range adjusting the control inputs (no-swirl and swirl volume
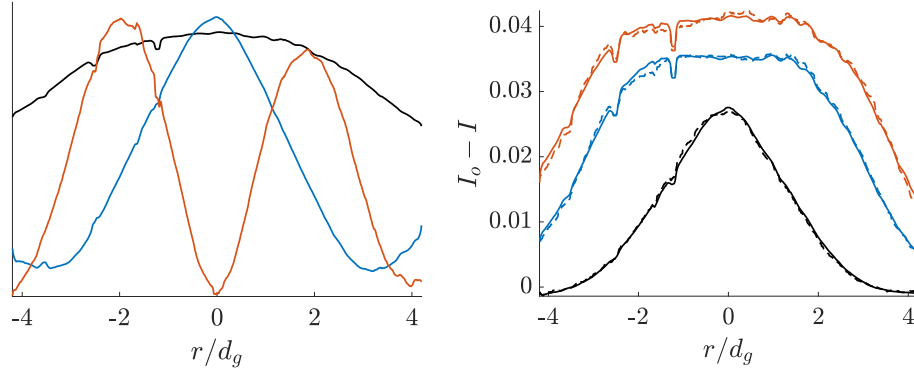
Figure 6.2: (Left) First Three Principal Components in arbitrary units. (Right) Observed profiles (dashed lines) and principal component reconstructions (solid lines), for $M = 13.6$ and $SR = 0.2, 0.5, 0.8$ from bottom to top.

flow rates, Q_{ns} and Q_{sw}, respectively) within these limits. Light attenuation profiles, used as a surrogate of the spray liquid volume fraction, were collected in open loop sequence. Said profiles were analyzed using principal component analysis. PCA revealed that the three main modes serve as a good basis to represent most of the energy in the observed shapes, as shown in figure 6.2.

The principal components identified as a basis to represent the light attenuation are normalized to form an orthonormal basis onto which to project the instantaneously measured profiles. As a result, the spray state that is the goal of the control algorithm, can be described as a spatial profile using only three parameters. A two by three transfer function relates the 3 values that define the control goal to the 2 control variables. Given the projections onto the basis vectors, a least-squares fit for the flow parameters produces a linear function of the projection parameters.

We varied the values of the control parameters Q_{ns} and Q_{sw} so as to uniformly sample the momentum and swirl ratios of interest (as the spray physics are dominated by these nondimensional groups). The evolution of the principal component coefficients v_i with Q_{sw} and Q_{ns} is roughly linear. Each control parameter can be varied independently of the other
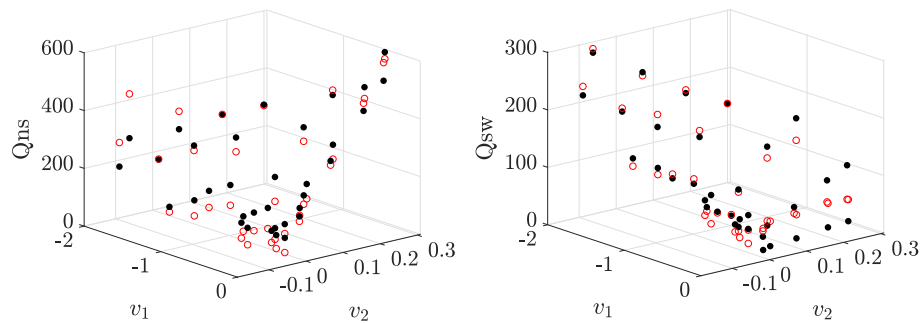
Figure 6.3: Observed (black dots) and predicted (red circles) values of the no-swirl (Left) and swirl (Right) gas flow rates.

which justifies the use of a linear fit (e.g. $v_i \approx a + bQ_{ns} + cQ_{sw}$).

Figure 6.3 shows the observed and predicted values of the swirling and non-swirling components of the gas flow rate based on a linear least squares fit to the principal component representation of the corresponding profiles. It can be observed that the fit reproduces the overall trends reasonably well ($R^2 \approx 0.9$) and that it fails mostly for low values of the gas flow rate.

6.2   Real-time Feedback Control Implementation

6.2.1   Control Algorithm and Performance

The real-time control is performed by setting a goal profile in terms of its principal component representation (any three values of the PCA basis, not a preset of values tested a-priori). The control algorithm minimizes the root mean square error (RMSE) of the profile measured instantaneously relative to the goal profile. This is achieved in two steps. First, an initial guess based on the least squares fit indicates the goal for the swirl and no-swirl components of the gas flow. Second, the magnitude of the change in both controls is adjusted by the magnitude of the root mean square error. A proportional–integral–derivative controller (native Labview implementation) is used to control the proportional valves based on the flow
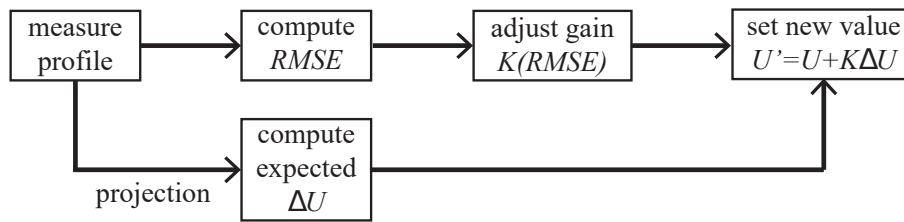
Figure 6.4: Control diagram for our proposed method.

meters and the computed set-point for the flow rates. This process is iterated to attain a tolerance in the cost function (difference between goal and actual light attenuation profiles). A schematic of the control algorithm is presented in figure 6.4.

The control algorithm is tested on a variety of random conditions showing quick and robust convergence to each of the random goal profiles (figure 6.5). The proportional valves used for both gas inputs have response times of the order of a fraction of a second, and this sets the characteristic time required for the system to stabilize. Interestingly, in some cases the convergence is non-monotonic as both control parameters are varied. The RMSE increases as the control changes both inputs semi-independently, and then drastically diminish as one control parameter reaches its optimum value, with the control algorithm then refining convergence by fine-tuning the other input in small increments. This can cause large changes of the spray features, which explain why the RMSE can increase before decreasing to below tolerance.
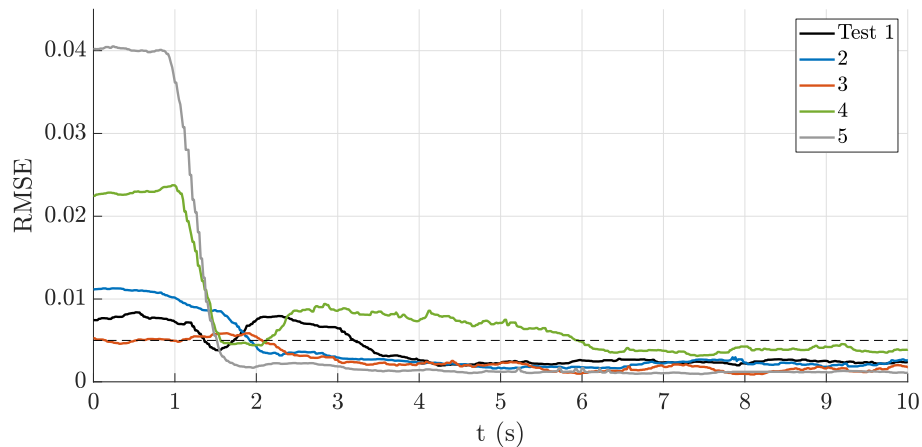
Figure 6.5: Root mean square errors along time, between the goal profile and the instantaneous profile for five cases corresponding to videos in supplementary material.

6.3 Conclusions

We achieved real-time feedback control of a high momentum spray based on a low dimensional representation of spray light attenuation that can be measured as a surrogate of liquid volume fraction and processed in real-time. To the best of our knowledge, this is the first instance of the implementation of such control in the literature. The control algorithm showed robust performance and response times well-matched to the available actuation in this high-momentum spray (in the order of fractions of a second). It is possible to rigorously correlate the light attenuation profile to physically meaningful characteristics of the spray, such as liquid volume fraction, opening the opportunity to use the proposed control strategy to maintain certain spray quality for a variety of applications where quantitative goals (not random profiles) are well-defined. Future work will focus on these aspects, as well as on implementing multiphysics control actuation, such as electrohydrodynamic effects and acoustic forcing.

Chapter 7

FEEDBACK CONTROL OF THE SPRAY LIQUID DISTRIBUTION OF ELECTROSTATICALLY ASSISTED COAXIAL ATOMIZATION

Electrostatic actuation is used for real-time multiphysics feedback control of two-fluid coaxial atomization. This actuation is added to the modulation of the axial and angular momentum of the turbulent coaxial gas stream, for a total of three actuators to control atomization. We characterize the spray real-time response through optical scattering measurements of radial liquid distribution. We apply principal component analysis on the scattering radial profiles and correlate the first three principal components to the three control inputs. The control algorithm continuously adjusts the three inputs to minimize the difference between a goal radial profile representing the desired spray state and the profile observed in real time. This real-time multiphysics (gas momentum plus electrostatic repulsion) control on the liquid distribution in a two-fluid coaxial spray is a novel contribution to the archival literature on this technology.[1]

Here, we present results for an electrostatically assisted two-fluid coaxial atomizer, where three control inputs shape the spray liquid distribution in real-time feedback. The sensing of the spray state is done through optical scattering, measuring a radial profile of liquid volume fraction at 18.5 gas diameters downstream of the nozzle. Applied voltage on the far field is actuated on, in addition to the actuation on the swirl and no-swirl gas flow rates.

---

[1]This chapter is and adaptation of work published in reference [47]

7.1 Experimental Setup

7.1.1 Atomizer and Flow Loop

The two-fluid coaxial atomizer used in this work has been characterized extensively [36, 46]. For the electrostatic actuation, the nozzle is placed between two parallel metallic plates and a voltage, variable between 0 and 25 kV, is equally applied to both of them, while the nozzle remains grounded. The liquid flows through a straight needle at the center of the gas nozzle at a constant flow rate, consistent with fully developed laminar Poiseuille flow. The axial component of the gas flow is controlled by the gas flow rate from four diametrically opposed, radially oriented, inlets perpendicular to the axis of the nozzle. The angular component of the gas flow is controlled by the gas flow rate from four inlets that are oriented tangential to the outer wall of the nozzle. The gas and liquid flow rates are controlled independently with three proportional valves and a high voltage power supply controls the applied potential. A plan and side views of the nozzle, including the parallel plates, are shown in figure 7.1. The liquid nozzle internal and external diameters are respectively 2 and 3 mm, while the gas nozzle internal diameter is 10 mm.

This electrohydrodynamic multiphase flow can be characterized in terms of three dimensionless groups: the gas-to-liquid momentum ratio $M = \rho_g U_g^2 / \rho_l U_l^2$, the swirl ratio $SR = Q_{ns}/Q_{sw}$, and the ratio of electric to surface tension energy, $\Gamma = \frac{\sigma_0^2/\epsilon_0}{\gamma/r_0}$, where the subscripts g and l denote the gas and liquid phases respectively, ρ_i are the mass densities. The mean velocities, U_i, are calculated from the volume flow rates Q_i, the subscripts ns and sw denote the no-swirl and swirling components of the gas flow rate respectively, and γ is the surface tension between the liquid and gas phases. For the electrostatic variables, σ_0 is the surface charge density at the liquid-gas interface, ϵ_0 is the permittivity of free space and r_0 the liquid needle radius. Our working fluids were ambient air and water with a small concentration of sodium chloride dissolved, with a conductivity of 2000 $\mu S/cm$. For all the results presented, the liquid flow rate was kept at $Q_l = 99(\pm 2.5) ml/min$, corresponding to a liquid Reynolds number $Re_l = 1200$. The total gas flow rates explored in this study were in
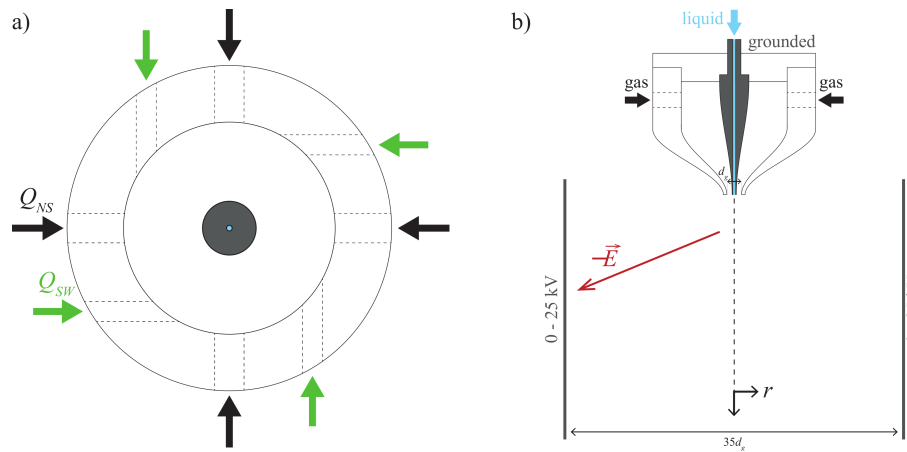
Figure 7.1: (a) Plan view of the nozzle along the gas inlets plane showing the liquid channel in the middle and the eight inlets for gas. (b) Side view of the atomizer including the parallel plates (not to scale).

the range $150 - 860\ SLPM$, resulting in velocities between 34 and 200 m/s and momentum ratios between 5 and 175. For a given total gas flow rate, the swirl ratio was varied in the range 0 to 1. Charge densities up to 3 C/m^3 were observed.

7.1.2   Light Scattering Measurements

The control sensing consists of light scattering measurements along a radial profile through the spray. In contrast with the attenuation measurements used in our previous work, light scattering measurements allow for a more robust detection of spray features at lower volume fractions, which enables detection of lower mass loading reliably, at higher gas momentum ratio. A collimated light sheet is shined through the spray at an angle of 30 degrees with the horizontal plane, intersecting the spray between 18 and 19 d_g downstream from the nozzle (the gas inner diameter, $dg = 1$ cm and the plates are $35d_g$ apart).

The light refracted by the spray droplets at 150° forward scattering is collected by a linear CCD array camera (Thorlabs model LC100), forming a radial transverse profile , perpendicular to the spray axis and normal to the plane of the metallic plates. A Zeiss 100
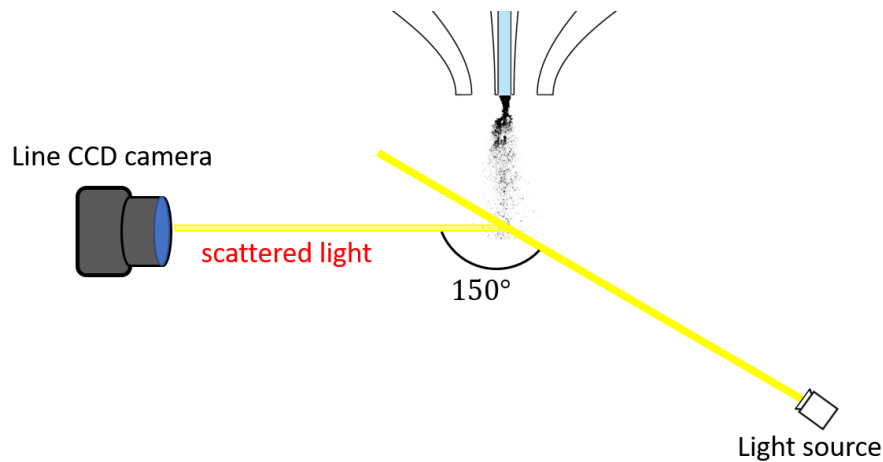
Figure 7.2: Geometry of light scattering for spray visualization, showing scattered light captured by the line CCD at an angle of 150 degrees to the incident collimated plane of light.

mm macro lens was used for visualization, yielding a resolution of 77 μm, with a field of view 16 cm wide. Figure 7.2 shows a schematic of the illumination mode used for measuring the radial profiles of the spray liquid distribution. As seen in the figure most of the spray width was captured in the collected images, with the scattered intensity at the edges approaching zero.

The optical scattering real-time sensing is able to capture the different features of the spray over the range of control inputs studied. We explored momentum ratios from 5 to 175, swirl ratios from 0 to 1 and applied voltages of 0 to 25 kV (corresponding to $\Gamma = 0 - 1000$). Appropriate filtering and sliding-time averaging reveal consistent profiles for varying actuation in spite of the unsteadiness of the instantaneous liquid volume fraction signal, intrinsic to turbulent flows. Figure 7.3 shows a small set of representative profiles that illustrate some of the features of the spray at different values of the control inputs. As the momentum ratio increases, scattering increases because the droplet number-density increases, especially near the centerline of the spray. Increasing the swirl ratio broadens
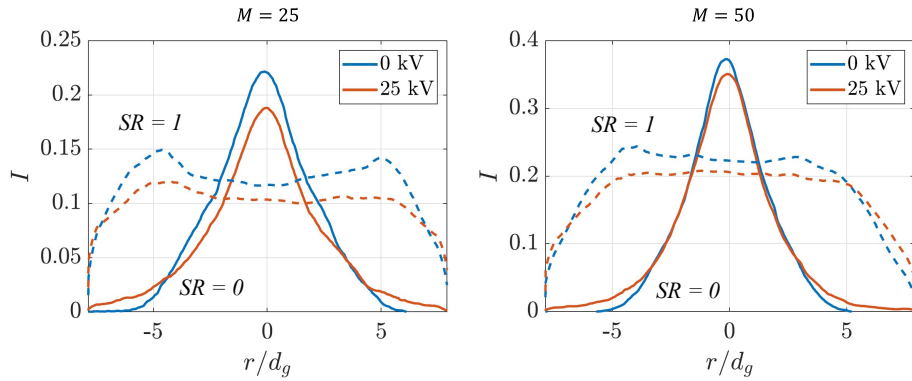
Figure 7.3: Radial profiles of light scattering (representing liquid volume fraction) with (red) and without (blue) electrostatic actuation for swirl ratios of zero (solid lines) and swirl ratio of one (dashed lines) Left and right are respectively at a momentum ratio of 25 and 50.

the spray as droplets are transported away from the spray centerline, but may result in a double bump feature in the scattered transverse profiles. Finally, we observe a broadening of profiles as we increase the applied voltage, resulting both from the electrostatic repulsion among charged spray droplets and by the electric field established between the grounded nozzle and charged plates.

7.1.3 Principal Component Analysis of Light Scattering Profiles

Principal Component Analysis was performed onto a large data set collected over a wide range of control inputs, in order to arrive at a reduced-order representation of the data. The dataset included measurements for 140 different spray conditions with around 250 profiles for each condition. The parameter space sampled was comprised of combinations of 7 momentum ratios between 5 and 170, 5 swirl ratios between 0 and 1 and 4 voltages between 0 and 25 kV. We used a standard implementation of PCA using MATLAB's Singular Value Decomposition built-in functions and standard algorithms as the ones detailed by Kutz. [31]. Most of the features of the collected profiles could be adequately and sparsely represented by the main three principal components which contained about 84% of the energy. As shown in Figure

7.4 accurate reconstructions were achieved with the first three principal components.

More importantly, the distance between the two profiles as measured by the integral over the profile of the normalized root-mean-squared difference and by the sum of the normalized root-mean-squared difference of their three principal components closely match each other (Figure 7.4b)). This property guarantees that two profiles that are close in the principal component parameter space will indeed be very similar in physical space, such that convergence of the principal component coefficients ensures that the desired profile goal will be achieved.

The resulting reduced-order representations were correlated to the control inputs using a least squares linear fit, in a 3 by 3 matrix, in order to obtain a linear map between the observed profiles and the control variables.
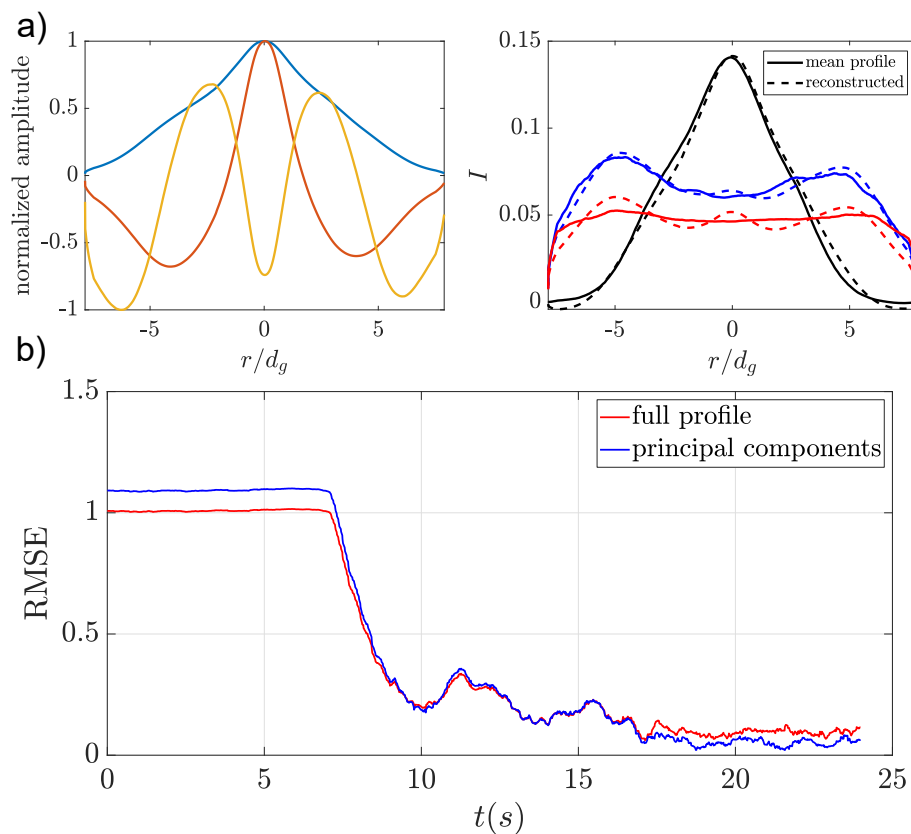
Figure 7.4: (a) First Three Principal Components normalized by their maxima (Left). Measured profiles (solid lines) and principal component reconstructions (dashed lines) (Right). (b) Normalized root mean square error time series between the goal and the real-time measurement computed from the full data (solid) and the PCA decomposition (dashed).

7.2   Real-time Feedback Control Implementation

7.2.1   Control Performance

The goal of the spray control is to drive the experimental spray towards a desired state, characterized by a liquid volume profile measured with the light scattering on the line CCD camera. The control inputs are adjusted in real-time by the closed-loop control algorithm, based on a linear mapping obtained from the open loop investigation with a gain that is
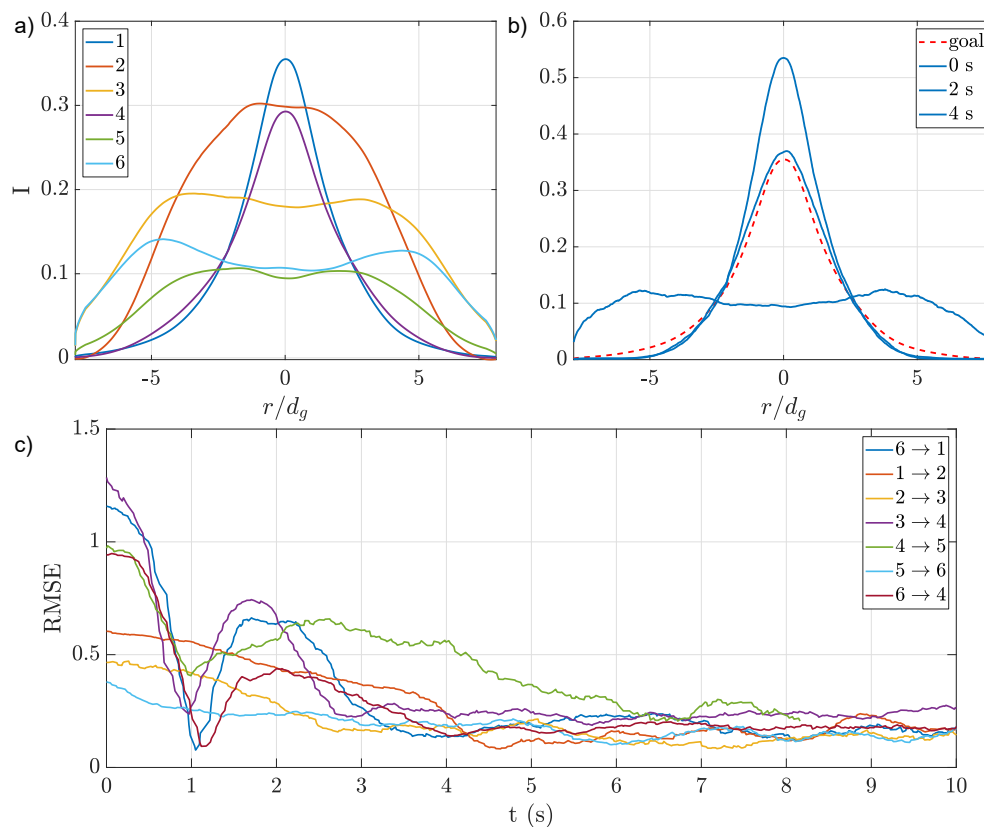
Figure 7.5: (a) Goal profiles used to test the control algorithm as shown in the supplementary video. (b) Example of control algorithm convergence, progressing from profile 6 to 1. (c) Normalized root mean square errors between real-time profiles and goals (desired light profiles in the spray). The legend indicates the starting profile as numbered in the supplementary video and the goal profile.

adjusted based on the real-time error. This results in an closed-loop iterative approach (with a frequency of iteration being approximately 100 Hz) with control input adjustments that decrease as the desired profile is approached [46]. The algorithmic gains are set as a compromise between convergence speed and stability/robustness to process noise.

As seen in figure 7.5 (and in the movie included in the supplementary material), our control algorithm leads to convergence upon a wide variety of specified goals. Table 7.1 below

presents the mean convergence error, $\langle \varepsilon \rangle$, and the standard deviation of the convergence error, ε', for the control examples in the supplementary video and in figure 7.5. The standard deviation of the normalized convergence error is a fraction of the convergence error. The signal shows greater variance at higher values of the swirl ratio, which is also apparent in higher variance of the convergence error for such cases.

Table 7.1: Closed loop control performance metrics.

M	SR	Voltage (kV)	$\langle \varepsilon \rangle$	ε'	$100 \cdot \frac{\varepsilon'}{\langle \varepsilon \rangle}$
59	0.21	0.0	0.10	0.01	8.94
87	0.40	20.7	0.05	0.01	26.44
48	0.70	8.9	0.10	0.03	25.89
49	0.24	0.0	0.09	0.01	9.22
27	0.38	6.2	0.21	0.03	16.29
22	0.56	8.8	0.05	0.01	28.35

7.3   Comparison of Control Signal with PDPA Measurements

The optical intensity signals collected were shown to reliably characterize different states of the system an correlate well with the control inputs. But in order to connect them with useful physical models of the state of the spray it is necessary to identify which spray property is best captured by our measurements. In this section we present results that correlate mean values of the state of the spray such as the volume fraction to the intensity signals used for control. We derive an approximate expression relating the detected signal intensity to an area fraction of the spray.

The radiant intensity $I(\theta)$ scattered from a small spherical particle of diameter D at an angle θ in the forward direction relative to an incident plane wave of irradiance E_0 is given

by [34]:

$$\frac{I(\theta)}{E_0} = \frac{D^2}{16}\left\{\alpha^2\left[\frac{2J_1(\alpha\theta)}{\alpha\theta}\right]^2 + \left[\frac{4m^2}{(m^2-1)(m+1)}\right] + 1\right\} \tag{7.1}$$

where $\alpha = \pi D/\lambda$ is the size number for a wavelength of incident light λ, J_1 is the Bessel function of first kind of order unity and m is the particle's index of refraction. We can simplify equation 7.1 by noting that for visible light, at 30° scattering angle and using the index of refraction of water the constant terms inside the brackets (i.e. the second and third terms) are more than an order of magnitude larger than the Bessel function term for particles larger than about 5 microns in diameter. Thus we can approximate the irradiance from a population of droplets with a volumetric number density distribution given by dN/dD to be:

$$\frac{I(\theta)}{E_0} = \int_0^\infty \frac{D^2}{16}\left\{\left[\frac{4m^2}{(m^2-1)(m+1)}\right] + 1\right\}\frac{dN}{dD}dD \tag{7.2}$$

where we have ignored the effects of multiple scattering, assuming a dilute spray approximation (naturally this would break down for axial locations too close to the nozzle). Hence we can write an approximation as:

$$\frac{I(\theta)}{E_0} \propto \int_0^\infty D^2\frac{dN}{dD}dD = \phi_A \tag{7.3}$$

where the integral, ϕ_A, can be understood as an area fraction; that is the area occupied by a two-dimensional projection of the drops onto a unit area surface.

Figures 7.6 and 7.7 show comparisons of the light intensity measurements at the line CCD detectors with different measures of the spray obtained from PDPA measurements. We hence define Phi_A as in equation 7.3, Phi as in equation 4.8 and MF as proportional to the normalized volumetric flux presented in chapter 4. We can see that for the case of no swirl (figure 7.6) both the normalized volume and area fractions agree well with the normalized intensity, whereas the normalized mass flux decays faster than the intensity signal. On the other hand once we add swirl to the gas coflow (figure 7.7) the area fraction correlates much better to the CCD intensity than does the volume fraction.

In addition to the light scattered from particles near the focal plane, the intensity at the detector is affected from attenuation as light travels across the spray. Hence, we consider the
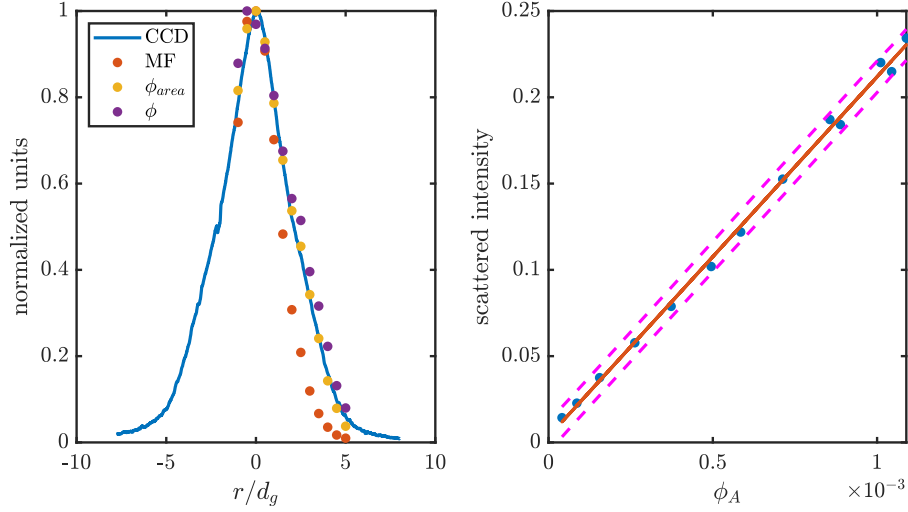
Figure 7.6: Scattered light intensity profiles compared to mass flux, area fraction and volume fraction estimates obtained from PDPA measurements for $M = 25, SR = 0$ and no electric field (left). Units are normalized by the maximum value of each quantity for a given profile. Scattered intensity measurements vs area fraction along with least squares fit and 95% confidence bounds in dashed lines (right).

attenuation that occurs due to scattering (in this situation attenuation due to absorption is negligible in comparison). The transmission law for a polydispersion of large particles can be written as [13]:

$$\frac{E}{E_0} = \exp\left[-\frac{3}{2}\left\langle \frac{\bar{K}\phi}{d_{32}} \right\rangle l\right] = \exp\left[-\frac{3}{2}\langle \bar{K}\phi_A\rangle l\right] \tag{7.4}$$

where $\bar{K}$ is the mean scattering coefficient, ϕ is the volume fraction, d_{32} is the Sauter mean diameter, l is the path length traversed by the light beam, and the angle brackets denote spatial averaging over the path length to account for the nonuniform distribution of the scatterers. Combining equations 7.3 and 7.4 we can write a relation between the intensity of light at the detector and the area fraction of the spray:

$$I_{detector}(r) \propto \exp[-\langle\phi_A\rangle]\phi_A(r) \tag{7.5}$$
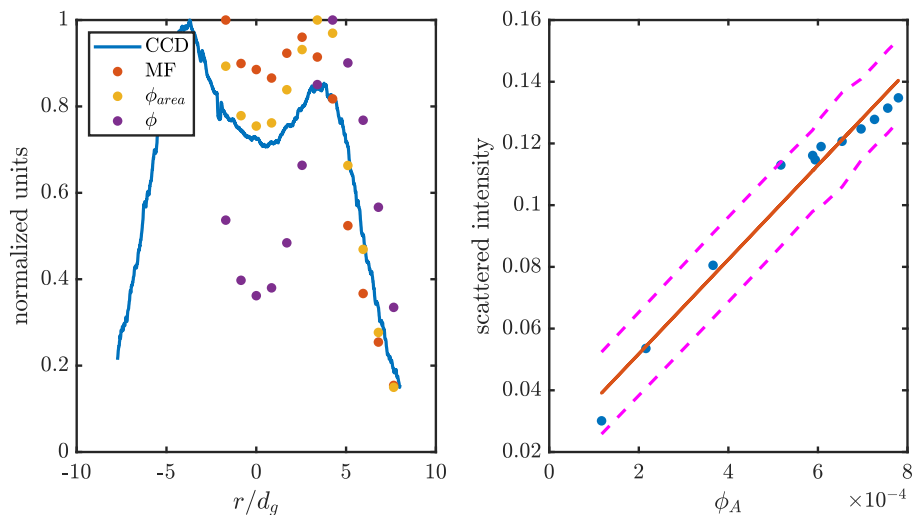
Figure 7.7: Scattered light intensity profiles compared to mass flux, area fraction and volume fraction estimates obtained from PDPA measurements for $M = 25, SR = 0.5$ and no electric field (left). Scattered intensity measurements vs area fraction along with least squares fit and 95% confidence bounds in dashed lines (right).

where we assume integration over a similar path length (the path length captured by the detector as the cross section of the spray).

We tested the expression 7.5 against the area fractions over a range of conditions and found a good correlation with the mean (time averaged) intensities at the CCD camera (figure 7.8). Thus we see that with appropriate calibration, simple scattered light measurements across a cross section of the spray can provides estimates of the spray liquid distribution in terms of the area fraction.
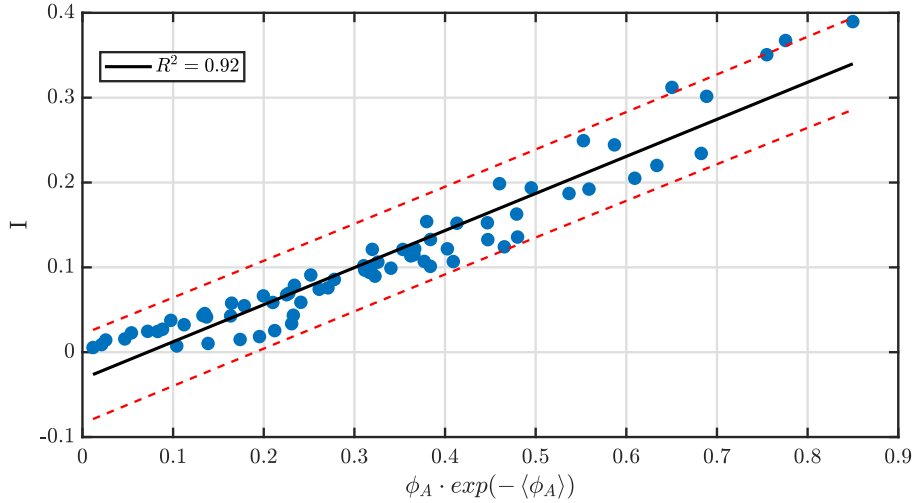
Figure 7.8: Scattered light intensity vs equation 7.7 along with least squares fit and 95% confidence bounds for profiles taken at several conditions of momentum ratio, swirl ratio and applied voltage.

7.4   Conclusions

We demonstrate multi-physics control, using an external electric field to both charge the spray droplets and attract the charged droplets radially outwards as they flow downstream of the nozzle. This extends previous work on real-time feedback control of the spray liquid distribution in two significant ways: 1) adopting a more robust sensing technique that captures features of the spray more accurately, even in less dense sprays, over a broader range of momentum ratios and swirl ratios; 2) and by adding an electrostatic actuation. We also identified the scattered light measurements as being determined by the spray area fraction, thus indicating a simple measurement can be utilized to estimate the spray liquid distribution in near real time (assuming that the correlation found on average holds for the instantaneous measurements). To the best of the authors' knowledge, this is the first instance of real-time feedback control on the liquid distribution of a two-fluid coaxial spray using multiphysics actuation.

Chapter 8

GENERAL CONCLUSIONS

8.1   Near field: Impact of Electric Fields on Primary Breakup

This thesis investigates the impacts of electrostatic forcing on coaxial atomization using two different experimental setups. The first setup enabled us to explore the effects of different electric field geometries on the primary breakup of the liquid jet. Our results show that an electric field that generates substantial stresses opposing the direction of the flow can reduce the wavelength and increase the growth rate of the initial shear instabilities even at momentum ratios several orders of magnitude larger than the estimated electric Euler number. In contrast, an electric field of similar strength but pointing mostly radially was ineffectual in modifying the primary breakup.

A different configuration achieved Electric Euler numbers up to 10 and was capable of producing purely electrostatic breakup. It was shown that the electrostatic breakup dominated the large scale breakup mechanisms when the electric Euler number was five times larger than the momentum ratio. The transition between electrohydrodynamically dominated breakup and aerodynamically dominated breakup occurred at a lower gas-to-liquid momentum ratio with the addition of swirl to the coflowing gas jet. Even for the cases where the large scale deformations of the liquid jet were dominated by aerodynamic stresses, electrostatic forces were seen to introduce small-scale features, as revealed by increases in the curvature of the liquid core as well as its arc-length to intact length ratios. These small-scale features showed the morphology observed for electrohydrodynamic breakup, such as whipping and ramified instabilities. This is evidence that electrostatic stresses modified the primary breakup in a way that helps explain the reduction in mean droplet diameters observed with interferometric measurements.

8.2   Mid field: Impact of Electric Fields on Droplet Population Sizes and Transport

Electrostatic forcing was seen to reduce the mean droplet diameters of the spray even at momentum ratios an order of magnitude larger than the electric Euler number. These reductions in mean diameters were observed for low and high moments of the droplet diameter size distribution (i.e. d_{10} and d_{30}). Moreover, the electric forces were seen to dramatically increase the radial transport of droplets and the electric forces were seen to dominate the transport far from the centerline. We observed preferential radial transport of small droplets, consistent with electric charge densities that were a decreasing function of size. The radial velocities far from the centerline were consistent with the hypothesis that the droplets' volume charge density followed a power law close to the Rayleigh limit: $\rho_c \propto d^{-1.5}$.

Addition of swirl to the gas coflowing jet along with electrostatic forcing was observed to produce droplet populations with a substantially narrower diameter distribution and smaller mean diameters. It is worth noting that these substantial reductions in droplet size, were achieved without modifying the liquid-gas mass ratio, and with a minimal energetic cost compared to an equivalent increase in gas-to-liquid momentum ratio. Moreover, combining swirl with electric forcing allowed for sprays with more uniform radial profiles for mean diameter, as well as liquid volume flux.

8.3   Multiphysics Control of Atomization

Real time feedback control of atomization based on optical scattering and attenuation measurements of the radial liquid distribution has been demonstrated. The optical measurements were reduced to a low order representation based on their first proper orthogonal modes, and the proper orthogonal coefficients were connected to the control inputs. This enabled fast and robust real time feedback control of atomization. This represents the first demonstration of multiphysics real-time feedback control of a two-fluid atomizer and the first using electrostatic forcing. The scattering measurements were observed to capture the spray liquid area

fraction well, thus revealing the connection between the main features of the area fraction distributions and the control parameters in our system.

Other research efforts not discussed in this dissertation included the use of acoustic fields in assisting and modifying atomization and transport, characterization of the 3 components of the gas phase in a volume, as well as explorations of atomization in a high pressure environment. Future work could include implementation of control using acoustic forcing as well as multiphysics control in variable pressure environments subject to large perturbations. The multiphysics control strategies may also be expanded enabling actuation in timescales shorter than the characteristic breakup timescales.

BIBLIOGRAPHY

[1] L.L.F. Agostinho, B. Bos, A. Kamau, S.P. Brouwer, E.C. Fuchs, and J.C.M. Marijnissen. Simple-jet mode electrosprays with water. Description, characterization and application in a single effect evaporation chamber. *Journal of Aerosol Science*, 125:237–250, nov 2018.

[2] A. Aliseda, E.J. Hopfinger, J.C. Lasheras, D.M. Kremer, A. Berchielli, and E.K. Connolly. Atomization of viscous and non-newtonian liquids by a coaxial, high-speed gas jet. Experiments and droplet size modeling. *International Journal of Multiphase Flow*, 34(2):161–175, feb 2008.

[3] Elyar Allaf-Akbari and Nasser Ashgriz. An electrospray in a gaseous crossflow. *Journal of Aerosol Science*, 114:233–243, dec 2017.

[4] Masataka Arai. The Possibility of Active Attitude Control for Fuel Spray. *Engineering*, 5(3):519–534, jun 2019.

[5] G. Billoud, M. A. Galland, C. Huynh Huu, and S. Candel. Adaptive Active Control of Combustion Instabilities. *Combustion Science and Technology*, 81(4-6):257–283, 1992.

[6] Elena Castro-Hernández, Pablo García-Sánchez, Javier Alzaga-Gimeno, Say Hwa Tan, Jean Christophe Baret, and Antonio Ramos. AC electrified jets in a flow-focusing device: Jet length scaling. *Biomicrofluidics*, 10(4):043504, jul 2016.

[7] Norman Chigier and Rolf D. Reitz. *Regimes of Jet Breakup and Breakup Mechanisms (Physical Aspects)*, pages 109–135. American Institute of Aeronautics and Astronautics, Inc., 1996.

[8] Michel Cloupeau and Bernard Prunet-Foch. Electrohydrodynamic spraying functioning modes: a critical review. *Journal of Aerosol Science*, 25(6):1021–1036, sep 1994.

[9] Adam Coker, Yedidia Neumeier, Ben T. Zinn, Suresh Menon, and Tim Lieuwen. Active instability control effectiveness in a liquid fueled combustor. *Combustion Science and Technology*, 178(7):1251–1261, 2006.

[10] Robert T. Collins, Krishnaraj Sambath, Michael T. Harris, and Osman A. Basaran. Universal scaling laws for the disintegration of electrified drops. *Proceedings of the National Academy of Sciences*, 110(13):4905–4910, mar 2013.

[11] T. Conrad, A. Bibik, D. Shcherbik, E. Lubarsky, and B.T. Zinn. Feasibility of "intermittent" active control of combustion instabilities in liquid fueled combustors using a "smart" fuel injector. *Proceedings of the Combustion Institute*, 31(2):2223–2230, jan 2007.

[12] Antoine Delon, Alain Cartellier, and Jean-Philippe Matas. Flapping instability of a liquid jet. *Physical Review Fluids*, 3:43901, 2018.

[13] R. A. Dobbins, L. Crocco, and I. Glassman. Measurement of mean particle sizes of sprays from diffractively scattered light. *AIAA Journal*, 1(8):1882–1886, may 1963.

[14] Jens Eggers and Emmanuel Villermaux. Physics of liquid jets. *Reports on Progress in Physics*, 71(3), 2008.

[15] Ling Fei, Sang Ha Yoo, Rachel Ann R. Villamayor, Brian P. Williams, Seon Young Gong, Sunchan Park, Kyusoon Shin, and Yong Lak Joo. Graphene Oxide Involved Air-Controlled Electrospray for Uniform, Fast, Instantly Dry, and Binder-Free Electrode Fabrication. *ACS Applied Materials & Interfaces*, 9(11):9738–9746, mar 2017.

[16] Thomas P. Forbes, Tim M. Brewer, and Greg Gillen. Primary and secondary droplet and charge transmission characteristics of desorption electro-flow focusing ionization. *Applied Physics Letters*, 102(21):214102, may 2013.

[17] Thomas P. Forbes and Edward Sisco. Mass spectrometry detection and imaging of inorganic and organic explosive device signatures using desorption electro-flow focusing ionization. *Analytical Chemistry*, 86(15):7788–7797, aug 2014.

[18] Alfonso M Gañán-Calvo. Electro-Flow Focusing: The High-Conductivity Low-Viscosity Limit. *Physical Review Letters*, 2007.

[19] Alfonso M. Gañán-Calvo, José M. López-Herrera, Miguel A. Herrada, Antonio Ramos, and José M. Montanero. Review on the physics of electrospray: From electrokinetics to the operating conditions of single and coaxial Taylor cone-jets, and AC electrospray. *Journal of Aerosol Science*, 125:32–56, nov 2018.

[20] Alfonso M. Gañán-Calvo, José M. López-Herrera, and Pascual Riesco-Chueca. The combination of electrospray and flow focusing. *Journal of Fluid Mechanics*, 566:421–445, nov 2006.

[21] A.M. Gañán-Calvo, J. Dávila, and A. Barrero. Current and droplet size in the electrospraying of liquids. Scaling laws. *Journal of Aerosol Science*, 28(2):249–275, mar 1997.

[22] Alessandro Gomez and Keqi Tang. Charge and fission of droplets in electrostatic sprays. *Physics of Fluids*, 6(1):404–414, jan 1994.

[23] Mikhael Gorokhovski and Marcus Herrmann. Modeling primary atomization. *Annual Review of Fluid Mechanics*, 40(1):343–366, 2008.

[24] J.M. Grace and J.C.M. Marijnissen. A review of liquid atomization by electrical means. *Journal of Aerosol Science*, 25(6):1005–1019, sep 1994.

[25] Peng He, Haejune Kim, Dawei Luo, Manuel Marquez, and Zhengdong Cheng. Low-frequency ac electro-flow-focusing microfluidic emulsification. *Applied Physics Letters*, 96(17):174103, apr 2010.

[26] E. J. Hopfinger and J. C. Lasheras. Explosive breakup of a liquid jet by a swirling coaxial gas jet. *Physics of Fluids*, 8(7):1696, jun 1998.

[27] C. M. Jones, J. G. Lee, and D. A. Santavicca. Closed-loop active control of combustion instabilities using subharmonic secondary fuel injection. *Journal of Propulsion and Power*, 15(4):584–590, 1999.

[28] Trung Kien Nguyen, Vu Dat Nguyen, Baekhoon Seong, Nguyen Hoang, Jungkeun Park, and Doyoung Byun. Control and improvement of jet stability by monitoring liquid meniscus in electrospray and electrohydrodynamic jet. *Journal of Aerosol Science*, 71:29–39, may 2014.

[29] Agissilaos Kourmatzis, Egemen L. Ergene, John S. Shrimpton, Dimitrios C. Kyritsis, Farzad Mashayek, and Ming Huo. Combined aerodynamic and electrostatic atomization of dielectric liquid jets. *Experiments in Fluids*, 53(1):221–235, jul 2012.

[30] Abhijeet Kumar and Srikrishna Sahu. Liquid jet breakup unsteadiness in a coaxial air-blast atomizer. *International Journal of Spray and Combustion Dynamics*, 10(3):211–230, sep 2018.

[31] Jose Nathan Kutz. *Data-Driven Modeling & Scientific Computation : Methods for Complex Systems & Big Data*. Oxford University Press, Oxford, first edition. edition, 2013.

[32] J. C. Lasheras and E. J. Hopfinger. Liquid Jet Instability and Atomization in a Coaxial Gas Stream. *Annual Review of Fluid Mechanics*, 32(1):275–308, jan 2000.

[33] J. C. Lasheras, E. Villermaux, and E. J. Hopfinger. Break-up and atomization of a round water jet by a high-speed annular air jet. *Journal of Fluid Mechanics*, 357:351–379, feb 1998.

[34] Arthur H Lefebvre and Vincent G McDonell. *Atomization and Sprays.* CRC Press, Portland, 2 edition, 2017.

[35] Guangbin Li, Xisheng Luo, Ting Si, and Ronald X. Xu. Temporal instability of coflowing liquid-gas jets under an electric field. *Physics of Fluids*, 26(5):054101, may 2014.

[36] Nathanael Machicoane, Julie K. Bothell, Danyu Li, Timothy B. Morgan, Theodore J. Heindel, Alan L. Kastengren, and Alberto Aliseda. Synchrotron radiography characterization of the liquid core dynamics in a canonical two-fluid coaxial atomizer. *International Journal of Multiphase Flow*, 115:1–8, jun 2019.

[37] Nathanael Machicoane, Guillaume Ricard, Rodrigo Osuna-Orozco, Peter Dearborn Huck, and Alberto Aliseda. Influence of steady and oscillating swirl on the near-field spray characteristics in a two-fluid coaxial atomizer. *International Journal of Multiphase Flow*, 129:103318, aug 2020.

[38] Lucia Manna, Claudia Carotenuto, Roberto Nigro, Amedeo Lancia, and Francesco Di Natale. Primary atomization of electrified water sprays. *The Canadian Journal of Chemical Engineering*, 95(9):1781–1788, sep 2017.

[39] P. Marmottant and E. Villermaux. On spray formation. *Journal of Fluid Mechanics*, 498:73–111, jan 2004.

[40] K.R. McManus, T. Poinsot, and S.M. Candel. A review of active control of combustion instabilities. *Progress in Energy and Combustion Science*, 19(1):1–29, jan 1993.

[41] A. J. Mestel. Maximal accelerations for charged drops in an electric field. *Physics of Fluids*, 14(4):1396, mar 2002.

[42] Efstathios Michaelides, Clayton T. Crowe, and John D. Schwarzkopf. *Multiphase flow handbook.* Mechanical and aerospace engineering (CRC Press). Taylor & Francis, CRC Press, Boca Raton, second edition. edition, 2017.

[43] T. M. Muruganandam, S. Nair, D. Scarborough, Y. Neumeier, J. Jagoda, T. Lieuwen, J. Seitzman, and B. Zinn. Active control of lean blowout for turbine engine combustors. *Journal of Propulsion and Power*, 21(5):807–814, 2005.

[44] S. Murugappan, S. Acharya, D. C. Allgood, S. Park, A. M. Annaswamy, and A. F. Ghoniem. Optimal control of a swirl-stabilized spray combustor using system identification approach. *Combustion Science and Technology*, 175(1):55–81, 2003.

[45] Jean Antoine Nollet. *Recherches Sur Les Causes Particulieres Des Phenomenes Electriques*. Freres Guerin, 1754.

[46] Rodrigo Osuna-Orozco, Nathanael Machicoane, Peter D. Huck, and Alberto Aliseda. Feedback control of coaxial atomization based on the spray liquid distribution. *Atomization and Sprays*, 29(6):545–551, 2019.

[47] Rodrigo Osuna-Orozco, Nathanael Machicoane, Peter D. Huck, and Alberto Aliseda. Feedback control of the spray liquid distribution of electrostatically assisted coaxial atomization. *Atomization and Sprays*, 30(1):1–9, 2020.

[48] Manoj Kumar Patel, Bushra Praveen, Hemant Kumar Sahoo, Bharat Patel, Ashwani Kumar, Manjeet Singh, Manoj Kumar Nayak, and Pradeep Rajan. An advance air-induced air-assisted electrostatic nozzle with enhanced performance. *Computers and Electronics in Agriculture*, 135:280–288, apr 2017.

[49] Manoj Kumar Patel, Hemant Kumar Sahoo, Manoj Kumar Nayak, and C. Ghanshyam. Plausibility of variable coverage high range spraying: Experimental studies of an externally air-assisted electrostatic nozzle. *Computers and Electronics in Agriculture*, 127:641–651, sep 2016.

[50] A Putnam. Integratable form of droplet drag coefficient. *ARS Journal*, 31(10):1467–1468, 1961.

[51] Lord Rayleigh. On the equilibrium of liquid conducting masses charged with electricity . *The London, Edinburgh, and Dublin Philosophical Magazine and Journal of Science*, 14(87):184–186, sep 1882.

[52] H. Rehab, E. Villermaux, and E. J. Hopfinger. Flow regimes of large-velocity-ratio coaxial jets. *Journal of Fluid Mechanics*, 345:357–381, aug 1997.

[53] Guillaume Ricard, Nathanaël Machicoane, Rodrigo Osuna-Orozco, Peter D. Huck, and Alberto Aliseda. Role of convective acceleration in the interfacial instability of liquid-gas coaxial jets. *Physical Review Fluids*, 6(8):084302, aug 2021.

[54] Joan Rosell-Llompart, Jordi Grifoll, and Ignacio G. Loscertales. Electrosprays in the cone-jet mode: From Taylor cone formation to spray development. *Journal of Aerosol Science*, 125(May):2–31, 2018.

[55] D. A. Saville. Electrohydrodynamic stability: Fluid cylinders in longitudinal electric fields. *Physics of Fluids*, 13(12):2987–2994, aug 1970.

[56] D. A. Saville. Electrohydrodynamic stability: Effects of charge relaxation at the interface of a liquid jet. *Journal of Fluid Mechanics*, 48(4):815–827, aug 1971.

[57] D. A. Saville. Stability of electrically charged viscous cylinders. *Physics of Fluids*, 14(6):1095–1099, aug 1971.

[58] D. A. Saville. ELECTROHYDRODYNAMICS:The Taylor-Melcher Leaky Dielectric Model. *Annual Review of Fluid Mechanics*, 29(1):27–64, jan 1997.

[59] Baekhoon Seong, Sangyeon Hwang, Hyung-Seok Jang, Hyungdong Lee, Jihoon Kim, Vu Dat Nguyen, Dae-Hyun Cho, Liwei Lin, and Doyoung Byun. A hybrid aerodynamic and electrostatic atomization system for enhanced uniformity of thin film. *Journal of Electrostatics*, 87:93–101, jun 2017.

[60] John S. Shrimpton. Dielectric charged drop break - Up at sub-Rayleigh Limit conditions. *IEEE Transactions on Dielectrics and Electrical Insulation*, 12(3):573–578, jun 2005.

[61] Ting Si, Fang Li, Xie Yuan Yin, and Xie Zhen Yi. Modes in flow focusing and instability of coaxial liquid-gas jets. *Journal of Fluid Mechanics*, 629:1–23, 2009.

[62] Geoffrey Taylor. Disintegration of water drops in an electric field. *Proceedings of the Royal Society of London. Series A. Mathematical and Physical Sciences*, 280(1382):383–397, jul 1964.

[63] C. M. VARGA, J. C. LASHERAS, and E. J. HOPFINGER. Initial breakup of a small-diameter liquid jet by a high-speed gas stream. *Journal of Fluid Mechanics*, 497:405–434, 2003.

[64] S. Verdoold, L.L.F. Agostinho, C.U. Yurteri, and J.C.M. Marijnissen. A generic electrospray classification. *Journal of Aerosol Science*, 67:87–103, jan 2014.

[65] N. Vilanova, V. R. Gundabala, and A. Fernandez-Nieves. Drop size control in electro-coflow. *Applied Physics Letters*, 99(2):021910, jul 2011.

[66] Emmanuel Villermaux. Mixing and spray formation in coaxial jets. *Journal of Propulsion and Power*, 14(5):807–817, may 1998.

[67] Zhentao Wang, John Z. Wen, Junfeng Wang, and Qingming Dong. PDPA investigation on an electrostatically-assisted twin-fluid atomization flow. *Advances in Mechanical Engineering*, 2014, jan 2014.

[68] Herbert H. Woodson and James R. Melcher. *Electromechanical Dynamics*. Wiley, 1968.